R67-17

CAVITATION NEAR SURFACES OF DISTRIBUTED ROUGHNESS

by

Roger E.A. Arndt

Arthur T. Ippen

HYDRODYNAMICS LABORATORY

Report No. 104

Prepared Under

Grant Nos. DA-31-124-ARO-D-189

and DA-31-124-ARO-D-410

U.S. Army Research Office

Durham, North Carolina

June, 1967

MIT

DEPARTMENT OF CIVIL ENGINEERING

SCHOOL OF ENGINEERING

MASSACHUSETTS INSTITUTE OF TECHNOLOGY

Cambridge 39, Massachusetts

R67-17

HYDRODYNAMICS LABORATORY

Department of Civil Engineering

Massachusetts Institute of Technology

CAVITATION NEAR SURFACES OF DISTRIBUTED ROUGHNESS

by

Roger E. A. Arndt and Arthur T. Ippen

June 1967

Report No. 104

Prepared Under

Grants Nos. DA-31-124-ARO-D-189, DA-31-124-ARO-D-410

DA Project No. 20014501B33C

AROD Project No. 6024-E

Army Research Office (Durham)

ABSTRACT

This investigation consists of an experimental study of cavitation inception and the associated bubble dynamics in turbulent boundary layers adjacent to surfaces roughened with two-dimensional triangular grooves. The project was initiated due to the apparent lack of published information on the effects of distributed roughness on cavitation inception as opposed to the effects of isolated irregularities. The experimental program covers the measurement of mean velocity profiles, turbulence intensity and the determination of the cavitation inception index for turbulent flow adjacent to both smooth and rough boundaries. In all cases the test liquid was water at room temperature. Four triangular roughness patterns were tested, consisting of roughness heights of 0.100", 0.050", 0.025", and 0.0125", respectively. The maximum velocity was varied between the limits 16 to 51 feet per second. For the same conditions, cavitating flow was observed by high speed motion pictures. Data concerning bubble distribution, stability, and growth rate were obtained from the photographs and correlated with existing theory.

The experiments resulted in the significant conclusion that the cavitation inception index may be directly related to the skin friction coefficient for smooth and rough boundaries. It was also determined that the inception index is less for surfaces having a distributed roughness than for an isolated irregularity of equivalent height. Photographic observations showed that in all cases, cavitation inception occurred away from the wall, approximately in the center of the boundary layer. At the same time, the maximum concentration of nonexpanding bubbles was observed to be close to the wall. Bubble distributions were found that could be correlated with existing turbulent diffusion theory. Bubble stability data and bubble growth data both indicated inception pressures which correspond to tensions of not more than 1 psi. The actual inception process is started by negative peaks in static pressure fluctuations which correspond to approximately 5 to 7 times the expected values of the root mean square wall pressure. Turbulence intensity in the region of cavitation inception was found to be primarily dependent on the value of the wall shear stress. Agreement with hot wire investigations made by others in air was quite satisfactory.

Values for skin friction could be correlated with a Reynolds number defined by the displacement thickness and modified for the effects of roughness pressure gradient. Data obtained near both smooth and rough boundaries follow the same universal law. Mean velocity measurements were in substantial agreement with previously reported data for equilibrium boundary layers.

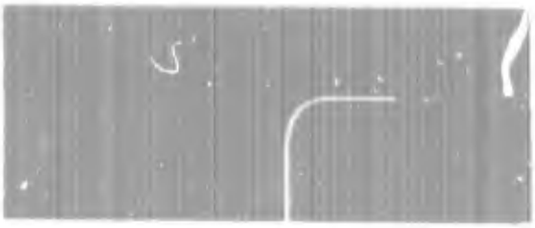

σ = 1.05

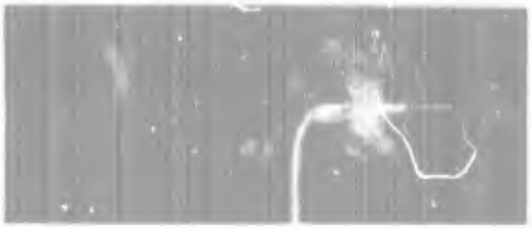

σ = .52

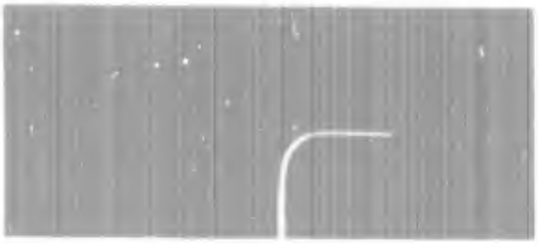

σ = .91

σ = .34

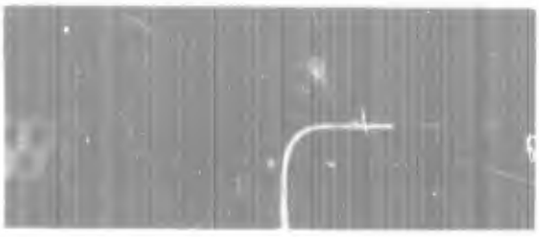

σ = .75

σ = .24

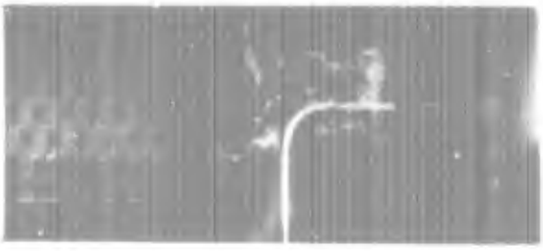

σ = .63

σ = .15

Example of Cavitation on a Disk

ACKNOWLEDGEMENTS

The investigation was sponsored by the Army Research Office (Durham) under Contracts No. DA-31-124-ARO-D-189 and No. DA-31-124-ARO-D-410. Dr James Murray acted as contract coordinator for the Army. The work was administered at the Massachusetts Institute of Technology by the Division of Sponsored Research under Project No. 76089. The National Aeronautics and Space Administration provided financial assistance for Mr. Arndt through a traineeship award for 1965 to 1967.

This report is based on the work presented by Mr. Arndt for his Ph.D. dissertation. Dr. Arthur T. Ippen acted as project supervisor for the major portion of the program. For the period 1 July 1964 to 31 July 1965, the work was under the technical direction of Dr. Zeev Kronfeld, Visiting Associate Professor of Civil Engineering, and under the supervision of Dr. Peter S. Eagleson. Mr. Charles Horstman, Research Assistant, was employed on the project during this period. Dr. James W. Daily (Since 1 September 1964: Head, Department of Engineering Mechanics, University of Michigan) originally had proposed work of this type and acted as a consultant to the project during the initial phases in 1964/65.

A special work of thanks must go to Mr. Herbert Messenger, employed as Research Assistant on the project since 1 June 1966. His painstaking assistance in the collection and analysis of data is gratefully acknowledged. Mr. Edward McCaffrey, electronic technician, was of considerable help in the development and maintenance of the apparatus. Most of the machine work was performed by the machine shop staff of the M.I.T. Gas Turbine Laboratory under the able supervision of Mr. Paul Wassmouth.

TABLE OF CONTENTS

TABLE OF CONTENTS (Cont'd.)

TABLE OF CONTENTS (Cont'd.)

LIST OF FIGURES AND TABLES

LIST OF FIGURES AND TABLES (Cont'd.)

LIST OF FIGURES AND TABLES (Cont'd.)

LIST OF FIGURES AND TABLES (Cont'd.)

LIST OF SYMBOLS*

A	Constant, defined in text
B	Constant, defined in text
C	Constant, defined in text
C_f	Local skin friction coefficient, $(C_f = \frac{\tau_o}{\rho\frac{U^2}{2}})$
C_L	Lift coefficient, $Li/\rho\frac{U^2}{2} S_*$
C_p	Pressure coefficient, $(p - p_o)/\rho\frac{U_o^2}{2}$
C_{pmin}	Minimum pressure coefficient, $(p_{min} - p_o)/\rho\frac{U_o^2}{2}$
d	Probe diameter
d_b	Bubble diameter
d^*	Critical bubble diameter
$E(f)$	Energy density
f	Frequency
f_d	Natural frequency of transducer
f_o	Natural frequency of turbulence gage
F	Function, defined in text
F_1	Roughness factor $(\log^{-1} \overline{\Delta u_1}/5.6u_*)$
F_2	Pressure gradient factor $(\log^{-1} \overline{\Delta u_2}/5.6u_*)$
g	Gravitational constant (32.174 ft./sec.^{2})
G	Shape factor, $G = \frac{U}{u_*}(\frac{H-1}{H})$
h	Manometer reading
H	Shape factor, $H = \delta_*/\theta$
k	Mechanical roughness height
k_s	Equivalent sand grain roughness
K	Constant, defined in text
L	Characteristic length
Li	Lift
m	Source strength

* Only the principal symbols are defined here. Those symbols which have limited usage within a section are defined where they first appear.

n	Exponent in velocity power law $\frac{\overline{u}}{U} = (\frac{y}{\delta})^{1/n}$
p	Pressure
$\overline{p}$	Temporal mean pressure
p'	Fluctuating pressure component
p_{cr}	Critical pressure
p_o	Reference pressure
p_{vp}	Vapor pressure
p^*	$p_{cr} - p_{vp}$
p_a	Pressure outside of bubble wall
r	Radial coordinate
R	Bubble radius
R^*	Critical bubble radius
$\mathbb{R}$	Reynolds number Ul/r
$\mathbb{R}_\delta$	Reynolds number based on boundary layer thickness $(\frac{U\delta}{\nu})$
$\mathbb{R}_{\delta^*}$	Reynolds number based on displacement thickness $(\frac{U\delta^*}{\nu})$
$\mathbb{R}_\theta$	Reynolds number based on momentum thickness $(\frac{U\theta}{\nu})$
$\mathbb{R}_p$	Probe Reynolds number $(U_o d/\nu)$
s	Surface tension
S	Slope of logarithmic velocity profile
S_o	Surface area
t	Time
T	Temperature
$\overline{u}$	Local mean velocity, longitudinal direction
u_i	Local velocity component, $(i = 1, 2, 3)$
$\overline{u}_i$	Temporal mean velocity component, $(i = 1, 2, 3)$
u_i'	Fluctuating component of velocity, $(i = 1, 2, 3)$
u_*	Shear velocity $(u_* = \sqrt{\tau_o/\rho})$
U	Maximum local velocity

U_o	Reference velocity
$\bar{v}$	Local mean velocity perpendicular to wall
v'	Velocity fluctuation perpendicular to wall
V_c	Characteristic velocity
V^*	Gas content, % by volume at N.T.P.
$\bar{w}$	Local mean velocity perpendicular to $\bar{u}$ and $\bar{v}$
ω	Bubble rise velocity
W	Weight of gas per bubble
x	Longitudinal coordinate
x_i	Cartesian coordinates (i = 1, 2, 3)
y	Distance from the wall
z	Coordinate perpendicular to x and y
Z	Exponents in concentration power law
α	Gas content
β	Constant in Henry's law
γ	Specific weight
δ	Boundary layer thickness
Δ	Characteristic boundary layer thickness, $\Delta = \frac{U}{u_*}\delta_*$
Δp	Pressure difference
$\Delta\bar{u}_1$	Velocity defect due to roughness
$\Delta\bar{u}_2$	Velocity defect due to pressure gradient
θ	Momentum thickness
κ	von Karman constant
λ	Darcy - Weisbach friction factor
Π	Constant in Cole's wake function
ρ	Mass density (γ/g)
σ	Cavitation index, $(p_o - p_{vp})/\rho\frac{U_o^2}{2}$
σ_i	Incipient cavitation index (value of σ at the onset of cavitation)
$\bar{\sigma}_i$	Incipient cavitation index, smooth body.
τ_o	Wall shear stress
ν	Kinematic viscosity
ϕ	Velocity potential
ψ	Functional relationship

I. INTRODUCTION

1.1 General Background

After more than half a century of intensive research, cavitation in liquids still remains as a basic problem area in many branches of engineering. In fact, with the onset of modern technology, the problem has become more acute than ever before. For engineering purposes, cavitation may be defined as the process of formation of the vapor phase of a liquid when subjected to reduced pressures. A liquid is said to cavitate when vapor bubbles form as a consequence of reduced pressure in the liquid.

Cavitation occurs whenever the local pressure in a flow field falls below a certain critical value. It is a problem in many areas such as in turbomachinery, hydrofoils, marine propellers and various hydraulic structures; conduits, valves, spillways, etc. In fact there is a possibility of cavitation in practically every instance of liquid flow.

In the initial stages of cavitation macro-sized bubbles form in the minimum pressure region and are swept away into regions of higher pressure. The bubbles then collapse in such a manner that very high pressures are produced locally, creating noise, hydroelastic vibrations and even physical damage to the structure itself. Further reduction in pressure results in more severe cavitation and can result in large vapor filled cavities which remain attached to solid surfaces as shown in the frontispiece. At this point the performance of turbomachinery or of hydrofoils falls off severely.

Severe cavitation damage and degradation of performance of turbines, pumps, hydrofoils, spillways, energy dissipators, etc., is commonplace and has been cited again and again in the literature.

As far back as 1754, Leonard Euler, in a memoir on the theory of hydraulic turbines, suggested the possibility of a limiting pressure and loss of performance. In more recent times cavitation was investigated by Reynolds (1901) in a simple experiment with a tube having a constriction such that flow velocity increased with a resulting decrease in pressure sufficient to create cavitation. The impetus for this early research came from the introduction of propellers for ships in the later part of the 19th century. It was observed that after a critical speed was reached, the propeller would "race" with a resultant loss in power and efficiency. Burril (1951) describes the cavitation problems encountered in the full scale trials

I. INTRODUCTION

1.1 General Background

After more than half a century of intensive research, cavitation in liquids still remains as a basic problem area in many branches of engineering. In fact, with the onset of modern technology, the problem has become more acute than ever before. For engineering purposes, cavitation may be defined as the process of formation of the vapor phase of a liquid when subjected to reduced pressures. A liquid is said to cavitate when vapor bubbles form as a consequence of reduced pressure in the liquid.

Cavitation occurs whenever the local pressure in a flow field falls below a certain critical value. It is a problem in many areas such as in turbomachinery, hydrofoils, marine propellers and various hydraulic structures; conduits, valves, spillways, etc. In fact there is a possibility of cavitation in practically every instance of liquid flow.

In the initial stages of cavitation macro-sized bubbles form in the minimum pressure region and are swept away into regions of higher pressure. The bubbles then collapse in such a manner that very high pressures are produced locally, creating noise, hydroelastic vibrations and even physical damage to the structure itself. Further reduction in pressure results in more severe cavitation and can result in large vapor filled cavities which remain attached to solid surfaces as shown in the frontispiece. At this point the performance of turbomachinery or of hydrofoils falls off severely.

Severe cavitation damage and degradation of performance of turbines, pumps, hydrofoils, spillways, energy dissipators, etc., is commonplace and has been cited again and again in the literature.

As far back as 1754, Leonard Euler, in a memoir on the theory of hydraulic turbines, suggested the possibility of a limiting pressure and loss of performance. In more recent times cavitation was investigated by Reynolds (1901) in a simple experiment with a tube having a constriction such that flow velocity increased with a resulting decrease in pressure sufficient to create cavitation. The impetus for this early research came from the introduction of propellers for ships in the later part of the 19th century. It was observed that after a critical speed was reached, the propeller would "race" with a resultant loss in power and efficiency. Burril (1951) describes the cavitation problems encountered in the full scale trials

of the "H.M.S. Turbinia" in the 1890's. Eisenberg (1963) further cites cavitation problems in the trials of the "H.M.S. Daring" during the same period. Eisenberg also attributes the coining of the term "cavitation" to R. E. Froude, then director of the British Admirality's ship model testing laboratory.

Since the early beginnings in cavitation research, a vast quantity of literature on the subject has been generated. All the investigations to date can probably be put in one of three categories: 1) cavitation inception, 2) cavitation damage, 3) fully caviting flows. Although not completely defined, an insight into cavitation inception requires first an understanding of the location and magnitude of the minimum pressure within a given flow field and secondly an understanding of the precise mechanism of cavitation inception or in other words a knowledge of the magnitude and duration of the critical pressure necessary for cavitation. As will be shown in subsequent chapters, time dependent variations in pressure are of considerable importance in cavitation and can have far reaching effects when it comes to predicting inception. Inherent in this area of research is the question of scaling model test data to the prototype. In fact, scale effects remain as a fundamental problem in model test work as cited by Holl and Wislicenus (1961). This investigation may be classified in this general area.

The area of cavitation damage has been of particular interest in recent times to not only the marine engineer and hydraulic engineer but also to the nuclear and propulsion engineer who finds himself concerned with pumping of exotic liquids such as the cryogenic liquids and liquid metals, i.e., mercury, molten potassium and sodium. The interest in a fundamental understanding of cavitation damage has resulted in the bringing together of the diverse research areas of bubble collapse, shock propagation in liquids and solids, fatigue limits under shock loading of various materials and other complex considerations in both fluid and solid mechanics. This whole area is a field in itself and will not be discussed further.

The third area, namely cavity flow, is another complete field in itself and perhaps has seen the most successful use of mathematical treatment. A direct analogy may be drawn between the transition from subsonic to supersonic aerodynamic research and the shift from cavitation inception research to fully cavitating flow investigations. This was brought about when it became apparent in the late forties and early fifties, that in many cases the speed regime of propellers, pumps, hydrofoils, etc.

was such that cavitation was unavoidable. Various components had to be designed where cavitation was not avoided but actually sought in the design. Examples of cavity flow analysis and design are numerous in the literature. The beginnings of the research probably date back to Lord Kelvin's (1887) attempt to explain the d'Alembert paradox. Kelvin's solution did not accurately predict the drag of an infinitely long flat plate transverse to the flow in the fully wetted state but is quite precise for the case of a plate with an attached vapor filled cavity, similar to that shown on the final picture in the frontispiece. The beginnings of modern research in the area may be found in various post-war papers such as those of Reichardt (1945), Plesset and Shaffer (1948), and Tulin and Burkart (1955). However, no further mention of this field will be made in the following treatment.

1.2 The Roughness Problem with Regards to Cavitation

It is a well accepted fact that in many instances of practical importance, surfaces in contact with a flowing liquid are not hydrodynamically smooth. Roughness can result from practical limitations on surface finish such as for example the smoothness of concrete structures or the relative smoothness obtainable in turbomachinery or hydrofoils. Other problems erupt from isolated irregularities such as a mismatch of joints and the presence of rivets, screws, etc. Most work to date has been concerned with the effect of isolated irregularities. Rather limited work has been done on the effects of distributed roughness as opposed to an isolated irregularity. Associated with the roughness problem are the turbulence and boundary layer parameters. In the case of an isolated irregularity, it has been shown by Holl (1959) that the boundary layer parameters may be treated as input to the cavitation inception problem. Obviously, in the case of distributed roughness the nature of the boundary layer is directly related to the surface roughness and to the pressure distribution which in turn is related to body shape and the growth of the boundary layer itself.

1.3 Objectives and Summary of the Present Investigation

A survey of previous investigations into the cavitation inception problem indicates that a more thorough understanding of the effects of turbulence and wall shear on cavitation in a boundary layer is required. Such an understanding is essential since in many practical cases cavitation inception occurs in a boundary layer. In particular this study was aimed at the more specific problem of a

boundary layer flow over a distributed roughness. The pioneering work of Daily and Johnson (1956) on the effect of the boundary layer and turbulence on cavitation inception near a smooth wall provided a firm foundation for the logical extension of this research to inception near rough walls. In fact, the experimental apparatus used in this investigation is an improved version of that used by Daily and Johnson.

Preliminary considerations indicated that the important parameters to be investigated were relative roughness, mean velocity profiles, turbulence intensity, wall shear, incipient cavitation index and the details of the bubble dynamics associated with the cavitation inception. Initial studies were made with a smooth roof, and the experimental techniques developed during this primary phase were extended to the investigation of cavitation inception, bubble dynamics, boundary layer developement and turbulence intensity near various surfaces having geometrically similar patterns of roughness.

Cavitation inception was studied visually whereas the details of the bubble dynamics were investigated with high speed photography. Three methods of determining skin friction were used -- the Preston tube, the Von Karman Momentum Integral Method, and a relatively new technique based on the universal law of the wall for the mean velocity profile. Turbulence was measured with a completely redesigned and improved total head tube-transducer combination similar to that originally used by Ippen et al (1955).

Skin friction measurements were correlated into a universal law for boundary layers with smooth and rough boundaries and both adverse and favorable pressure gradients as originally suggested by Clauser (1954). Turbulence intensity and cavitation inception are both shown to be directly related to the wall shear. Values of mean pressure at the wall measured during cavitation inception were consistently and considerably higher than the vapor pressure of the test fluid (room temperature water in all cases). Analysis of this result with consideration of the measurements of Wooldridge and Willmarth (1962) and others indicates that cavitation inception is initiated by pressure fluctuations having a frequency of occurrence of less than 5%. This result is not inconsistent with both theory and similar conclusions drawn by Rouse (1953). Investigation of the bubble distribution in the boundary layer, for wall pressures less than critical, indicated that turbulent diffusion is the controlling factor in the distribution. Close

agreement with the distributions predicted by the classical sedimentation theory for fully developed turbulent flows was obtained. Of great importance is the associated result that cavitation inception for all cases tested occurs in the center of the boundary layer which is also consistent with the results of Daily and Johnson (1956). This result is not completely consistent with present thought on the location of minimum pressure in a turbulent boundary layer. In addition, the roughness grooves themselves were observed to be the source of nuclei for the subsequent cavitation inception in the center of the boundary layer.

Experience with the experimental apparatus, especially a flattened version of the Preston tube and the turbulence gage has proved useful and is presented in some detail in the Appendix.

Finally this investigation indicates the close relationship between cavitation research and modern hydrodynamic and aerodynamic research on boundary layer noise and the fundamental structure of turbulent shear flows.

II. REVIEW OF PREVIOUS INVESTIGATIONS

2.1 General Introduction

The literature generated during the past half century on all aspects of cavitation is quite extensive; and, therefore, it is essential to restrict this review to papers directly related to the task at hand. Primary consideration is thus given to the mechanics of inception, bubble dynamics and turbulence intensity as defined by boundary layer parameters and related to roughness. Many interesting papers dealing with other observations of particular cases of cavitation as well as with fully cavitating flows and cavitation damage, while reviewed for their relevance to this study, must be considered of secondary importance; and hence, will receive no further mention here.

2.2 Cavitation Inception and the Scale Effects Problem

Probably the first important theoretical contribution to the investigation of cavitation is due to Rayleigh (1917). Rayleigh considered the collapse of an empty spherical cavity for the case of an incompressible fluid with the pressure remaining constant at infinity. He obtained a solution by equating the resulting kinetic energy of the fluid to the work done at infinity by the pressure acting through a change of volume equal to the change of volume of the bubble. A solution was found for the wall velocity as a function of radius and of time of collapse and for the pressure distribution in the surrounding fluid. He also considered the effect of gas content on the resulting motion by assuming isothermal compression of the gas. Finally, Rayleigh computed the pressure produced if any empty bubble collapses on an absolutely rigid sphere. Here he abandons the assumption of an incompressible fluid but only after impact with the rigid sphere. Plesset (1949) revived the Rayleigh theory and extended it to the consideration of a cavitation bubble in the flow about a submerged ogive body. For this study Plesset neglected the effects of the boundary layer but included the history of the pressure external to the bubble as it moves from a region of high pressure through the minimum pressure zone and on to the zone of pressure recovery on the body. He obtained good agreement with theory except for the initial stages of growth and the later stages of collapse. He further shows that for inception in cold water, heat transfer effects and gas diffusion effects are negligible. For the latter case this is demonstrated by the quantity of heat necessary for the evaporation of water during bubble growth and the temperature gradients necessary

through the diffusion layer for this transfer of heat. In cold water this amounts to fractions of a degree. This problem is further considered in detail by Plesset and Zwick (1954). Knapp and Hollander (1948) had previously developed a photographic technique for observing the history of cavitation bubbles. They obtained good agreement for the velocity of collapse with the Rayleigh theory. They also point out that with increasing intensity of cavitation the bubble concentration increases to the point where interference effects are important.

The first applications of the Rayleigh theory have been extended to the stability of gas bubbles by Epstein and Plesset (1950), the growth of vapor bubbles in superheated water by Plesset and Zwick (1954) and gaseous cavitation induced by sound by Strasberg (1957), Plesset and Hsieh (1960), Hsieh and Plesset (1961) and Eller and Flynn (1963). An excellent summary of this research has been given since by Plesset (1964). Of importance to this study is the fact that the effects of heat transfer, compressibility of the liquid, and vaporization time are unimportant for the study of cavitation inception in cold water. However, even though the time constants for gas diffusion are much larger than for vaporous cavitation, Strasberg points out that bubbles may initially grow to a critical size by gaseous cavitation and then initiate vaporous cavitation.

At the same time that new interest arose in bubble dynamics, research into scale effects was intensified. Scale effects refer to the fact that the so-called cavitation index, originally proposed by Thoma (1924),

$$\sigma = \frac{p_o - p_{vp}}{\rho \frac{U_o^2}{2}} \tag{2.1}$$

where p_o is some reference pressure

p_{vp} is the vapor pressure of the liquid

$\rho \frac{U_o^2}{2}$ is the free stream dynamic pressure

is not the only parameter which determines the onset of cavitation. Kermeen, McGraw and Parkin (1955) investigated the variation of incipient cavitation with Reynolds number for various submerged bodies. It was found that as scale and velocity increase

the cavitation inception number approaches the absolute value of the minimum pressure coefficient for streamlined bodies. On the other hand, Reynolds number was a significant scaling parameter for sharp-edged disks. The differences in the cavitation inception phenomena were observed photographically. Inception for the streamlined bodies began near the surface in the boundary layer, whereas inception in the case of the disks was observed to occur in the cores of vortices in the wake. For the first time tensions were observed and measured in the flow of ordinary water during incipient cavitation. In a discussion of this paper, Holl and Robertson suggested a correlation of data with the Weber number,

$$W = \frac{U_o}{\sqrt{s/\rho L}} \tag{2.2}$$

where U_o is a characteristic velocity

s is the liquid surface tension

ρ is the liquid density

L is a characteristic length

and showed that some cavitation inception data for hemispheres and ogives collapsed to one curve when plotted versus the product of the free stream velocity and the square root of the model diameter. Robertson, e . al., (1957) also reported a Reynolds number correlation for cavitation inception data on disks, and a Weber number correlation for various ogive nosed cylinders. For the blunter-nosed ogive bodies they suggest that either scaling law may apply and different inception indices can occur. They further suggested the existence of two regimes of cavitation inception. Oshima (1960) considered theoretically the scale effects of cavitation inception on geometrically similar bodies. His mathematical model is based on Rayleigh's equation for spherical cavitation bubbles. Real fluid effects are introduced by assuming dynamically similar growth on geometrically similar bodies until bubble sizes approaching the respective displacement thickness are approached as suggested by Kermeen, et. al., (1955). Real fluid effects are neglected in the sense that inception is assumed to occur at geometrically similar points on each body. Pressure distributions and boundary layer properties are assumed independent of Reynolds number. The key to the scaling effect

in this theory is the time of exposure of a cavitation nucleus to minimum pressures on the body. A dependence of cavitation index on body size and velocity is found which is apparently in good agreement with selected experimental results. Holl and Wislicenus (1960) considered the scale effects expressed by similarity considerations, including the dependency on fluid properties, roughness, temperature, gas content, number of nuclei, etc. They concluded from the analysis of extensive experimental data that scale effects are important and that the relative importance of various parameters other than the cavitation index was strongly related to the particular type of flow. Viscosity and surface tension effects are important for cavitation attached to a wall. For cavitation away from a solid surface it was found that factors such as the number of nuclei in the flow and a characteristic velocity of the cavitation process are important. In a discussion of the paper by Holl and Wislicenus, McCormick derives a simple expression for the dependence of the cavitation index on the Reynolds number for sharp-edged disks. In the analysis he neglects scale effects due to the bubble dynamics by assuming the pressure at cavitation inception to be equal to the vapor pressure of the liquid. McCormick related the strength of the vortex shed from the disk to a characteristic velocity and length and to the boundary layer formed on the face of the disk. Assuming a Rankine model for the pressure distribution through the vortex and a power law for the boundary layer profile,

$$\frac{\bar{u}}{U} = \left(\frac{Y}{\delta}\right)^{1/n} \tag{2.3}$$

he obtains a relationship between incipient cavitation index, σ_i, and Reynolds number, Re, given by

$$\sigma_i = CRe^{1/n} \tag{2.4}$$

where C is an undetermined constant. The best fit of the data cited by Holl and Wislicenus gives a value of the exponent, n, of 3.55 which is certainly a reasonable value for a boundary layer near a separation point. The important point is that the scale effects <u>in this particular case</u> are primarily a function of viscous action and the details of inception are probably unimportant.

The role of bubble dynamics, the associated effects of gas content and diffusion, and the stability of cavitation nuclei have been the subject of many investigations. Ripkin and Olsen (1958) and Ripkin (1959) have made experiments on bodies of revolution that indicate that the so-called hysteresis effect is absent in tests with a high free air content. This effect is evident as the difference between the value of pressure at the onset of cavitation and the value of pressure required to remove cavitation. Hysteresis is present in water with a low number of nuclei. They further hypothesize on the action of vorticity in the flow as a stabilizing mechanism for cavitation nuclei.

Another suggestion for the existence of nuclei is given by Harvey, et. al., (1947). They suggested the stabilization of small bubbles in small cracks or crevices in the wall material. Further work on hysteresis was done by Holl and Treaster (1966) which confirms Ripkin's original hypothesis. They found that a certain time is required for a certain number of nuclei to flow into the minimum pressure region and create cavitation. It was observed that tensions of as high as 8 to 9 psi would be attained on the test body immediately after quickly lowering the static pressure level in their water tunnel. The tension would exist for several seconds before cavitation occurred with a sudden increase in pressure to a value equal to the vapor pressure. A theoretical model based on the Rayleigh equation is presented which approximates the experimental evidence. Johnson and Eisenberg (1966) also cite the effect of nuclei content on cavitation inception and conclude that the accepted technique for cavitation testing using water with a low gas content and resorbers to drive undissolved gas back into solution in the water tunnel circuit, will result in scale effects for model data. Hence, model tests thus performed give optimistic values for the cavitation performance of full-scale hydrofoils, pump blades, propellers, etc. However, Holl (1960) cites a scale effect of the opposite trend when saturated water is used. For saturated water he derived the relationship for streamlined bodies:

$$\sigma_i = -C_{p_{min}} + \frac{g\beta}{\rho \frac{U}{2}} \qquad (2.5)$$

where $C_{p_{min}}$ is the minimum pressure coefficient

α is the dissolved air content in ppm by weight

β is Henry's constant, psi/ppm

$\rho \frac{U^2}{2}$ is the free stream dynamic pressure

Good agreement with some data published by Calehuff and Wislicenus (1956) was found. In summary, the available literature on the subject of scale effects indicates that great care must be exercised in extrapolating any model data on cavitation.

2.3 Turbulence and Roughness Effects on Cavitation Inception

A particular category of the scale effects problem cited above are the effects of turbulence and roughness. Few data are available on these two particular aspects of cavitation inception.

Rouse (1953) investigated cavitation inception in the high shear zone of a submerged water jet. Inception data obtained in water were correlated with measurements of the fluctuating static pressure in a free air jet. The results indicated that cavitation occurred at a value of the cavitation index given by

$$\sigma_i = 10 \frac{\sqrt{\overline{p'^2}}}{\rho \frac{U_o^2}{2}} \tag{2.6}$$

where $\sqrt{\overline{p'^2}}$ is the maximum value of the root mean square value of the static pressure fluctuations

$\rho \frac{U_o^2}{2}$ is the dynamic pressure at jet nozzle.

Rouse points out that it is the negative peak of the pressure fluctuations that is important. Further, he attributes the coefficient of 10 to both temporal and spatial variations of turbulence. In other words he hypothesizes that

$$\sigma_i = C_t \, C_s \frac{\sqrt{\overline{p'^2}}}{\rho \frac{U_o^2}{2}} \tag{2.7}$$

where C_t is the effect of temporal variations in turbulence

C_s is the effect of spatial variations

Rouse points out that if a Gaussian distribution of temporal variations of pressure with time is assumed, and if negative pressure fluctuations which occur less than 5% are responsible for the cavitation inception, then the coefficient C_t has the value 1.64.

Daily and Johnson (1956) investigated the effect of boundary layer turbulence on cavitation inception. They found that inception near a smooth wall in a two-dimensional water tunnel would always occur when the local wall pressure was greater than the vapor pressure. They correctly attribute this to a pressure reduction in the boundary layer due to turbulence. Using turbulence data estimated from high-speed photographs of cavitation bubbles in the flow and applying Batchelor's (1951) equation for isotropic turbulence:

$$\sqrt{\overline{p'^2}} = 0.583\ \rho\overline{u'^2} \tag{2.8}$$

they obtained the value

$$\sigma_i = 7.9\ \frac{\sqrt{\overline{p'^2}}}{\rho\,\frac{U^2}{2}} \tag{2.9}$$

In addition, they noticed from inspection of high-speed motion pictures of the cavitating flow that inception occurred in the center of the boundary layer. This is in contradiction to the theoretical result that the static pressure in a turbulent boundary is a minimum close to the wall.

The major portion of the literature on the effects of roughness on cavitation inception is limited to studies of isolated irregularities. Eisenberg (1951) considered the effects of small errors in the shape of a given body using potential theory. This study is limited to a "waviness" of the boundary rather than a sharp-edged irregularity. Shalnev (1950), (1951) presents empirical data for inception on different discrete roughnesses and roughness projections such as occur at the ends of turbomachinery blades. He did not correlate his data with boundary layer

properties.

Holl (1959) conducted an exhaustive series of experiments on cavitation inception for two-dimensional isolated irregularities submerged in a boundary layer flow. Both sharp-edged protuberances and circular arc projections were studied. It was found that correlation of the cavitation inception index could be achieved by comparing it to the height of the roughness in terms of the boundary layer thickness, to the boundary layer shape factor (defined as the ratio of displacement thickness to momentum thickness) and to a Reynolds number based on roughness height and local velocity. Reasonable correlation with theory was achieved for the case of unseparated flow over the circular arc protuberances. Recently, Benson (1966) studied the problem of cavitation inception related to three-dimensional roughness elements. Patterns of roughness consisting of a row of equally-spaced elements on a flat plate were studied with the row both aligned with the flow direction and transverse to the flow direction. Roughness shapes considered were cones, cylinders and hemispheres. Similar trends to those observed by Holl were found for the dependence of the inception index on relative roughness and Reynolds number.

Previous investigations of cavitation near surfaces having distributed roughness are quite few in number. Benson (1958) made a limited study of cavitation near a wall roughened with closely-spaced rectangular slots transverse to the flow. At relatively high wall pressures, cavitation was first observed in the slots. The cavitation in these grooves then supplied nuclei to the flow in the adjacent boundary layer where cavitation occurred when the pressure was lowered still further. The variation of the incipient cavitation index with velocity for the boundary layer was fairly small whereas the variation of the index for groove cavitation was from 1.2 to 0.35 over a range in velocity from 20 to 50 feet per second respectively. Close inspection of these data appear to indicate the occurrence of gaseous cavitation in the grooves and vaporous cavitation in the boundary layer.

Colgate (1959) made a limited study of cavitation near two types of concrete surfaces in a two-dimensional duct. For each surface he correlated wall pressure at cavitation inception with wall shear velocity. However, the values of wall shear reported for a relative roughness height of approximately 0.4 appear much too low when compared with other measurements of shear stress near rough boundaries such as, for example, Nikuradse (1933). More recently, Numachi, et. al., (1965a)

(1965b) and Numachi (1966) have studied the effect of surface striations on hydrofoil performance. Tests on the effect of roughness on lift and drag under cavitating and non-cavitating conditions were run with hydrofoils having the roughness grooves directed either parallel to the flow direction or transverse to the flow direction. In both cases degradation of both cavitating and non-cavitating performance was observed which increased in severity with an increase in roughness height. The cavitation stall point (the value where lift drops off with a decrease in free stream static pressure) was observed to occur at values of the cavitation index which increased with an increase in the intensity of roughness.

2.4 Turbulent Shear Flow Near Smooth and Rough Boundaries: Investigation of Temporal Mean Velocity Distribution and Wall Shear Stress

A comprehensive treatment of the literature on turbulent boundary layers is beyond the scope of this investigation. However, an excellent summary of the early thought on this subject was given by Schlichting (1960). Clauser (1956) also provided an excellent synopsis of present thought on the mean structure of a turbulent boundary layer, which included his earlier (1954) work, along with some new suggestions for further research in the area. He re-emphasized the existence of a universal law of the wall, which was first derived using a similarity argument by Prandtl (1962). A slightly different apporach was offered by Von Karman (1932) and a critical review of the similarity argument was given by Millikan (1938). This law of the wall holds in the region very close to the wall out to approximately 15% of the total boundary layer thickness and is given by

$$\frac{\bar{u}}{u_*} = \frac{1}{\kappa} \ln \frac{u_* y}{\nu} + A \qquad (2.10)$$

where $\bar{u}$ is the local temporal mean velocity at a distance y from the wall

u_* is the shear velocity

ν is the kinematic viscosity

κ is the Von Karman constant

The constant A is independent of pressure gradient but varies with wall roughness. Clauser finds from his analysis of several sets of data that κ is 0.41 and that A has the value 4.9 for smooth walls. Corresponding to the law of the wall, Clauser

(1956) also suggests a universal velocity defect law which, in the region of validity of the law of the wall, is given by

$$\frac{\bar{u} - U}{u_*} = \frac{1}{\kappa} \ln \frac{u_* y}{U \delta_*} + B \qquad (2.11)$$

where U is the maximum velocity

δ_* is the displacement thickness

Here the constant B is <u>independent of roughness</u> but is dependent on the pressure gradient. By a very unique method of considering the outer portion of a turbulent boundary layer as a laminar layer having a constant value of eddy viscosity and having a velocity distribution which can be extrapolated to a finite slip velocity at the wall, Clauser (1956) was able to arrive at some interesting conclusions concerning the similarity of boundary layers. He deduced from the theory and available experimental evidence that:

1. The eddy viscosity in the outer 80%-90% of the boundary layer is constant and proportional to the product of maximum velocity and displacement thickness.
2. The eddy viscosity at the inner portion of the boundary layer is proportional to the product of the shear velocity and the distance from the wall.
3. For equilibrium boundary layers given by a constant value of the parameter

$$\frac{\delta_*}{\tau_o} \frac{\partial p}{\partial x}$$

where τ_o is the wall shear stress and $\frac{\partial p}{\partial x}$ is the pressure gradient in the direction of flow, the constants of proportionality for the "inner" and "outer" laws of eddy viscosity are independent of the effects of roughness and pressure gradient.

At the same time Coles (1956) made an extensive survey of existing experimental data on the turbulent boundary layer. He suggests that the entire boundary layer may be represented by two universal laws; the inner portion by the logarithmic law of the wall and the outer portion by a universal wake function which is characterized by the profile at a point of separation or reattachment. The equation for the distribution of temporal mean velocity through a turbulent boundary layer is given by Coles as

$$\frac{\bar{u}}{u_*} = \frac{1}{\kappa} \ln \frac{u_* y}{\nu} + \frac{\Pi}{\kappa} \omega\left(\frac{y}{\delta}\right) + A \qquad (2.12)$$

where ω is the universal wake function

Π is a function of the local wallshear stress and the parameter, $\frac{U\delta_*}{\nu}$

Further, Coles demonstrates that when the shear stress at the wall approaches zero, the velocity distribution reduces to

$$\frac{\bar{u}}{U} = \frac{1}{2} \omega\ (y/\delta) \qquad (2.13)$$

A tabulation of the function $\omega(y/\delta)$ is given by Coles, He further suggests that for a zero pressure gradient Π has the value 0.55.

Of direct consequence to this investigation is the measurement of wall shear. A great deal of data has been collected for wall shear due to turbulent flow over smooth walls. Nikuradse (1930) was able to confirm the existence of a law of the wall, as proposed by Prandtl, with measurements of shear stress and velocity in smooth pipes. Later, Ludwieg and Tillman (1949) proved the existence of a law of the wall for boundary layers using an ingenious heat transfer technique for indirect measurement of surface shearing stress. Preston (1954) developed a simple technique for measuring shear stress on smooth walls which depends on the universal law of the wall. He found that the pressure sensed by a round total head tube resting on the surface adjacent to a turbulent boundary layer is a universal function of the wall shear, tube diameter and the properties of the fluid. This technique remains today the most direct and simple method for the determination of wall shear on a smooth wall with turbulent flow.

The variation of surface shear on rough boundaries is a more complex problem. Early investigations of wall shear for turbulent flow near rough boundaries were generally restricted to observations of uniform flow in a pipe or flume, the value of the surface shear stress being inferred from the energy grade line, i.e., pressure gradient for pipe flow or channel slope in the case of the flume. The classic study

in this area is the investigation of flow through sand roughened pipes by Nikuradse (1933). He found that for high Reynolds numbers the pipe resistance factor defined as

$$\lambda = \frac{dp}{dx} \frac{4r}{\rho u_{av}^2} \tag{2.14}$$

where $\frac{dp}{dx}$ is the pressure gradient

r is the pipe radius

ρ is the fluid density

u_{av} is the average velocity in the pipe (flow rate divided by cross-sectional area)

was a function of relative roughness only:

$$\lambda = \frac{1}{(1.74 + 2 \log r/k_s)^2} \tag{2.15}$$

where k_s is the sand grain diameter. For lower Reynolds numbers, the pipe resistance factor is dependent on both the relative roughness and the Reynolds number. Other pipe flow investigations on "groove" and "depression" type roughness performed by Streeter and Chu (1949), Sams (1952) and Ambrose (1956) indicate a shear stress behaviour that is independent of the roughness height. This phenomenom is probably explained by the existence of a stable vortex in each roughness groove, with the major energy dissipation occurring in these vortices. Deepening the grooves probably has no influence on the size of these vortices, and the energy dissipation remains constant for a particular flow condition.

Experimental investigations of wall shear stress for the case of non-uniform flow over rough boundaries are few in number. The reason probably is that the simple methods of determining shear stress in uniform flow, or the Preston tube and Stanton tube techniques for smooth walls are not available. The first approach to the computation of the wall shear stress distribution on a rough plate was made by Prandtl and Schlichting (1934) by transposing and using the pipe flow data of Nikuradse

with the aid of the Von Karman momentum integral relation for a boundary layer with zero pressure gradient. This analytical investigation was extended by the experimental work of Schlichting (1937). Moore (1951) investigated the rough wall boundary layer in a zero pressure gradient. His roughness consisted of square rods placed normal to the flow and spaced a distance of 4 roughness heights apart. Three sizes of roughness were used; 1/8, 1/2, and 1 1/2 inch squares. He attempted to correlate his results with the analysis of Prandtl - Schlichting which was based on the distance, x, from the leading edge of the plate. This distance is ill defined, owing to the uncertainty of the flow conditions when the boundary layer thickness is comparable to the roughness height. Moore did find that there was a universal velocity defect law identical to the smooth wall law provided he properly selected the datum for measuring the distance from the wall and the boundary layer thickness to be some distance below the crest of the roughness. Clauser (1954), encouraged by Moore's result that the velocity defect law is independent of the roughness, developed a method for analyzing roughness effects which is the most useful to date. He found that the logarithmic velocity distribution given by

$$\frac{\bar{u}}{u_*} = \frac{1}{\kappa} \ln \frac{u_* y}{\nu} + A \tag{2.16}$$

undergoes a downward shift by an amount, $\frac{\Delta \bar{u}}{u_*}$, so that the logarithmic law may be written in the form

$$\frac{\bar{u}}{u_*} = \frac{1}{\kappa} \ln \frac{u_* y}{\nu} + A - \frac{\Delta \bar{u}}{u_*} \tag{2.17}$$

Nikuradse (1933) had established a logarithmic law of the wall in the form:

$$\frac{\bar{u}}{u_*} = \frac{1}{\kappa} \ln \frac{y}{k} + C \tag{2.18}$$

with the aid of the Von Karman momentum integral relation for a boundary layer with zero pressure gradient. This analytical investigation was extended by the experimental work of Schlichting (1937). Moore (1951) investigated the rough wall boundary layer in a zero pressure gradient. His roughness consisted of square rods placed normal to the flow and spaced a distance of 4 roughness heights apart. Three sizes of roughness were used; 1/8, 1/2, and 1 1/2 inch squares. He attempted to correlate his results with the analysis of Prandtl - Schlichting which was based on the distance, x, from the leading edge of the plate. This distance is ill defined, owing to the uncertainty of the flow conditions when the boundary layer thickness is comparable to the roughness height. Moore did find that there was a universal velocity defect law identical to the smooth wall law provided he properly selected the datum for measuring the distance from the wall and the boundary layer thickness to be some distance below the crest of the roughness. Clauser (1954), encouraged by Moore's result that the velocity defect law is independent of the roughness, developed a method for analyzing roughness effects which is the most useful to date. He found that the logarithmic velocity distribution given by

$$\frac{\bar{u}}{u_*} = \frac{1}{\kappa} \ln \frac{u_* y}{\nu} + A \tag{2.16}$$

undergoes a downward shift by an amount, $\frac{\Delta \bar{u}}{u_*}$, so that the logarithmic law may be written in the form

$$\frac{\bar{u}}{u_*} = \frac{1}{\kappa} \ln \frac{u_* y}{\nu} + A - \frac{\Delta \bar{u}}{u_*} \tag{2.17}$$

Nikuradse (1933) had established a logarithmic law of the wall in the form:

$$\frac{\bar{u}}{u_*} = \frac{1}{\kappa} \ln \frac{y}{k} + C \tag{2.18}$$

(the constant κ is assigned the value 0.41 by Clauser). By subtracting the second equation from the first. Clauser found the relation

$$\frac{\Delta\bar{u}}{u_*} = \frac{1}{\kappa} \ln \frac{u_* k}{\nu} + \text{const.} \qquad (2.19)$$

which holds for fully rough flow. Clauser found that Moore's data fit this expression very well.

Hama (1954) performed an experimental investigation of the flow over a plate roughened with wire screen. Four geometrically similar sizes of screen were used giving a 28-fold magnification of roughness height. He compared his data with Sarpkaya's flume data for the same roughness and found excellent agreement using Clauser's analysis. He also presents a comparison between Moore's data and flume data collected by Rand for a comparable roughness which again is in excellent agreement. Hama also proposes that further experimentation on roughened surfaces might just as well be performed in a pipe, since the data obtained can be easily extended to the case of a boundary layer. Perry and Joubert (1963) performed a set of experiments on a flat plate roughened in identically the same manner as Moore (1951), and analyzed their data in the same fashion as Hama. The difference was that the investigation was carried out under adverse pressure gradients. The data obtained correlated perfectly with that previously obtained with zero pressure gradient, confirming the original assumption that the law of the wall is independent of pressure gradient.

2.5 Turbulent Shear Flow near Smooth and Rough Boundaries: Investigation of Velocity and Pressure Fluctuation

The true nature of turbulence is still unknown and theoretical models proposed to date all depend on supplemental experimental data. Serious experimental investigations of turbulent shear flow began in the 1930's, but the classic investigations are the determinations of turbulence intensity in a two-dimensional channel and a pipe by Laufer (1951), (1954). This work was extended to the problem of a boundary layer in a zero pressure gradient by Klebanoff (1955). With the

improvement of the hot wire technique, a great deal of additional experimental data on turbulence intensity in air near smooth walls is now available. Limited data are available for liquid flow. Graveto (1967) analyzed the available turbulence data for smooth walls and concluded that turbulence intensity is primarily a function of wall shear.

Turbulence intensity data for flow over rough walls are few in number. The first significant study in this area appears to be the measurements of Tillman (1945) using a sand roughened plate. Following this study, Moore (1951) made some measurements on a plate roughened with square rods. Corrsin and Kistler (1955) determined the turbulence intensity in a boundary layer flow over a corrugated surface. Two studies have been made on the turbulence intensity following an abrupt change in roughness; in a pipe by Logan and Jones (1963), and in a two-dimensional channel by Carper, et. al., (1963). Recently, Robertson and Martin collected data in two pipes; one roughened with sand grains and the other having a "natural" roughness. All the above investigations used air at the test fluid.

Two studies of turbulence intensity in water flow over rough boundaries have been made. Fage (1933) used a two-dimensional channel with the walls roughened with a pattern of pyramids, similar to the knurling found on the handles of various hand tools and instruments. Turbulence intensity was inferred by the motion of small impurities in the water which were observed with a microscope. Only maximum turbulent velocities were reported. Liu, et. al., (1966) has made measurements in an open channel flume with a bottom roughened with square rods in the same fashion as Moore (1951). Qualitatively, the results agree with previous hot wire data, but a very large amount of scatter is evident.

Analysis of the meager results available to date indicates a strong dependency of turbulent intensity on wall shear. However, apparently the shape and relative height of the roughness is important in the region close to the wall.

Associated with turbulent velocity fluctuations are the temporal variations in static pressure. Taylor (1936) considered this problem and derived the relation

$$\sqrt{\overline{p'^2}} = \frac{\rho}{2} K \left(\overline{u_1'^2}\right) \qquad i = 1, 2, 3$$

$$1 < K < \sqrt{2} \qquad (2.20)$$

or $$\sqrt{\overline{p'^2}} = \frac{3}{2}\rho K \left(\overline{u'^2}\right) \quad \text{for isotropic turbulence} \tag{2.21}$$

where p' is the time varying component of static pressure

u_i' are the time varying components of velocity

ρ is the mass density of the fluid

Batchelor (1951) found a similar relationship for isotropic turbulence. Because of instrumentation problems, the actual measurements of p' in a shear flow are very limited. Rouse (1953) quotes some measurements in a turbulent jet and Strasberg (1963) presents some data for the turbulent wake behind a cylinder.

In a turbulent boundary layer, measurements of fluctuating pressure are limited to wall pressures. Kraichen (1956a) considered the problem theoretically and using some data of Laufer (1951) was able to show that the primary contribution to the pressure fluctuations in a turbulent boundary layer near a wall is the interaction of the turbulence with the wall shear. He predicts the value of the root mean square of the pressure fluctuations to be 6 times the magnitude of shear stress. Willmarth and Wooldridge (1962) measured the pressure fluctuations in air beneath a 5 inch thick boundary layer and found the root mean square wall pressure to be 2.19 times the wall shear. They also summarized the data of other investigations to date and concluded that the rms wall pressure-shear stress ratio decreases slightly with an increase in Reynolds number and surface roughness. They also found that most pressure disturbances are convected downstream with a speed approximately equal to 0.8 of the maximum velocity. Energy density spectra of the pressure fluctuations are similar to those for velocity fluctuation, and appear to have a universal form when they are normalized with respect to displacement thickness and maximum velocity. Bull, et. al., (1963) also made similar measurements and compared their results with all the previous investigations on the subject. They found that $\sqrt{\overline{p'^2}}/\tau_o$ increased from 2.11 at a momentum thickness Reynold's number of 6,400 to 2.80 at a Reynold's number of 33,800. This is in disagreement with the conclusion reached by Willmarth and Wooldridge (1962) after the analysis of several data for low speed flow. In this case, the Mach number was also increased in direct proportion to the increase in Reynold's number.

Maestrello (1965) found that $\sqrt{p'^2}/\tau_o$ increased with Mach number, over the same range of Mach number used in Bull's measurements. Maestrello also found a universal power spectrum for pressure fluctuations when the maximum velocity and the displacement thickness are used as a characteristic velocity and length respectively.

Little has been reported on the effect of roughness on the wall pressure fluctuations. Willmarth and Wooldridge (1962) made a limited study on a surface having natural roughness (tool nicks and scratches) which indicated a increase in $\sqrt{p'^2}/\tau_o$. Abecasis (1966) measured fluctuating wall pressure in a tilting flume using water and several types of rough concrete surfaces. Unfortunately, Abecasis did not study the statistical properties of the pressure fluctuations. He only reports the maximum negative peaks in wall pressure. This quantity is certainly ill-defined; however, if this peak is assumed to occur less than 5% of the time, its value would be equal to $1.64\sqrt{p'^2}$. Assuming this to be true, his data is in substantial agreement with the smooth wall data previously cited. There appear to be no detailed results available on the roughness effect on turbulent pressure fluctuations.

III. Theoretical Considerations

3.1 Introduction

This investigation is an experimental study of cavitation inception with particular emphasis on the effects of turbulence and boundary roughness. In order to place the experimental results in the proper context, it is necessary to review the available theory and to investigate the possible deviations from the theory. Basically, cavitation is caused simply by the fact that, owing either to convective or local accelerations in a flow field, the pressure at some point falls to a value low enough to permit the existence of both the liquid and gaseous phase. The analysis thus poses two questions: 1) what is the location and magnitude of the minimum pressure in a given flow field and 2) what is the value of pressure necessary to initiate the formation of the gaseous phase, i.e. cavitation. At first glance, the problem does not appear complex and for some engineering applications the cavitation problem can be simplified to the point that it is amenable to rapid calculation. On the other hand, there are many unanswered questions which depend either on the real fluid effects or on the details of the inception process or both. What has plagued many previous investigators is that it is difficult at times to place an observed deviation from a simple theory into the proper category for detailed analysis. It is necessary then to examine the existing theory, to thoroughly understand the assumptions that went into the analysis, and to investigate new theoretical approaches to explain observed deficiencies.

3.2 Fundamental Cavitation Law

If a fluid is considered to be incompressible and inviscid, the Bernoulli equation is known to apply in the form:

$$p_o + \rho\frac{U_o^2}{2} = p + \rho\frac{U^2}{2} \qquad (3.1)$$

where ρ is the fluid density

U_o is a reference velocity

p_o is a reference pressure

U is the local velocity

p is the local pressure

When considering the flow about immersed bodies, it is convenient to define a pressure coefficient in the form

$$C_p = \frac{p - p_o}{\rho \frac{U_o^2}{2}} \tag{3.2}$$

Thus, C_p has the value 1.0 at stagnation points and a minimum value at points of maximum velocity since from (3.1):

$$C_p = 1 - \left(\frac{U}{U_o}\right)^2 \tag{3.3}$$

It is also convenient to define the value of C_p at the point of minimum pressure (or maximum velocity) as

$$C_{pmin} = \frac{p_{min} - p_o}{\rho \frac{U_o^2}{2}} \tag{3.4}$$

The so-called cavitation index is defined as

$$\sigma = \frac{p_o - p_{vp}}{\rho \frac{U_o^2}{2}} \tag{3.5}$$

where p_{vp} is the vapor pressure of the liquid. It is obvious from the Bernoulli equation that this is a pertinent parameter <u>if</u> cavitation occurs at the vapor pressure p_{vp}. If this is true then the value of σ at the point of incipient cavitation is obtained by setting $p_{vp} = p_{min}$ or from (3.4) and (3.5):

$$\sigma_i = - C_{pmin} \tag{3.6}$$

Equation (3.6) is the fundamental equation of cavitation inception. Assuming cavitation to be, as stated, only a function of p_o, U_o, ρ and p_{vp}, it is clear dimensionally that σ is the only variable necessary to describe the flow. A simple case, for example, is the variation of lift on a hydrofoil with the cavitation index. Defining a lift coefficient

$$C_L = \frac{L'}{\rho \frac{U_o^2}{2} S_o} \tag{3.7}$$

where L' is the lift

S_o is the planform area

and neglecting viscosity and free surface effects, it follows from dimensional reasoning that

$$C_L = \psi(\sigma) \qquad \text{only} \tag{3.8}$$

This is illustrated in Figure 3.1. The minimum pressure coefficient on the surface of a typical hydrofoil at a mild angle of attack is -1.25. The solid lines indicate the variation of pressure coefficient over the upper and lower surfaces for non-cavitating flow. If the flow were truly inviscid, the value of C_p at the trailing edge, x/c = 1.0, would be 1.0, and the lift would be zero. The value of the lift coefficient is given by the integral

$$C_L = \int_0^1 (C_{pl} - C_{pu})\, d\left(\frac{x}{c}\right) \tag{3.9}$$

where C_{pl} is the value of C_p on the lower surface

C_{pu} is the value of C_p on the upper surface

c is the chord length

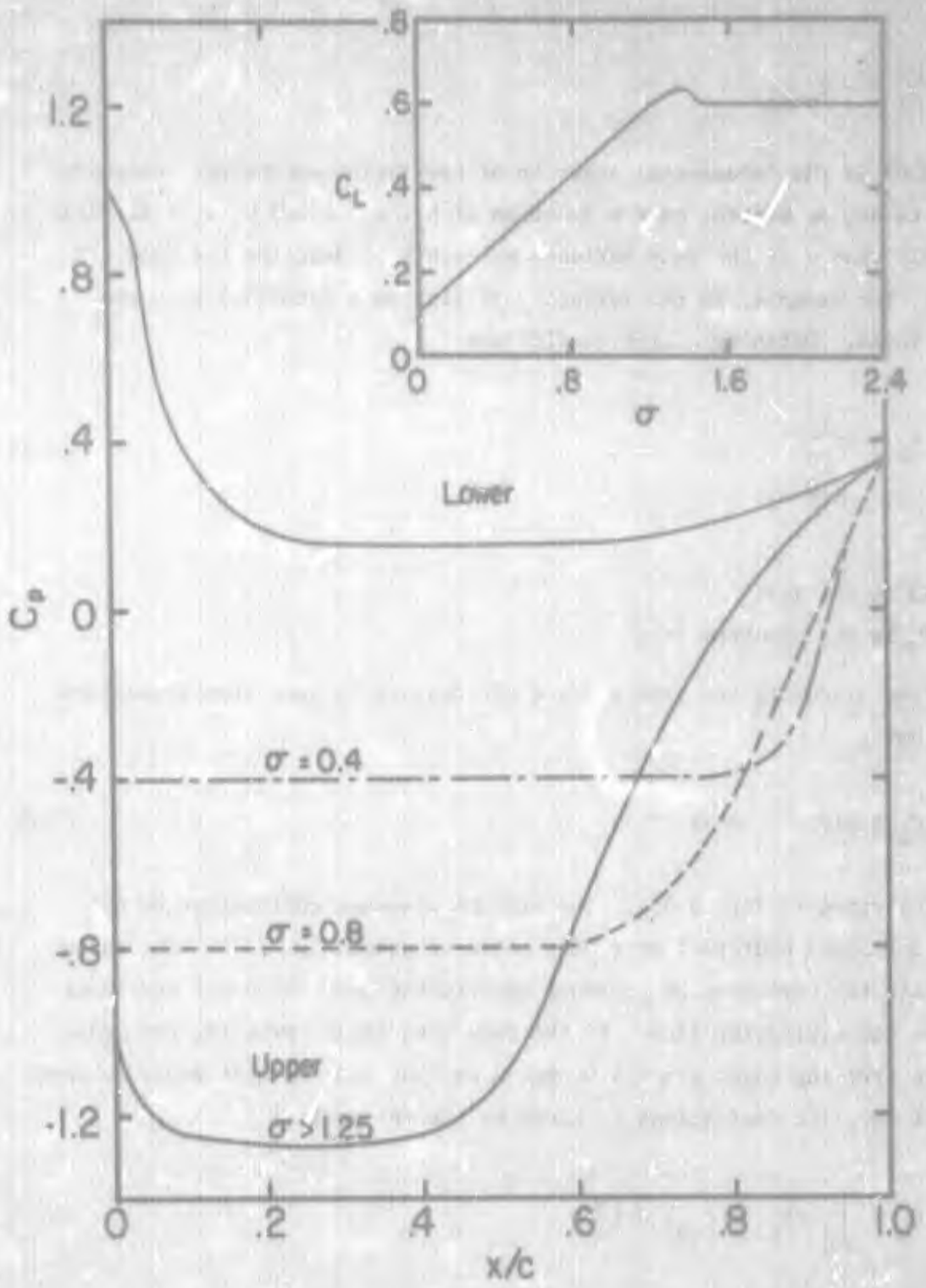

Figure 3.1: Variation of Hydrofoil Lift with Cavitation Index

For all values of σ greater than 1.25, C_L is a constant. However, as σ is lowered below 1.25, the flow field is modified since the minimum value of the static pressure is given by p_{vp}. Thus $-C_{pmin} = \sigma$ and the pressure distributions are modified as shown. From equation (3.9) it is obvious that C_L must be reduced in value. At the same time the flow remains no longer attached to the upper surface of the foil and a cavity is formed, the length of which is indicated by the zone of constant C_{pmin} as shown in Figure 3.1. The lift coefficient will decrease with a reduction in σ until $\sigma = 0$ where C_L attains its minimum value as shown. This is an elementary example of the dependence of performance on the cavitation index. However, in practice, the problem is much more complex.

3.3 Bubble Dynamics

To understand how the simple theory cited above can deviate from experiment, it is necessary to investigate the actual process of cavitation. The existence of small spherical bubbles (nuclei) in the flow is assumed. Following Rayleigh (1917) we consider a small spherical bubble in an incompressible, inviscid fluid. Gravity is neglected, and the motion is assumed to be axisymmetrical. With these assumptions any change in bubble size may be represented by a source flow. The velocity potential is given by

$$\phi = \frac{m}{r} \tag{3.10}$$

where r is the radial distance in spherical coordinates. The velocity of the bubble wall is given by $\frac{dR}{dt}$ where R(t) is the radius of the bubble and the boundary condition to be satisfied is

$$v = -\frac{\partial \phi}{\partial r} = \frac{dR}{dt} \quad @ \; r = R \qquad \text{where } v \text{ is the radial velocity.} \tag{3.11}$$

Substitution of (3.11) into (3.10) yields the strength of the source as

$$m = R^2 \frac{dR}{dt} \tag{3.12}$$

so that the velocity potential of the flow is given by

$$\phi = \frac{R^2R'}{r} \tag{3.13}$$

where the prime denotes differentiation with respect to time. The dynamic equation for unsteady flow is:

$$-\frac{\partial\phi}{\partial t} + \frac{p}{\rho} + \frac{v^2}{2} = F(t) \tag{3.14}$$

By substitution of (3.11) and (3.13) into (3.14) and letting $p = p_\infty$ at infinity, the following equation may be written

$$-\frac{R^2R'' + 2RR'^2}{r} + \frac{1}{2}\left(\frac{R^2R'}{r^2}\right)^2 = \frac{p_\infty - p(R)}{\rho} \tag{3.15}$$

where $p(R)$ is the pressure at the bubble wall. The equation of motion for the bubble wall is obtained by letting $r = R$:

$$RR'' + \frac{3}{2}(R')^2 = \frac{p(R) - p_\infty}{\rho} \tag{3.15a}$$

The pressure difference between the inside and the outside of the bubble may be obtained from the equilibrium between the partial pressure of vapor and gas inside the bubble, the surface tension and the external pressure thus

$$p(R) - p_\infty = p_{vp} + p_g - 2\frac{s}{R} - p_\infty \tag{3.16}$$

where p_{vp} is the vapor pressure
p_g is the partial pressure due to gas
s is the surface tension

Assuming isothermal conditions, and neglecting diffusion so that the weight of gas

W, remains constant within the bubble, the gas pressure is given by

$$p_g = \frac{3WNT}{4\pi R^3} \tag{3.17}$$

where W is the weight of gas
N is the gas constant
T is the absolute temperature

Letting $K = \frac{3WNT}{4\pi}$, Equation (3.15a) may be written in the form

$$RR'' + \frac{3}{2}(R')^2 = \frac{1}{\rho}\left[p_{vp} - p_\infty - \frac{2s}{R} + \frac{K}{R^3}\right] \tag{3.18}$$

This equation is fairly complex due to its non-linearity. However, several solutions for special cases have been cited in the literature. Rayleigh solved the problem for p_∞ = constant. An exact numerical solution for gaseous cavitation under a sinusoidal variation of p_∞ is given by Eller and Flynn (1965). In this solution the term K/R^3 is modified to allow gas diffusion. It is important to note that there are several assumptions inherent in the formulation of Equation (3.18):

1) inviscid flow
2) iso-thermal conditions
3) zero diffusion or heat transfer
4) vapor pressure is constant, i.e., time for vaporization or condensation is small compared to the bubble motion
5) spherical symmetry

A critical discussion of these assumptions is given by Plesset (1964). For this study the factors affecting growth, rather than collapse, are important. For large R we find that

$$\frac{2s}{R} \to 0 \qquad \frac{K}{R^3} \to 0$$

The right-hand side of (3.18) is bounded, and in a similar fashion the left-hand side must also be bounded; thus, equation (3.18) reduces to

$$R' = \sqrt{\frac{2}{3}\frac{p_{vp} - p_\infty}{\rho}} \tag{3.19}$$

Inspection of bubble growth data indicates that equation (3.19) is a good approximation a short time after initial growth.

3.4 Bubble Stability

As pointed out previously by Daily and Johnson (1956), an equation of static stability for a small bubble may be obtained. By setting the inertial terms to zero in equation (3.18), the equation for static equilibrium of a spherical bubble is obtained in the form

$$p_\infty - p_{vp} = \frac{K}{R^3} - \frac{2\sigma}{R} \tag{3.20}$$

By differentiating equation (3.20) with respect to R, a minimum value of $p_\infty - p_{vp}$ and a corresponding critical value of bubble radius is found which follows the relationship

$$p^* = -\frac{4\sigma}{3R^*} \tag{3.21}$$

where p^* is the minimum value of $p_\infty - p_{vp}$
R^* is the corresponding critical radius

Equations (3.20) and (3.21) are plotted in Figures 3.2 and 3.3 respectively. It is to be noted that with decreasing gas content (K→0), the value of the critical pressure approaches negative infinity. However, as the critical radius approaches dimensions of the same order as the liquid molecules, the theory is no longer valid. A theoretical analysis, which takes into account the molecular structure of the liquid predicts the possibility of tensions as high as 500 to 10,000 atmospheres.

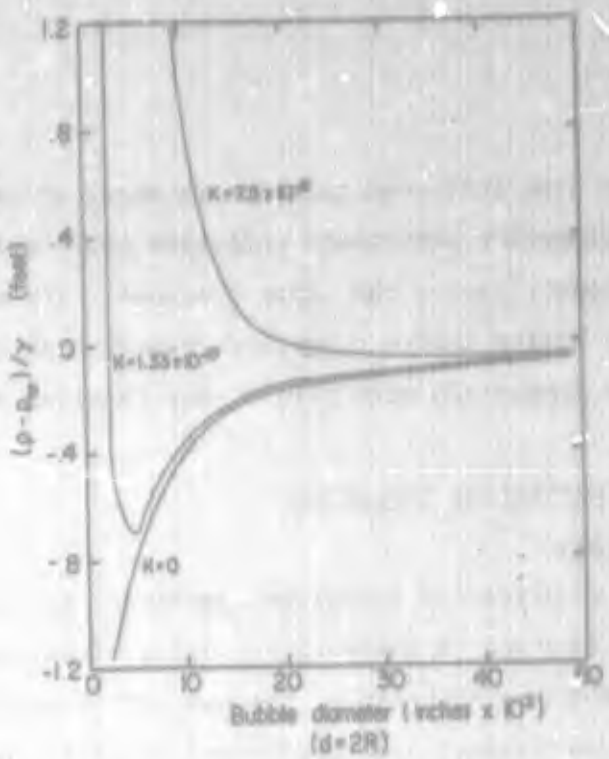

Figure 3.2: Static Equilibrium of Bubble

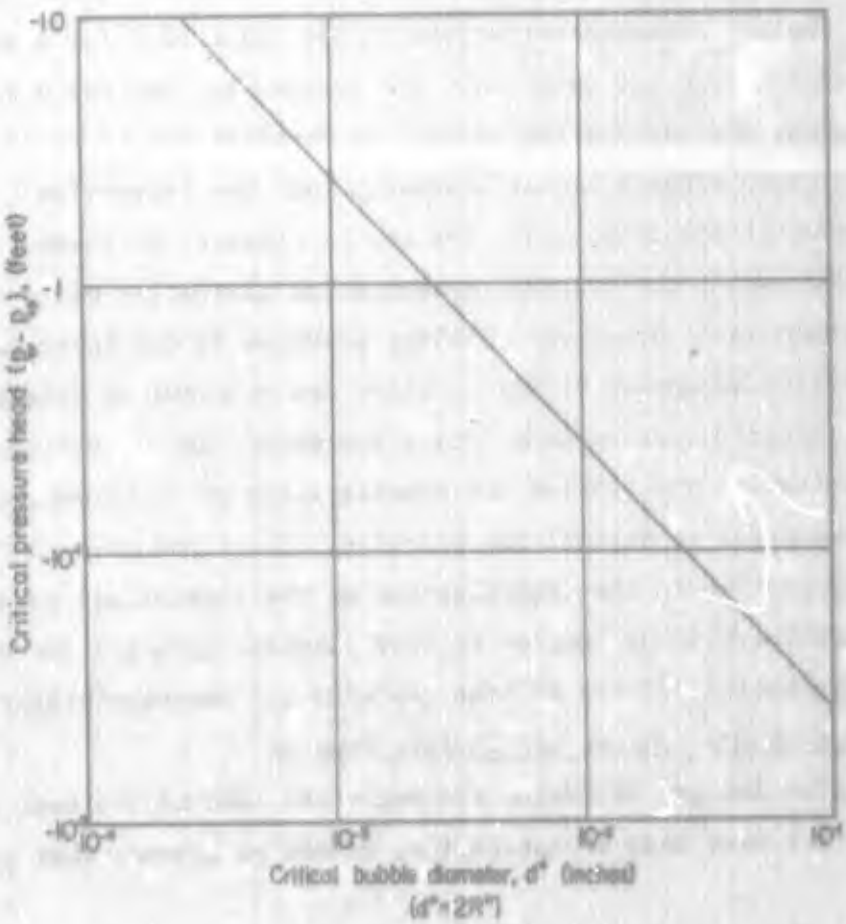

Figure 3.3: Variation of Critical Pressure with Critical Radius

Laboratory experiments have indicated tensions in water as high as 300 atmospheres. On the other hand, engineering experience indicates that cavitation generally occurs at a value of static head close to the vapor pressure. For such conditions, nuclei must exist in the flow having bubble diameters greater than 0.001 inch as shown in Figure 3.3. A further comparison with this theory is given in the discussion of results.

3.5 Scale Effects on Cavitation Inception

3.5.1 Introduction

The function of a cavitation inception experiment is to provide general information for the prediction of cavitation. Quite often, a model is used with a physical size less than the prototype. The cavitation scaling law infers that for geometrically similar bodies, flow conditions are the same when the cavitation index is equal in prototype and model, regardless of the differences in velocity and/or scale. Obviously, this can be true only if the original assumptions made in the cavitation scaling law are true, i.e., if it is dependent on ρ, U_o, p_o, and p_{vp} only. Reported variations in the value of σ for a particular shape with velocity or scale are numerous. The reasons for the scale effects are sometimes ill defined, and quite often are due to combinations of several influences. Primarily, these effects can be separated into two categories: 1) deviations from the Bernoulli equation, i.e., the static pressure no longer varies with the velocity squared and 2) the critical pressure for cavitation has a value different from the liquid vapor pressure. Scaling problems in the first category are classic, but cavitation inception brings to light new problems in this area, particularly when inception occurs away from a boundary. The second category is peculiar to cavitation and implies the consideration of fluid properties that are not normally important in engineering practice. The first step in the solution of the scaling problem is the determination of the significant parameters. The following discussion will be limited to cold liquids, having a low value of vapor pressure, eliminating effects of heat transfer and compressibility.

3.5.2 Effects of Gas Content and Surface Tension

If heat transfer and gas diffusion are neglected, and if the test liquid used has a gas content less than at saturation, it can be assumed that dynamically

similar cavitation inception will occur if

$$\frac{V_c}{U_o} = \text{constant}$$

where V_c is a characteristic velocity of the cavitation process. From equation (3.19), a characteristic velocity could be given by

$$V_c = \sqrt{\frac{p_{vp} - p_\infty}{\rho}} \tag{3.22}$$

and thus the required similarity condition would be

$$\frac{\sqrt{\frac{p_{vp} - p_\infty}{\rho}}}{U_o} = \text{constant} \tag{3.23}$$

At incipient cavitation, $p_\infty = p_{cr}$. If the critical pressure is equal to the vapor pressure, the similarity condition (3.23) is satisfied identically. To carry the similarity condition one step further, equation (3.21) is substituted into (3.23) and noting that $p^* = p_{cr} - p_{vp}$ the requirement for dynamically similar cavitation inception reduces to

$$\frac{\sqrt{\frac{s}{\rho R^*}}}{U_o} = \text{constant} \tag{3.24}$$

Equation (3.24) represents a Weber number criterion in which the length parameter is given by the size of the nuclei rather than by a characteristic length of the body. This difficulty has probably plagued investigators for many years.

The influence of gas content is also an important feature. This presents a two-fold problem: first, the effects are not readily determined and secondly, an effective method of distinguishing between dissolved and undissolved gas content is not at hand. The scaling parameter cited above was derived by assuming a gas content less than saturation. If saturation is reached, the gas pressure

in a bubble is given by Henry's law:

$$p_g = \alpha\beta \tag{3.25}$$

where α is the gas content, ppm

β is Henry's constant, psi/ppm

Static equilibrium of the bubble is then given by

$$p_\infty - p_{vp} = \alpha\beta - \frac{2s}{R} \tag{3.26}$$

In this case, the critical radius is not defined. The critical pressure is defined as the point where the internal gas pressure reaches the saturation value. As indicated by equation (3.26), the critical pressure will be greater than the vapor pressure for $R > \frac{2s}{\alpha\beta}$. Such a situation is typical of gaseous cavitation. The characteristic velocity can no longer by defined by equation (3.22) since substitution of Henry's law into the Rayleigh equation would give $V_c = 0$ for large R. This is not an unexpected result since the characteristic velocity would be a function of a gaseous diffusion process rather than of the dynamics of the process. Following Holl (1960), it is easy to see that an apparent scale effect with velocity can result with a saturated liquid. Assuming gas content to be the only scale effect, and neglecting surface tension, the critical pressure is given by $(p_{vp} + \alpha\beta)$. If cavitation occurs when $p_{min} = \alpha\beta + p_{vp}$, the corrected scaling parameter would be

$$\sigma_s = \frac{p_o - (\alpha\beta + p_{vp})}{\rho \frac{U_o^2}{2}} \tag{3.27}$$

and by analogy with equation (3.6) the incipient cavitation law would be

$$\sigma_{si} = -C_{pmin} \tag{3.28}$$

However, if the standard definition of the cavitation index is used, the incipient condition is given by the relation:

$$\sigma_i = - C_{pmin} + \frac{\alpha\beta}{\rho \frac{U_o^2}{2}} \tag{3.29}$$

where the term $\frac{\alpha\beta}{\rho(U_o^2/2)}$ represents a scale effect. On the other hand, for under-saturated liquids, the critical pressure is less than the vapor pressure and a scale effect with velocity would be given by

$$\sigma_i = - C_{pmin} - \frac{p_{vp} - p_{cr}}{\rho \frac{U_o^2}{2}} \tag{3.30}$$

where $p_{cr} < p_{vp}$

In both cases σ approaches $- C_{pmin}$ for high velocity but for low velocities, high gas content implies $\sigma_i > -C_{pmin}$ and low gas content implies $\sigma_i < -C_{pmin}$. Both trends have been reported in the literature for different cases.

3.5.3 Turbulence Effects

The primary effect of turbulence on cavitation is the existence of a fluctuating component of pressure in the flow field. The predominant factor for inception is no longer the minimum value of the mean static pressure, but rather the magnitude of the negative peaks of the turbulent pressure fluctuations. A general analytical solution to this problem is evidently not feasible. However, it is useful in this connection to review the general formulation of flow conditions in a turbulent, two-dimensional boundary layer.

The equations of motion and continuity for an incompressible fluid in tensor notation are given by

$$\frac{\partial u_i}{\partial t} + u_j \frac{\partial u_i}{\partial x_j} = - \frac{1}{\rho} \frac{\partial p}{\partial x_i} + \nu \frac{\partial^2 u_i}{\partial x_j^2} \tag{3.31}$$

$$\frac{\partial u_i}{\partial x_j} = 0 \tag{3.32}$$

Each instantaneous component of velocity and pressure is assumed to be composed of a mean component (independent of time) and a fluctuating component:

$$u_i = \bar{u}_i + u_i' \tag{3.33a}$$

$$p = \bar{p} + p' \tag{3.33b}$$

Substitution into the equations of motion and continuity results in:

$$\frac{\partial u_i'}{\partial t} + (\bar{u}_j + u_j') \frac{\partial (\bar{u}_i + u_i')}{\partial x_j} = -\frac{1}{\rho} \frac{\partial (\bar{p} + p')}{\partial x_i} + \nu \frac{\partial^2}{x_j^2} (\bar{u}_i + u_i') \tag{3.34}$$

$$\frac{\partial u_i'}{\partial x_j} + \frac{\partial \bar{u}_i}{\partial x_j} = 0 \tag{3.35}$$

The temporal mean of the continuity equation (3.35) is given by

$$\frac{\partial \bar{u}_i}{\partial x_j} = 0 \tag{3.36}$$

It follows that

$$\frac{\partial u_i'}{\partial x_j} = 0 \tag{3.37}$$

By multiplying equation (3.37) by u_i', adding the result to equations (3.34) and taking the mean, the familiar Reynolds equations result (for steady mean-flow):

$$\bar{u}_j \frac{\partial \bar{u}_i}{\partial x_j} = -\frac{1}{\rho}\frac{\partial \bar{p}}{\partial x_i} + \nu \frac{\partial^2 \bar{u}_i}{\partial x_j^2} - \frac{\partial (\overline{u_i' u_j'})}{\partial x_j} \tag{3.38}$$

The equations of motion for the fluctuating components are obtained by subtracting equations (3.38) from equations (3.34):

$$\frac{\partial u_i'}{\partial t} + \frac{\partial}{\partial x_j}\left[(\bar{u}_j + u_j')u_i' + u_j'\bar{u}_i - \overline{u_j' u_i'}\right] = -\frac{1}{\rho}\frac{\partial p'}{\partial x_i} + \nu \frac{\partial^2 u_i'}{\partial x_j^2} \tag{3.39}$$

The mean flow equations may be considerably simplified by applying the usual boundary layer considerations (cf Schlichting [1960]):

$$\bar{u}\frac{\partial \bar{u}}{\partial x} + \bar{v}\frac{\partial \bar{u}}{\partial y} = -\frac{1}{\rho}\frac{\partial \bar{p}}{\partial x} + \nu \frac{\partial^2 \bar{u}}{\partial y^2} - \frac{\partial (\overline{u'v'})}{\partial y} \tag{3.40}$$

$$\frac{\partial \bar{p}}{\partial y} + \rho \frac{\partial \overline{v'^2}}{\partial y} = 0 \tag{3.41}$$

$$\frac{\partial \bar{u}}{\partial x} + \frac{\partial \bar{v}}{\partial y} = 0 \tag{3.42}$$

wherein the tensor notation has been dropped. Equation (3.41) may be integrated directly, resulting in the relation:

$$\bar{p} + \rho \overline{v'^2} = \text{constant} \tag{3.43}$$

Thus, the mean static pressure is a minimum where the velocity fluctuations normal to the wall are a maximum.

An expression for the fluctuating component of the static pressure may be obtained by operating on equations (3.39) by $\partial/\partial x_i$ and adding the resulting equation together with the continuity relationship to obtain

$$\frac{\partial^2 p'}{\partial x_j^2} = -\rho \frac{\partial^2}{\partial x_i \partial x_j}\left[(\bar{u}_j + u_j')u_i' + u_j'\bar{u}_i - \overline{u_j' u_i'}\right] \tag{3.44}$$

Kraichen (1956a) simplified equation (3.44) for two-dimensional boundary layers to the form

$$\frac{\partial^2 p'}{\partial x_j^2} = -2\rho \frac{\partial \bar{u}}{\partial y} \frac{\partial v'}{\partial x} \qquad (3.44a)$$

This equation is derived by assuming that $\bar{v} = \bar{w} = 0$, $\bar{u}$ is a function of y only and $u'/\bar{u} \ll 1$. Kraichen (1956a) justified his simplifications by an order of magnitude analysis using Laufer's (1951) data for a two-dimensional channel. In this case the assumptions $\bar{v} = \bar{w} = 0$ are identically satisfied. No proof was offered as to whether the same assumptions hold in a developing boundary layer. Willmarth and Wooldridge (1963) however demonstrated that the simplifications are justified in a boundary layer for wall pressure. Equation (3.44a) implies a predominant interaction between the turbulence and the mean shear. This has further implications for the problem of distributed roughness, since only a knowledge of the dependence of wall shear on the roughness properties would be required to determine the intensity of pressure fluctuations.

3.5.4. Roughness Effects and a Proposed Boundary Layer Cavitation Law

a.) As mentioned previously, the roughness problem may be dealt with in two categories, one of isolated irregularities and the other of distributed roughness. Cavitation inception due to an isolated irregularity on a parent body is primarily a local effect. Holl (1959) has demonstrated that this problem may be solved if the following information is known:

1. The smooth wall boundary layer thickness and the shape factor in the vicinity of the roughness.
2. The pressure distribution on the parent body.
3. The roughness height and the incipient cavitation index for the roughness alone (i.e., an individual roughness irregularity on a flat plate).

A minimum pressure coefficient may be defined for the parent body with a small roughness irregularity as:

$$C_{pminR} = \frac{p_{minR} - p_o}{\rho \frac{U_o^2}{2}} \qquad (3.45)$$

where p_{minR} is the local minimum pressure near the roughness protrusion

p_o is the static pressure in the undisturbed flow

U_o is undisturbed free stream velocity

Equation (3.45) may be rewritten in the form

$$C_{pminR} = \frac{p - p_o}{\rho \frac{U_o^2}{2}} + \frac{p_{minR} - p}{\rho \frac{U^2}{2}} \left(\frac{U}{U_o}\right)^2 \qquad (3.46)$$

where p is the local pressure outside of the boundary layer

U is the local velocity at the edge of the boundary layer

Assuming that the small irregularity does not affect the large scale motion about the body, the local pressure coefficient for a smooth body without the irregularity is given by

$$C_p = \frac{p - p_o}{\rho \frac{U_o^2}{2}} \qquad (3.47)$$

thus, also (see equation 3.3):

$$\left(\frac{U}{U_o}\right)^2 = 1 - C_p \qquad (3.48)$$

Defining the cavitation index for the isolated roughness on a flat plate as

$$\sigma_{iR} = \frac{p - p_{vp}}{\rho \frac{U_o^2}{2}}$$

and assuming cavitation inception to occur when $p_{vp} = p_{minR}$, the cavitation index for the body, defined in the standard manner is

$$\sigma_i = - C_p + \sigma_{iR}(1 - C_p) \qquad (3.49)$$

where C_p is the value of the pressure coefficient at the location of the roughness protrusion. If the isolated irregularity is located in a high pressure region, near a stagnation point, for example, the inception index defined by (3.49) might still be lower than the absolute value of the minimum pressure coefficient. In this case equation 3.6 would still apply (neglecting other scale effects):

$$\sigma_i = - C_p \tag{3.6}$$

The most unfavorable condition exists when the isolated irregularity is located on the body at the minimum pressure point. Then, the ratio between the inception indices for the body with and without the irregularity is given by

$$\frac{\sigma_i}{\bar{\sigma}_i} = 1 + \sigma_{iR} \frac{(1 + \bar{\sigma}_i)}{\bar{\sigma}_i} \tag{3.50}$$

where $\bar{\sigma}_i$ is the cavitation index without the roughness. The percentage increase in the cavitation index due to an isolated triangular projection located at the minimum pressure point on a hydrofoil was computed by Holl (1959) for the case where $\bar{\sigma}_i = 0.5$ and using his experimental value for σ_{iR} obtained on a flat plate with the boundary layer thickness 0.048 inches at the point in question. The results are shown in Table 3.1.

Table 3.1

Typical Increase in Cavitation-Index due to an Isolated Irregularity for $\delta = 0.048$ inches

k	k/δ	σ_{iR}	σ_i	Percent increase in $\bar{\sigma}_i$
0.001	0.021	0.34	1.01	102
0.002	0.042	0.45	1.18	135
0.004	0.083	0.67	1.50	201
0.008	0.167	0.90	1.85	270

If the value of σ_{iR} is not known, an estimate of σ_{iR} is given by:

$$\sigma_{iR} = \left(\frac{\bar{u}_k}{U}\right)^2 \sigma_{iR\infty} \qquad (3.51)$$

where $\sigma_{iR\infty}$ is the inception for the roughness in a free stream (i.e. $k/\delta = \infty$)

$\bar{u}_k$ is the local velocity at the tip of the roughness

b) For a surface having a distributed roughness, the problem is more complex. The boundary layer parameters are directly related to the wall roughness and cannot be estimated by neglecting its influence as is done for an isolated irregularity. In addition, each protuberance is directly influenced by the presence of adjacent irregularities, making it impossible to use any data for inception obtained for an isolated projection. However, for closely spaced roughness, the nature of the turbulent fluctuations, and the resulting temporal variations in static pressure are probably quite independent of the particular protuberance shape at distances from the wall of one or two roughness heights. Further, it may be assumed that the turbulence intensities are directly related to the wall shear:

$$\frac{\sqrt{\overline{u'^2}}}{u_*} = F(y/\delta) \text{ only} \qquad (3.52)$$

It is also assumed that the pressure fluctuations, p', and the velocity fluctuations, u', are related:

$$\sqrt{\overline{p'^2}} \sim \rho\sqrt{\overline{u'^2}} \qquad (3.53)$$

The difference between the mean static pressure at the wall, p_{wall} and the negative peak of the pressure fluctuations, p_{min} is given by

$$p_{wall} - p_{min} = C_1\sqrt{p'^2} \tag{3.54}$$

Combining equations (3.52), (3.53), and (3.54) and normalizing with respect to the free stream dynamic pressure, $\rho\frac{U^2}{2}$ results in the relation

$$\frac{p_{wall} - p_{min}}{\rho\frac{U^2}{2}} = 2C_2\left(\frac{u_*}{U}\right)^2 = C_2C_f \tag{3.55}$$

where C_f is the local skin friction coefficient, $\tau_o/\rho\frac{U^2}{2}$
Defining a local incipient cavitation index to be

$$\sigma_{il} = \frac{p_{wall} - p_{vp}}{\rho\frac{U^2}{2}} \tag{3.56}$$

and assuming cavitation when $p_{min} = p_{vp}$ the following significant general law is obtained

$$\sigma_{il} = C_2C_f \tag{3.57}$$

This law applies for <u>smooth</u> or <u>rough</u> boundaries.

If the wall roughness does not severely change the overall mean pressure distribution, a cavitation inception law for bodies with distributed roughness may be derived by analogy to the law for an isolated irregularity:

$$\sigma_i = -C_p + C_2C_f(1 - C_p) \tag{3.58}$$

It should be noted that in equation (3.58) both C_p and C_f are functions of position on the body. Thus, a trial and error solution is required for the minimum value of σ_i along the boundaries of the body. However, a simplification of equation (3.58) is possible if the inception point on the body is located where the mean local pressure is a minimum. Cavitation inception is then given by the relation:

$$\sigma_i = \bar{\sigma}_i + C_2 C_f (1 + \bar{\sigma}_i) \tag{3.59}$$

and the ratio between inception indices for a roughened and a smooth body may be stated as:

$$\frac{\sigma_i}{\bar{\sigma}_i} = 1 + C_2 C_f \frac{(1 + \bar{\sigma}_i)}{\bar{\sigma}_i} \tag{3.60}$$

The determination of the constant C_2 is one of the objectives of this study. The analysis of previous turbulence data and order of magnitude considerations outlined under "turbulence effects" indicate that C_2 should essentially be a universal constant.

3.5 Review of Boundary Layer Theory

A method for correlating the experimental results for the determination of skin friction over a wide range of cases has been suggested by Clauser (1954). This method is pertinent to this investigation and is presented here because of its use in this study.

In the region close to the wall, two velocity distribution laws are known to apply

$$\frac{\bar{u}}{u_*} = 5.6 \log\left(\frac{u_* y}{\nu}\right) - \frac{\Delta\bar{u}_1}{u_*} + 5.1 \tag{3.61}$$

$$\frac{(\bar{u} - U)}{u_*} = 5.6 \log\left(\frac{u_* y}{U\delta_*}\right) - \frac{\Delta\bar{u}_2}{u_*} + 0.6 \tag{3.62}$$

where $\frac{\Delta\bar{u}_1}{u_*}$ is the displacement from the smooth wall law

$\frac{\Delta\bar{u}_2}{u_*}$ is the displacement from the velocity defect law for zero pressure gradient

δ_* is the displacement thickness

y is the distance from the wall

u_* is the shear velocity, $\sqrt{\tau_o/\rho}$

$\Delta\bar{u}_1/u_*$ is independent of pressure gradient, whereas $\Delta\bar{u}_2/u_*$ is independent of roughness. These quantities may be stated as:

$$\frac{\Delta u_1}{u_*} = \psi_1\left(\frac{u_* k}{\nu}\right) \tag{3.63}$$

$$\frac{\Delta u_2}{u_*} = \psi_2\left[\frac{U}{u_*}\left(\frac{H-1}{H}\right)\right] \tag{3.64}$$

where H is the shape factor defined as the ratio between displacement and momentum thickness. By defining the parameters

$$F_1 = 10^{\frac{\Delta\bar{u}_1}{5.6u_*}} \tag{3.65}$$

$$F_2 = 10^{\frac{\Delta\bar{u}_2}{5.6u_*}} \tag{3.66}$$

and substracting equation 3.62 and 3.61, a universal skin friction law results:

$$\frac{U}{u_*} = \sqrt{\frac{2}{C_f}} = 5.6 \log \frac{F_2}{F_1} \mathrm{IR}_{\delta_*} + 4.5 \tag{3.67}$$

where $\mathrm{IR}_{\delta_*} = U\delta_*/\nu$. For a smooth flat plate equation 3.67 reduces to

$$\sqrt{\frac{2}{C_f}} = 5.6 \log \mathrm{IR}_{\delta_*} + 4.5 \tag{3.68}$$

Further consideration is given to this law in the discussion of the experimental results.

IV. EXPERIMENTAL EQUIPMENT AND PROCEDURES

4.1 Introduction

Essentially four types of experiments were run during this research program; mean velocity profiles, turbulence intensity, visual observation of cavitation inception and high-speed photography of cavitation. Each phase of the experimental research was dependent on the other, the final goal being the correlation of the observed environmental parameters and the cavitation process with available theory.

4.2 General Description of Water Tunnel

The water tunnel used in this facility is shown schematically in Figure 4.1. The overall configuration is similar in design to other modern water tunnels being of the closed loop, closed jet type. Water is circulated through the facility by a pump (p), driven by a 7 1/2 horsepower DC motor (j). The use of a DC motor allowed variation of velocity by simply changing the speed of the motor. Turning vanes (a) are used to guide the flow into a stilling section (b). At this point an air-tight dome (c) is located; the pressure level above the free surface in this dome may be adjusted from 2.5 feet of water absolute to approximately 100 feet absolute. Downstream of the stilling section the flow passes through a chamber (d) filled with a honeycomb which acts as a flow straightener and turbulence attenuator. Following the honeycomb is a transition from round to rectangular cross-section (e). A two-dimensional nozzle (f) accelerates the flow into the test section (g). The test section consists of a rigid brass frame to which are attached removable, transparent side walls, a roof and a bottom plate. Overall dimensions of the test section are 1 1/2 inches high, 6 inches wide and 30 inches long. After the test section there is a parabolic transition (h) from the parallel walls of the test section to the divergent walls of the diffuser (i). After the diffuser, the flow returns to the pump as shown in the figure. Provision is made for continuous by-pass filtering of the flow at (k) and for constant temperature operation by continuously by-passing a portion of the flow through a heat exchanger (o). Cooling water for this heat exchanger comes from a large reservoir located in the basement of the M.I.T. Hydrodynamics Laboratory, which acts as a large heat sink for the water tunnel. A vacuum pump is used to evacuate a surge tank (m). This tank serves as a source of vacuum for the control of the pressure level in the tunnel. For pressures above atmospheric the compressed air supply in the laboratory is utilized.

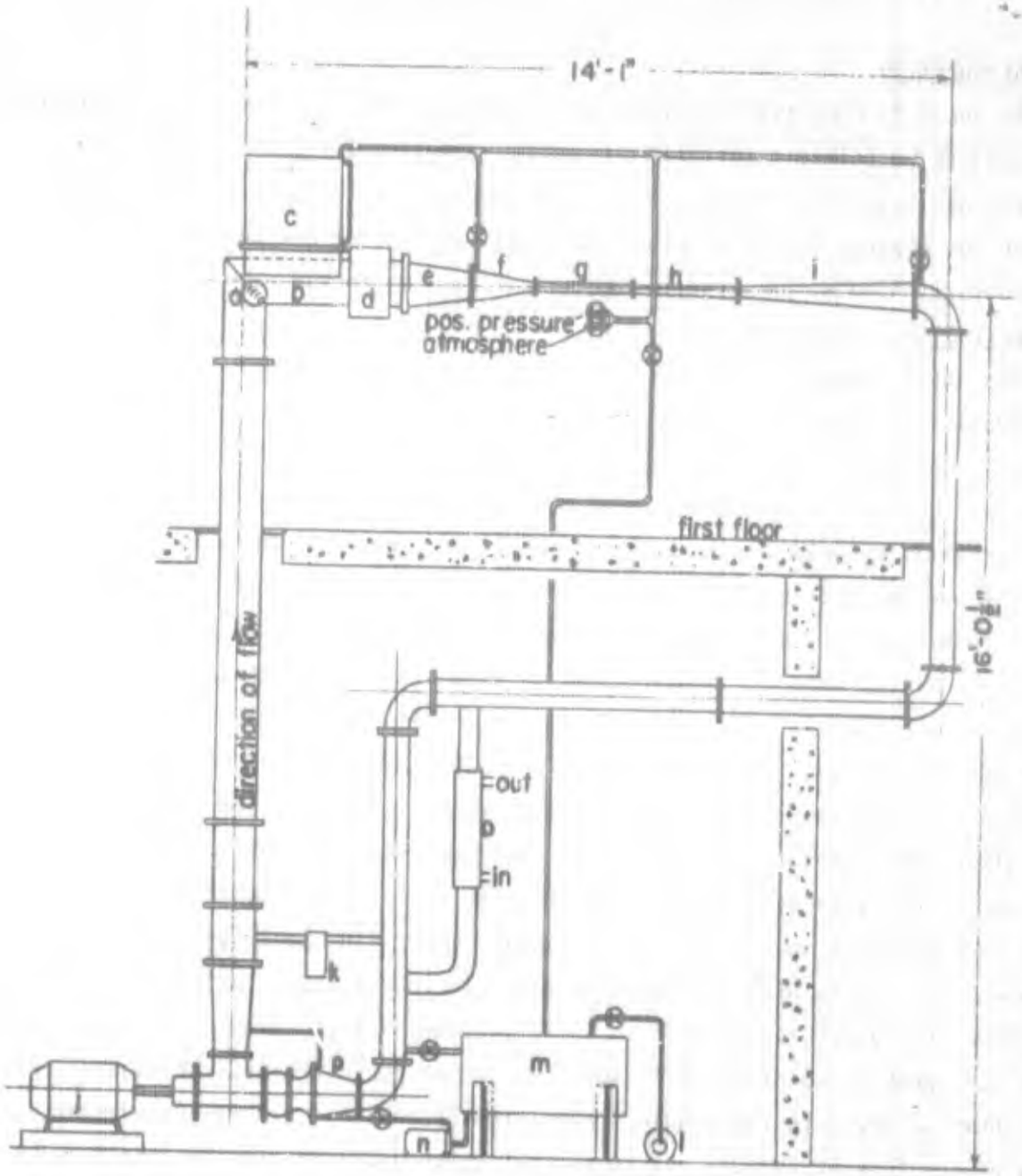

Figure 4.1: Schematic of Water Tunnel

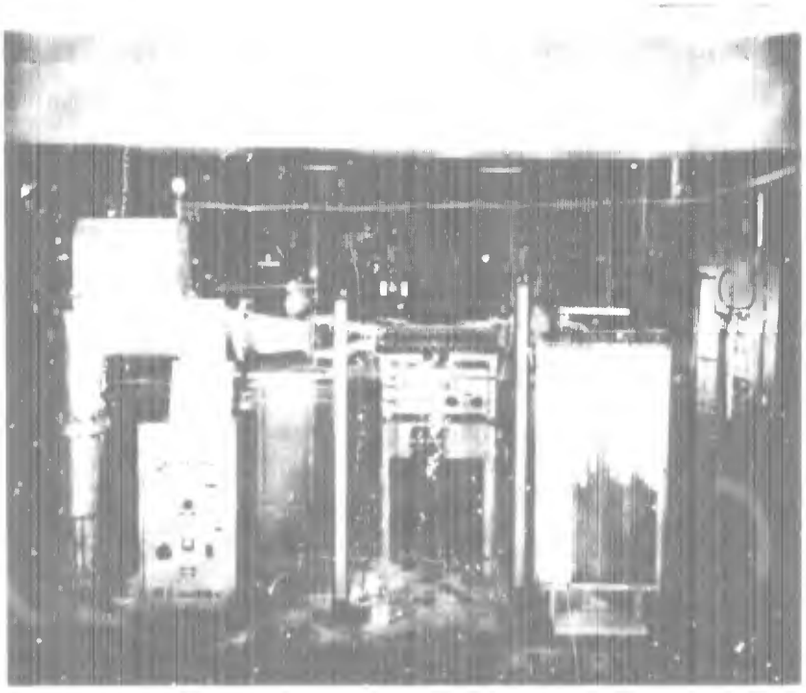

Figure 4.2: View of Upper Portion of Tunnel

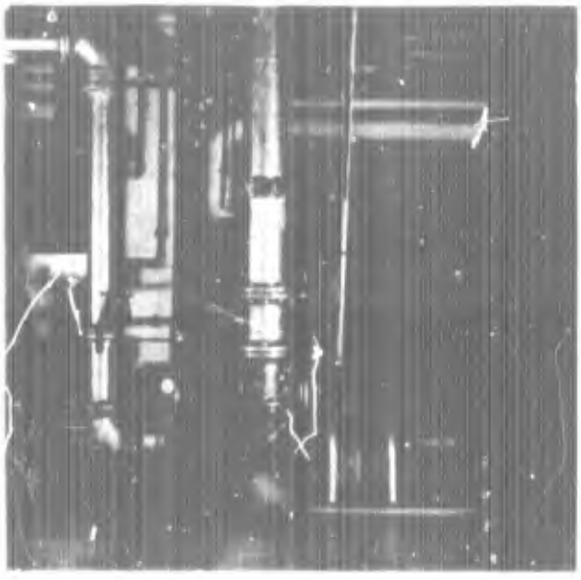

Figure 4.3: View of Lower Portion of Tunnel

Both the pressure piping and vacuum piping are connected to a special pressure regulator (a Cartesian Manostat #8, manufactured by the Manostat Corporation, N.Y.). By suitable valving, the same instrument is used for precise control of both vacuum and pressure. Except for modifications and improvements in the pumping system, flow straightener, test section, pressure control, filtering and cooling systems this facility is the same as that used by Daily and Johnson (1955), Benson (1958), and Daily, et. al., (1959).

4.3 Test Section Details

An overall view of the test section itself is shown in Figure 4.4. The important features are the bottom profile and various roofs used in this study. As shown in Figure 4.15, the bottom consists of an elliptical lip, a sloping section and an s-shaped transition to the horizontal. This design was selected to allow for boundary layer growth and to insure cavitation inception in the boundary layer adjacent to the roof. Altogether, six different roofs were used in this study, one smooth and five roughened roofs. Each roof had piezometer taps at seven stations along the plate. Except for the smooth plate, there are two piezometer holes at each station. The holes are 1/64 inch in diameter and are located two inches apart, straddling the centerline of the tunnel. Provision is made for blocking off piezometer taps with brass plugs when not in use. Each roof is roughened over a length of 22 inches with triangular grooves transverse to the flow. Nominal depth of the grooves is 0.100, 0.050, 0.025, and 0.0125 inches respectively. For geometric similarity, the peak to peak distance between grooves in each roof is equal to twice the roughness height. The first roof made for this study had triangular roughness protrusions 0.100 inch high. Cavitation occurred upstream at the first roughness element due to local acceleration of the fluid. Since it was desired to have cavitation inception downstream in the thickest portion of the boundary layer, all additional roofs were made with grooves which were identical to the protrusions. The peaks are flush with a smooth entrance section and allow a cavitation free transition from the smooth to the roughened portion of the roof.

Piezometer taps in the roughened portion are located on islands having a smooth surface level with the peaks of the roughness. The islands are 7/8 inch long by 1/4 inch wide. Details of the roofs and piezometer taps are shown in Figure 4.6. Table 4.1 lists the location of piezometer taps relative to the intersection between the test

Figure 4.4: Photograph of Test Section

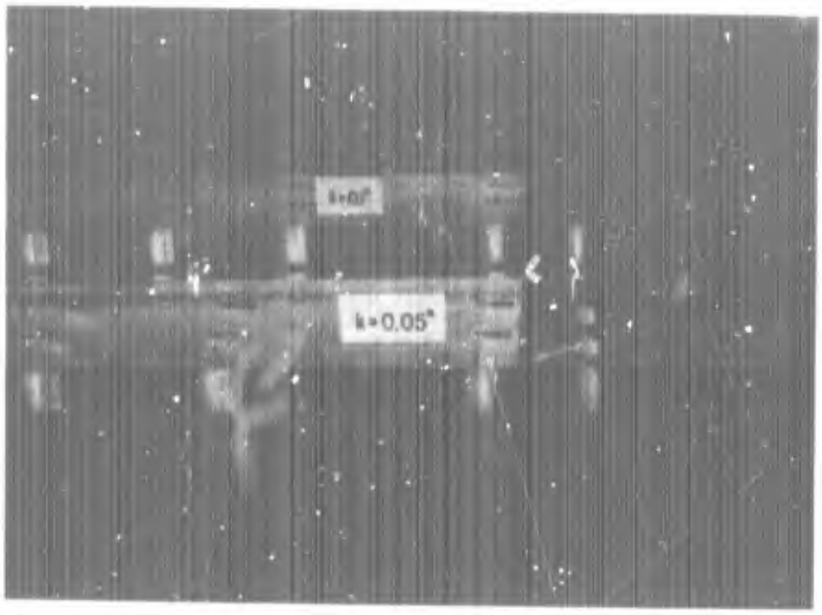

Figure 4.5: Photograph of Rough Roofs

section and the nozzle. Also given is the range of relative roughness in terms of the ratio of distance, x, and the nominal roughness height, k.

Table 4.1
Location of Piezometer Taps

Station	X	Relative Distance from Nozzle, x/k				
	(in)	Roof # (1)	(2)	(3)	(4)	(5)
1	2.5			Smooth Wall		
2	5.0	50	50	100	200	400
3	11.4	114	114	228	456	912
4	15.8	158	158	316	632	1264
5	20.1	201	201	402	804	1608
6	22.45	224.5	224.5	449	898	1796
7	27.30			Smooth Wall		

The smooth roof used in the preliminary phases of this study was identical in overall dimensions and had additional piezometer taps located along the centerline.

Corresponding to each piezometer station in the roof there is a 0.120 inch hole in the bottom. The holes are located along the centerline and at each station are located 1/2 inch further downstream than the piezometer taps. Instrumentation for mean velocity and turbulence measurements are inserted through these holes. Sealing is accomplished with o-rings. The 1/2 inch offset allowed the tip of the velocity probe to be in line with the piezometer holes.

4.4 Mean Velocity Measurement

Mean velocity measurements were made primarily with a total head tube fabricated from 0.027 inch O.D. hypodermic tubing. This device was inserted into the test section through one of the holes in the bottom of the test section. A micrometer traversing device (Figure 4.7) was used for moving the tube in and out of the roof boundary layer. Distance from the roof was read directly to 0.001 inch. The lead from the total head tube was connected to one leg of a well type differential manometer, and the leads from two adjacent static taps in the roof were connected to the other leg of the manometer. The reading on the manometer was

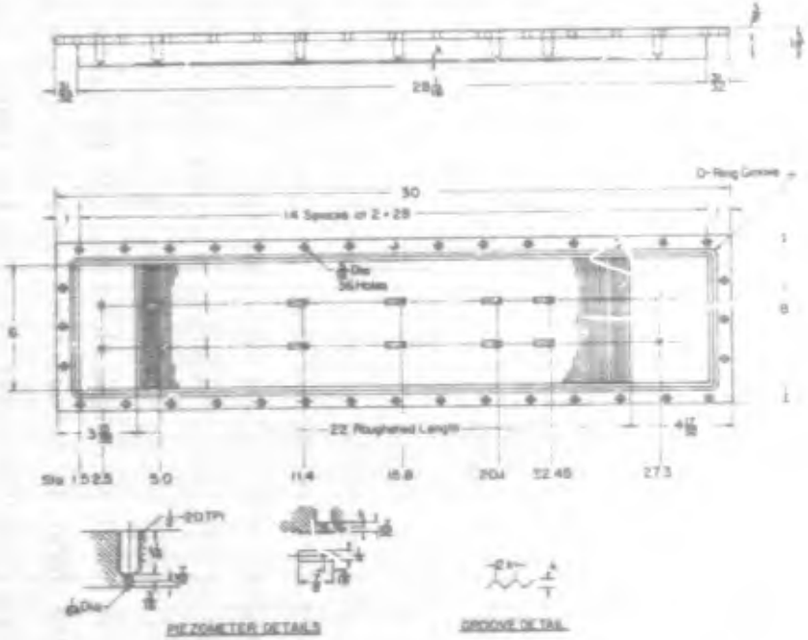

Figure 4.6: Details of Roof

Figure 4.7: Probe Traversing Device

then proportional to the local velocity head, except for minor variations in mean static pressure through the boundary layer. Mercury was used as the manometer fluid for nearly all phases of the test program, with the exception of a few low speed boundary layer traverses which were made using Meriam D-9325 Manometer Fluid. The probe was calibrated in a small free jet wind tunnel which was fabricated for the purpose. Details of the tunnel are given in the Appendix. At the same time, an 0.035 inch O.D. pitot static probe described by Daily, et. al., (1959), and two larger total head probes used for turbulence measurements were calibrated. The results are tabulated in Table 4.2. The calibration coefficient is defined as

$$C_p = \frac{\Delta p}{\rho U_{o/2}^2}$$

where Δp is the pressure difference sensed by the tube and $\rho U_{o/2}^2$ is the wind tunnel dynamic pressure. The probe Reynolds number listed in the table is based on either the tube diameter or the tip thickness in the case of the flattened probe.

Table 4.2

Summary of Probe Calibrations

Probe Type	C_p	R_p Reynolds Number Range
.022 Total Head	1.000	$8.4X10^3$ - $3.6X10^4$
.035 Pitot Static	1.040	$1.3X10^4$ - $5.7X10^4$
.120 Total Head	1.000	$4.6X10^4$ - $1.0X10^5$
.120 with .035 Flat Tip	0.995	$1.3X10^4$ - $5.7X10^4$

Corrections were made for temperature, wall effect and displacement of effective center. An ordinary thermometer was used to measure the temperature of the tunnel water. Temperature corrections for density were then made assuming the manometer fluid to be at the same temperature as the test fluid. Corrections for proximity of the wall were made using the correction curve published by Daily, et. al.; (1959) this curve is compared to that of MacMillan (1957) in Figure 4.8. The correction shown is a positive correction to the measured mean velocity, $\bar{u}$. Correction for the shifting of effective center for round

probes was made by adding 15% of the tube diameter to the actual distance from the wall. This correction is based on the measurements of MacMillan (1957). No correction for effective center was made for the flattened probe since comparison with round pitot tube data indicated that none was necessary.

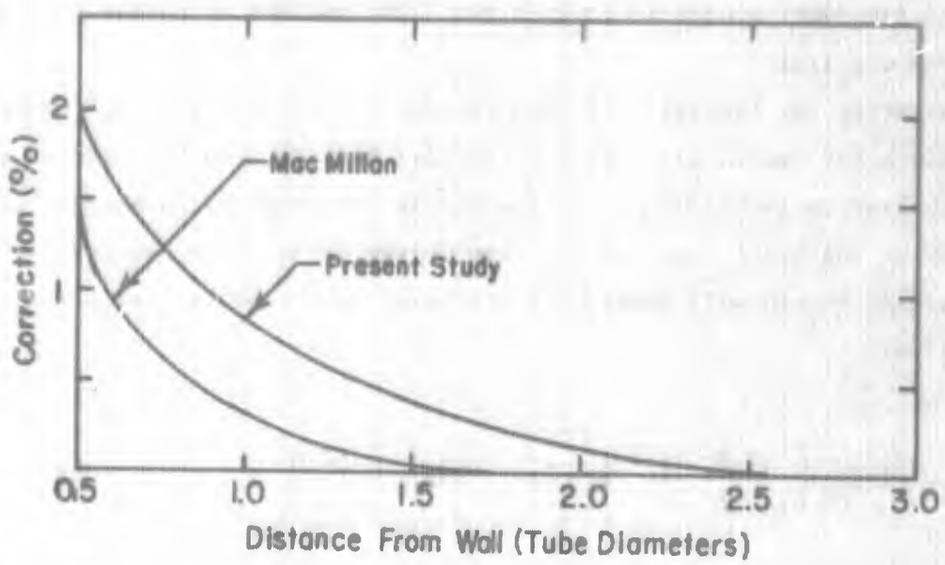

Figure 4.8 Wall Correction Curves

In addition, no corrections were made for turbulence in this study. An estimate of the error introduced by this was given by Ippen, et. al., (1955), as

$$\frac{\sqrt{\frac{2}{\rho}\Delta p}}{\bar{u}} = 1 - \frac{1}{2}\,\frac{\overline{u'^2}}{\bar{u}^2} \qquad (4.1)$$

where Δp is the probe reading

$\bar{u}$ is local mean velocity

$\overline{u'^2}$ is the mean square value of the local longitudinal velocity fluctuations.

When the root mean square value of the turbulence is less than 10% of the mean velocity, the correction is less than 1/2%.

Before each run, water was circulated through the tunnel for at least two hours. This allowed the motor to come to operating temperature and also for the water temperature to stabilize. Water temperature was read before and after a run. The flow rate, which was indicated by the pressure drop across the nozzle, was read at frequent intervals during a run. The maximum variation in flow rate during a run was 1/3%.

Shear stress at the wall for each run was indicated either by the Preston tube technique for smooth walls or by a special technique in the case of rough walls. The Preston technique proved inadequate for rough walls because of the sensitivity of the probe location relative to the datum. The calibration used for determining smooth wall shear with the total head tube is that given by Preston (1954):

$$\log_{10}\left(\frac{\tau_o d^2}{4\rho\nu^2}\right) = -1.392 + 0.875 \log_{10}\left(\frac{\Delta p d^2}{4\rho\nu^2}\right) \qquad (4.2)$$

where τ_o is the wall shear

Δp is the difference between the total pressure sensed by the tube and the static pressure

d is the diameter of the tube

ρ is mass density of the fluid

ν is the kinematic viscosity

A flattened tube, used in the preliminary turbulence studies was also calibrated in the tunnel, using the 0.022 inch probe as a standard. The results indicate that the tube has a calibration curve that is the same as that for a round tube except for the constant. A complete discussion of the Preston tube is given in the Appendix.

Shear stress for the rough wall was obtained by plotting the velocity data in the form

$$\frac{\bar{u}}{U} = F(\log y/k) \tag{4.3}$$

where $\bar{u}$ is the local mean velocity
U is the free stream velocity
k is the actual roughness height
y is the distance from the wall

The datum for y was located half way between the bottom and the peak of the roughness. Preliminary analysis of the data indicated that this location of the datum gave the best agreement between shear stress measured from the velocity data and the Karman momentum integral technique. The shear stress is given by the slope of a best fit straight line through the data closest to the wall according to the formula:

$$\sqrt{\frac{C_f}{2}} = \frac{S}{5.6} \tag{4.4}$$

where C_f is skin friction coefficient
S is the slope of the line

This equation, derived in the Appendix, is valid only for fully rough flow. All rough data fitted into this category which was confirmed by the fact that velocity profiles obtained over high and low velocities at a particular station were identical.

All data were reduced using the IBM 360 computer in the MIT Civil Engineering Systems Laboratory. Input to the computer was the velocity head in inches of manometer fluid and the micrometer dial reading in inches. Additional information concerning the kinematic viscosity, manometer fluid used, total head tube diameter, run number etc. was punched on the first two data cards. When necessary, the actual roughness height was part of the input. Actual roughness height was determined by making a casting of the grooves with a rubbery material similar to the casting cement used by dentists. The roughness height was read from the casting using a Kodak contour projector at X10 magnification.

Because of the different method of determining skin friction on the roughened surface, a preliminary reduction of the data in the computer was required. The local velocity in feet per second was determined from the equation

$$\bar{u} = C\sqrt{h} \tag{4.5}$$

where C is a constant determined by the manometer fluid and temperature of flow

h is the manometer reading in inches

The distance from the wall was computed from

$$y = y_{raw} + 0.65d + C.50k$$

where y_{raw} is equal to zero when the probe is resting on the top of the roughness. Local velocity was normalized with respect to maximum velocity and distance was normalized with respect to the roughness height. Skin friction was determined from the slope of the data plotted as $\frac{u}{U}$ versus log y/k. The value of skin friction so obtained served as input for the final data reduction. A typical example is shown in Figure 4.9

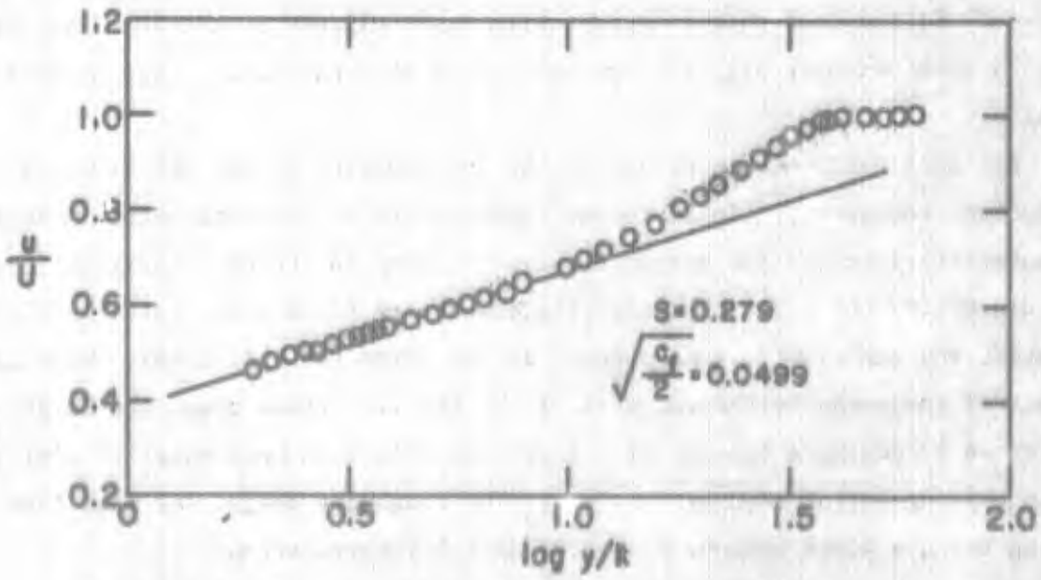

Figure 4.9: Example of Graphical Technique for Determining Rough Wall Shear Stress

In the case of the smooth roof the Preston equation was built into the computer program, and the pressure reading given by the total head tube resting against the roof was converted directly to shear stress.

Final output was given in the form of temporal mean velocity normalized with respect to free stream velocity and shear velocity, velocity defect normalized with respect to shear velocity and wall distance normalized with respect to four characteristic lengths: $\frac{\nu}{u_*}$, roughness height, boundary layer thickness (defined as the distance from the wall to where the local velocity is 99% of the free stream value) and a thickness parameter defined by

$$\Delta = \frac{U}{u_*} \delta_* \qquad (4.6)$$

where U = free stream velocity

$u_* = \sqrt{\frac{\tau_o}{\rho}}$, "shear velocity"

δ_* = displacement thickness

Other output was the boundary layer thickness, shape factor, momentum thickness, displacement thickness and various Reynolds numbers based on momentum thickness, boundary layer thickness and roughness height. The original data were also given as output for checking purposes.

4.5 Measurement of Turbulence Intensity

Longitudinal fluctuations in velocity were measured through the boundary layer adjacent to both smooth and rough surfaces. The turbulence intensity was obtained from the measurement of fluctuating total pressure sensed by a total head tube coupled to a pressure transducer. This instrument package was compatible with the same micrometer traversing device used for the mean velocity measurements. Selection of this type of instrument was based on the desire to use commercially available components and to have a method of measuring turbulence in liquids that is relatively trouble-free. The technique was originally established by Ippen, et. al., (1955) and Perkins and Eagleson (1959). Strasberg (1963) used an improved version for measurements in air.

The instrument used in this study is shown in Figure 4.10. It consists of a total head tube, 0.120 inch in diameter, coupled to a Consolidated Electrodynamics

Corporation 4-313-0001 pressure transducer. This transducer is of the flush mounted, variable resistance type. Application of pressure results in the deflection of a diaphragm which is sensed by unbonded strain gage windings connected in a four-arm bridge. Because of the flush mount, an adapter is required to connect the total head tube to the transducer. The transducer is coupled to a Sanborn Model 296, a basic thermal recorder. A plug-in carrier preamplifier, Model 350-1100B was used to excite the transducer and amplify the output signal. The transducer signal is fed both to the writing pen of the Sanborn and to an output jack.

A Ballantine Model 300 root mean square voltmeter is connected to the output jack for the determination of the root mean square value of the output signal. The output is also fed to a frequency analyzer for the determination of the spectral distribution of energy in the signal. A Technical Products Company Model 625 is used for this purpose. Included in the system is a TP 627 constant bandwidth analyzer, a Type 626 variable frequency oscillator, a Type 645 multiplier, and a Moseley Model 135 Recorder. A 2-cycle bandwidth filter was selected for use in this system. Moody gives a complete discussion of the theory and practice of this equipment in several Technical Products Company publications.

Static calibration of the transducer was achieved with the assembled instrument mounted in place in the tunnel test section. The static pressure level was varied with a pressure regulator described previously. The electrical output from the transducer was displayed as a trace on the Sanborn recorder. Static pressure was read on a manometer. The calibration was then obtained as mm of mercury versus mm of deflection of the Sanborn recorder. This curve is shown in Figure 4.11. At the same time, the signal voltage corresponding to a millimeter of paper was determined. This was necessary for converting root mean square values in millivolts to mm of mercury.

Two total head tubes were used in this study having the same external dimensions and differing only by the fact that the tip of one tube was flattened to 0.035 inches to allow for measurements closer to the wall. This particular tube was discarded in later work because the measured mean velocity profile did not agree with that obtained with the 0.022 inch round total head tube. However, the tube has been calibrated as a Preston tube and the calibration is presented in the Appendix.

An additional feature of this instrumentation is the method of obtaining a relatively flat response curve. One of the major draw-backs to this instrument is the relatively low frequency response. A resonance peak occurs at the natural frequency which distorts the output signal. Generally speaking, the root mean square value of the indicated turbulence intensity is higher than reality because of resonance. One way of coping with the problem is the method used by Daily and Hardison (1954). The spectral distribution of energy is obtained and plotted as energy per cycle per sec versus frequency. Instrument resonance is indicated by a peak in the spectrum at the resonant frequency. The area under this peak relative to the total area under the spectrum is the amount of distortion in the signal. In practice this correction can amount to more than 50% of the signal, resulting in large errors in the corrected reading. An instrument with a relatively flat response over a useful frequency range is the ideal solution. In this study a flat response curve was achieved by damping the probe by the insertion of horsehair in the total head tube. Theoretically the optimum amount of damping would be 70.7% of critical and the response of the instrument would be given by

$$\left|\frac{p}{p_o}\right| = \frac{1}{\sqrt{1+\left(\frac{f}{f_o}\right)^4}} \qquad (4.7)$$

where p is the pressure at the diaphragm

p_o is the external pressure

f is the fluctuation frequency

f_o is the natural frequency

The natural frequency and the amount of damping were determined by balloon tests. The assembled instrument was carefully filled with deaerated water containing a small quantity of Kodak Photo-Flow solution and the tip of the total head tube was inserted into a rubber stopper which was fitted into the neck of an ordinary toy balloon. The balloon was inflated with air and punctured. The electrical signal resulting from this step decrease in pressure was displayed as a trace on the screen of an oscilloscope. The trace was photographed by a Polaroid

camera with an adapter for use on an oscilloscope.

The instrument was tested initially without damping to obtain the value of the natural frequency f_o. Increasing amounts of horsehair were then inserted into the tube until the oscilloscope trace indicated the damping to be correct. Figure 4.12 illustrates typical traces obtained before and after damping. Both the round and flat tip probes were calibrated in this manner. The values of natural frequency obtained were always considerably higher for the flat tip probe than for the round tip. This is believed to be a function of the air-water interface at the tube tip, the flattened tube having an end condition closer to ideal. Results from these tests compare favorably with the theory, given by

$$f_o = 1.09\, f_d^{3/2} \frac{\sqrt{\frac{\rho_d}{\rho}\frac{A_1}{L_1}}}{\left(\frac{E_y}{\rho}\right)^{1/4}} \tag{4.8}$$

where f_d is the natural frequency in air of the transducer in cps

ρ_d is the mass density of the diaphram material

ρ is the mass density of the test fluid (water in this case)

A_1/L_1 is ratio of cross sectional area to length of the total head tube

E_y is Young's modulus for the transducer diaphragm

A derivation of this equation is given in the Appendix.

Quite a bit of developement work was required to obtain the present value of 325 cps for the natural frequency of the instrument. The trouble lay with the overly optimistic values of transducer natural frequency quoted by the manufacturer. Three units were used having transducers rated at 0-10 psi unidirectional, 0-15 psi unidirectional, and 0-15 psi bi-directional. The overall natural frequency of the first unit was 15 cps. The second unit had a value of 150 cps and the final unit rang out at 325 cps. With appropriate damping, this meant that unit #3 had a relatively flat response to 250 cps as shown in Figure 4.13.

Some of the initial developmental work was made using measurements in an open channel flume. This environment was selected because the bulk of the turbulent energy lay below 80 cps. A comparison between the energy density spectrum

Figure 4.10: Turbulence Probe

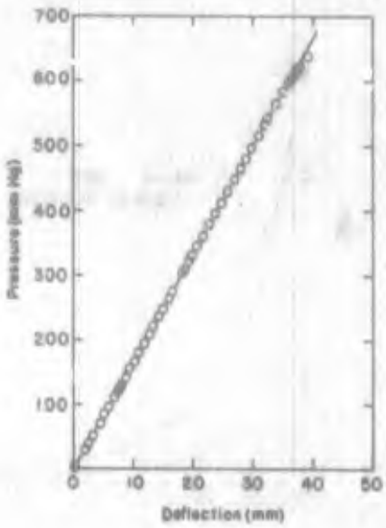

Figure 4.11: Static Calibration Curve for Transducer

Figure 4.12: Response of Turbulence Probe to a Step Function
One Box = 0.005 Sec.

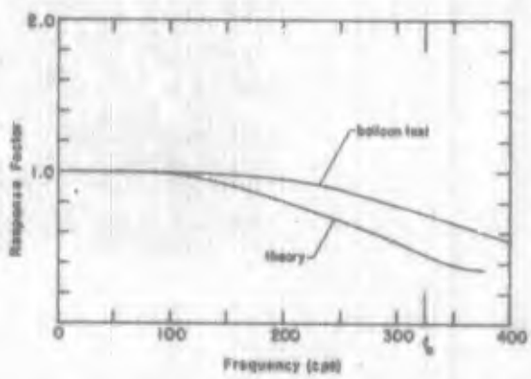

Figure 4.13: Computed Response Curves

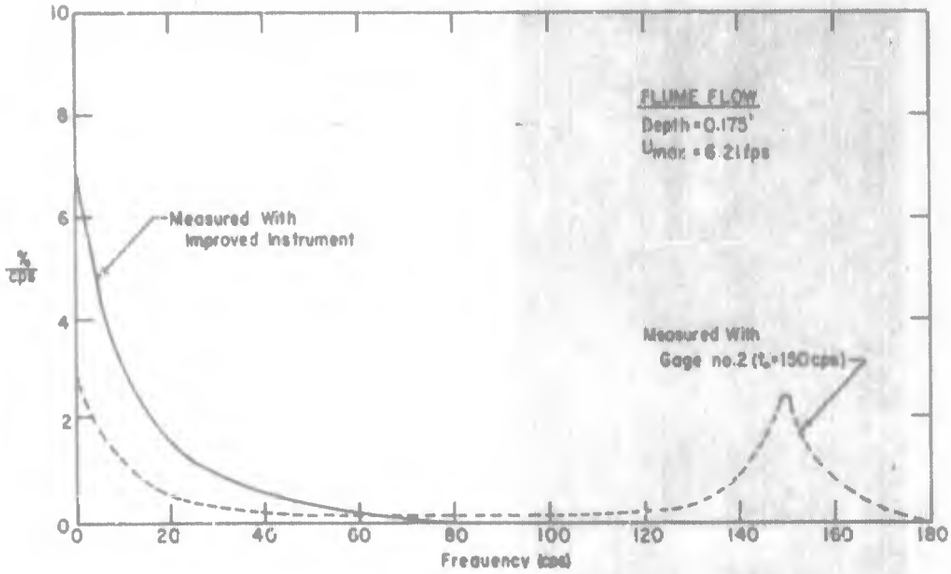

Figure 4.14: Typical Energy Density Spectra Measured with Turbulence Probe Damped and Undamped

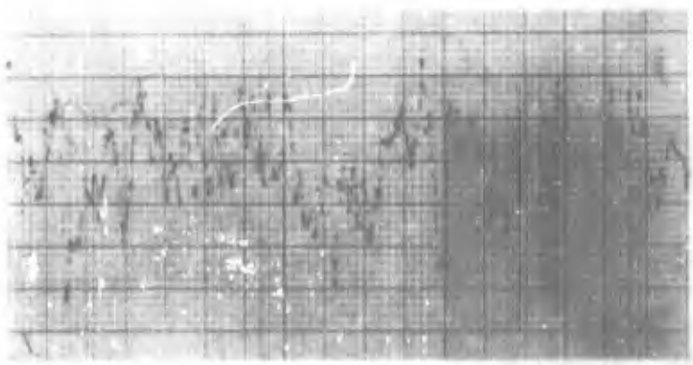

Figure 4.15: Typical Turbulence Signal (Probe #3)

measured by unit #2 in the undamped condition and the spectrum measured by the improved version is given in Figure 4.14. Note that the natural frequency of the undamped instrument is clearly indicated by a resonance peak.

After final developmental work was completed, the unit was tested in the water tunnel. Initial tests were run to determine the vibration characteristics of the unit mounted in the test section. The root mean square and spectral density of the output was determined for the unit filled with water and mounted in the traversing device, but not connected to the total head tube. The signal was compared with the output of a phonograph needle mounted on the test section. Resonant peaks were observed in the output from both the transducer and the phonograph needle. The resonant frequency for the transducer was either identical to the value or equal to one half the value of the resonant frequency in the signal from the phonograph needle. This resonance frequency varied with pump speed. In all cases the root mean square of the output due to vibration was less than 1% of the free stream turbulence signal. Based on this result, no corrections were made for vibration in the turbulence data.

The actual collection and reduction of data was similar to the procedure used for the mean velocity data. The same precautions were followed to insure steady state operation of the tunnel with regards to flow rate and temperature. The same corrections for wall effect and shear displacement effect described previously were also applied to the turbulence data. Before each run an energy density spectrum of the signal from the probe was obtained. Inspection of this plot was made to determine if there were any problems with resonance or overdamping. At each position of the probe in the boundary layer the mean value of the probe signal was recorded as a trace on the Sanborn. This was obtained using the averaging circuit in the instrument. The root mean square value of the signal was read on the rms voltmeter. Since the probe sensed total head, it was also necessary to record the static pressure at the station in question for each data point. Variations in static pressure with time during a run rarely exceeded 1 mm of mercury. The probe position relative to the wall was read on the micrometer dial of the traversing device.

Data reduction was carried out on the computer using a program similar to that used for mean velocity traverses. The basic input consisted of the mean

value of total head in mm of deflection, root mean square values in millivolts, static pressure in mm of mercury and the micrometer dial reading in inches. The static transducer calibration, roughness height, skin friction coefficient, viscosity, probe diameter, run number, etc. were punched on the first three cards.

Mean velocity was computed from the square root of the difference between total pressure and static pressure. The root mean square of the electrical signal was converted to an equivalent pressure head. The value of the turbulence intensity was then determined from the relation:

$$\frac{\sqrt{u'^2}}{U} = C\frac{\phi}{U} \qquad (4.9)$$

where C is a calibration constant

ϕ is the rms of the transducer signal in millivolts

U is the temporal mean local velocity in feet per second

Both turbulence intensity and mean velocity parameters were computed for all runs. An estimate of the errors associated with this technique is given in the Appendix.

4.6 Cavitation Inception Determination

Fundamental to this investigation is the determination of the incipient cavitation index under various conditions. This particular parameter is rather difficult to define and without certain "ground rules" there can be a large discrepancy in the data obtained by two different investigators. The technique used was to determine the so-called dessinent cavitation index cited by Holl (1959). This is the value of the cavitation index obtained when cavitation is removed by raising the static pressure and is generally higher than the value obtained for inception by gradually lowering the pressure until cavitation occurs. This discrepancy between incipient and dessinent cavitation is generally referred to as cavitation hysteresis.

Before the actual determination of cavitation inception certain calibration runs were performed. First the pressure gradient along the test section was determined over the range of flow rate used in this investigaiton. The pressure gradient is independent of velocity for the rough roofs, but varies with velocity for the smooth roof. However, the smooth roof pressure gradient was unsuitable for cavitation

inception work anyway. Cavitation inception would always occur on the entrance lip of the test section bottom with the smooth roof installed. The results of the calibration are presented in Figure 4.16. The data is presented as a pressure difference normalized with respect to the velocity head at the nozzle, the reference pressure being the value at x = 5 inches. Also determined was the free stream dynamic pressure for various flow rates indicated by the pressure drop across the nozzle. Figure 4.17 is the calibration curve for the 0.0125 inch roughness. The pressure gradient for this case is essentially flat and hence the local free stream dynamic pressure is the same at each measuring station as shown.

Cavitation itself was detected visually. However some experiments were run using the output from a phonograph needle resting on the test section. Components of the signal due to vibration were filtered out and the filtered signal was displayed on an oscilloscope screen. When cavitation occurred there was a marked increase in the output both in intensity and frequency. The technique worked beautifully for detecting inception on a small disk inserted in the flow. However, because of the much lower pressures required to get boundary layer cavitation, the pump would start to cavitate in many instances before cavitation was observed in the test section. This pump cavitation would create noise in the same frequency range as the test section cavitation, hence masking the electronic signal. The technique was discarded after these preliminary experiments produced negative results.

Preliminary to every cavitation run, the gas content of the tunnel water was reduced to approximately 0.3% by volume. This was accomplished by slowly circulating the water through the tunnel while applying a vacuum of approximately 28 inches of mercury at the stilling section. The local static pressure in the test section was very low, hence creating cavitation which extended into the diffuser. Approximately 3 to 4 hours were required for the deaeration process.

During the cavitation runs, all piezometer taps except at Station 2, x = 5 inches, were blocked off with special brass plugs. The tunnel was allowed to come to steady state and the water temperature and gas content were recorded before and after each run. For each data point the pressure drop across the tunnel was read and then the static pressure was lowered until cavitation occurred. The location of the inception point was noted and the pressure was raised until cavitation disappeared. The value of static pressure at Station 2 was read on an absolute manometer

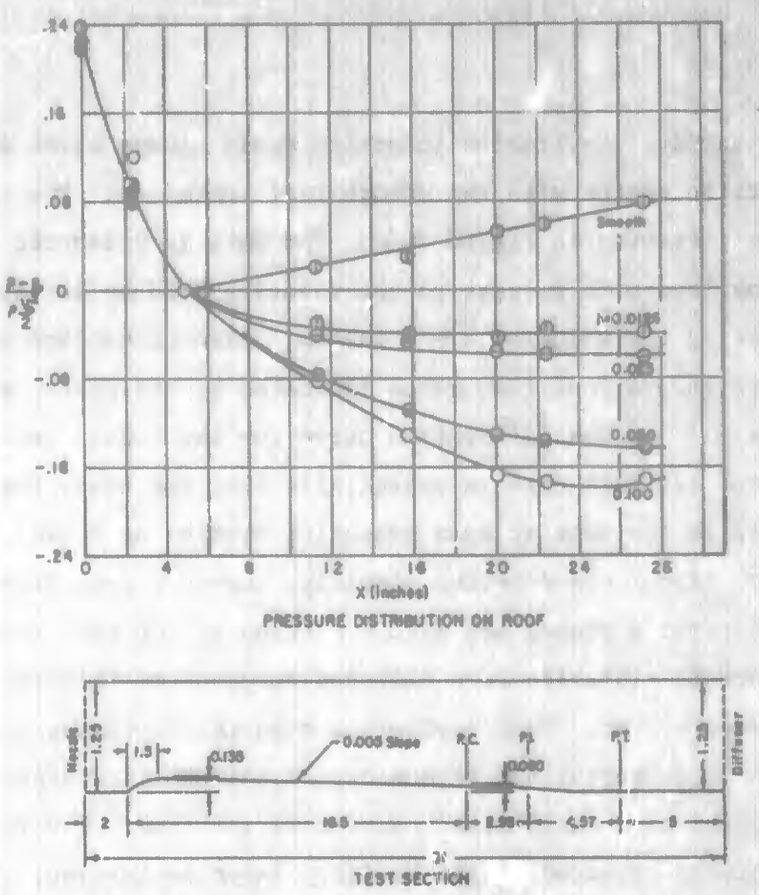

Figure 4.16: Tunnel Pressure Gradient

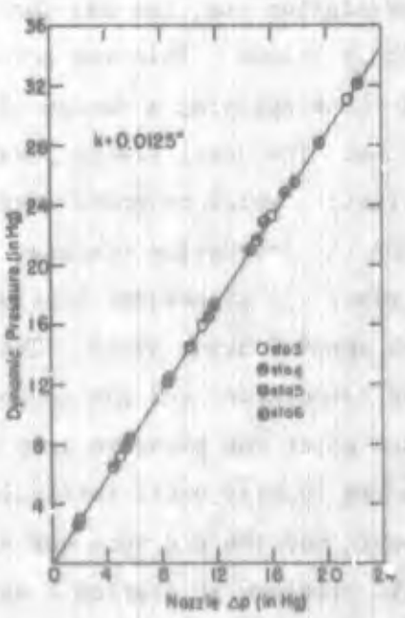

Figure 4.17: Typical Calibration Curve for Free Stream Dynamic Pressure

which gives a direct reading in mm of mercury. Static pressure was raised and lowered six times for each data point and a statistical view point was used in defining the absence of cavitation. It was defined as the absence of bubbles and sound for a period of two seconds. Bubbles were noted in the grooves on the roof which persisted to very high values of static pressure. The presence of these bubbles was discarded in the determination of incipient cavitation.

The data were reduced to an incipient cavitation index based on local wall pressure and free stream dynamic head. The local wall pressure was computed from the wall pressure at Station 2, the measured flow rate, and the previously determined pressure gradient for non-cavitating flow. The free stream dynamic pressure was obtained from the calibration curve for the station in question. In all cases, cavitation was observed downstream from Station 2. This insured a fairly reliable value for the static pressure. It is believed that the errors inherent in converting the wall pressure values at Station 2 to the local value at the point of incipient cavitation are lower than a direct measurement in a cavitating flow. This technique eliminated the problems of the piezometer tap influencing the cavitation inception by the introduction of nuclei and the problems inherent with gas in the lines leading from the taps to the manometer.

4.7 Determination and Control of Gas Content

An investigation of cavitation in a zone of established parallel flow requires that pressures near the vapor pressure exist throughout the main stream of the parallel flow. The zone of minimum pressure is not restricted to a limited area as for example the curvilinear flow about an immersed body. To maintain truly dissolved gas in the test section very low values of gas content would be required to prevent gas coming out of solution upstream of the cavitation inception point. To standardize the influence of dissolved and undissolved gas content, the gas content was kept at a low value and carefully controlled.

For measurement of gas content, a foil-shaped element was permanently inserted along the centerline of the downstream end of the transition between the test section and the diffuser. A hole in the tip of the foil permits a continuous flow of water past a modified Van Slyke apparatus. A known quantity of water can be drawn into this instrument and by repeatedly forcing the water through a restriction into an

evacuated volume the dissolved and undissolved air is removed from the sample. The gas and vapor are compressed into a known volume and its pressure is indicated on a manometer scale. At the same time the temperature of the water is noted. The percent gas content by volume is given by the formula

$$V^* = \frac{3.592 \times P_g}{(273 + T)} \qquad (4.10)$$

where

V^* is the percent gas content at standard temperature and pressure

P_g is the gas pressure, mm mercury

T is the temperature in ^{o}C.

McNulty (1962) gives a detailed explanation of the technique in using this instrument. A view of the apparatus used in this study is shown in Figure 4.18.

4.8 High Speed Photographic Techniques

The actual inception process was inspected with the use of high speed motion pictures. The technique is similar to that used by Daily and Johnson (1955). Silhouette photography, using an electronic flash as a light source, was the method used in this investigation.

The camera employed was a General Radio Oscillograph Recorder, Type 651-AH equipped with either a 90 mm f/1.8 or 50 mm f/1.4 lens. The camera speed is controlled by regulating the supply voltage with a Variac transformer. At the maximum supply voltage of 220 volts the camera reaches a film speed of 1,000 inches per second. The number of pictures taken per second is determined by the frame size and the camera speed. The frame size for this study was 1/4 inch. Allowing some spacing between frames, the distance travelled between frames is 1/3 inch. With a film speed of 1,000 inches per second this corresponds to a frequency of 1,000 ÷ 1/3 = 3,000 frames per second.

An Edgerton, Germeshausen and Grier Type 501 Stroboscope provided light flashes of approximately one microsecond (Figure 4.20). Three intensities of light are available over a frequency range of 60 to 6,000 cps. The 3,000 cps frequency selected for this study was controlled by a calibrated audio oscillator. Since a short time is required to accelerate the camera to the desired speed, a leader consisting of 40 feet of exposed film would be spliced to approximately 30 feet of unexposed

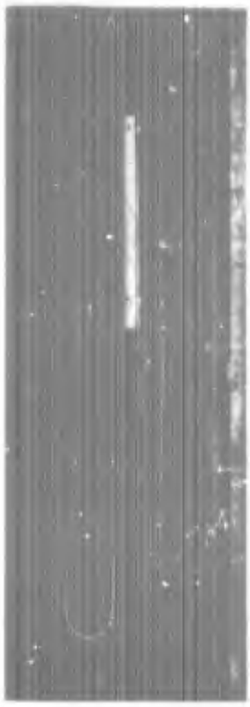

Figure 4.18: Gas Content Apparatus

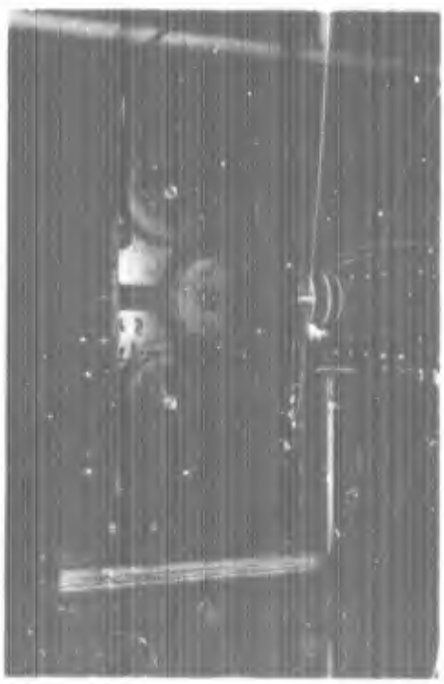

Figure 4.19: High Speed Camera

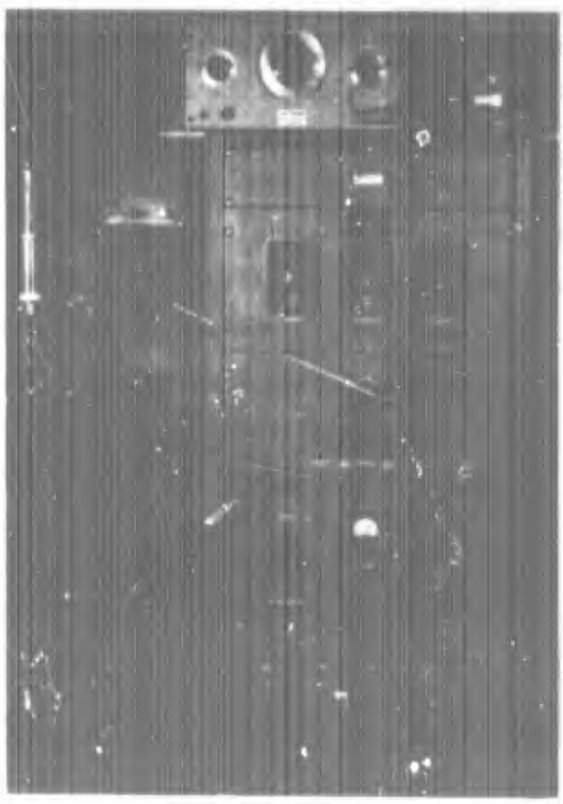

Figure 4.20: Stroboscope

film. A time delay of 0.7 seconds was set on the Stroboscope to allow this leader to pass by the lens before flashing the light source. Running time was an additional 0.8 seconds.

The light source, consisting of a standard quartz flash tube, was placed on one side of the test section and the camera was focused through the opposite wall. Magnification varied from 1/2 to 3. The variation in magnification was accomplished by changing the lens to film plane distance with specially constructed lens tubes.

To provide a reference to the roof in the photographs a threaded rod was inserted through one of the holes in the floor of the test section at the station of interest. The tip of the rod was allowed to rest on the roof. By photographing the rod, a frame of reference was given by the tip and the actual magnification was known from the measured distance between threads in the photograph. There were 40 threads per inch on the rod, so that at a magnification of 2, for example, there would be 20 threads per inch in the photograph.

The procedure followed in each run was to allow the water to circulate through the tunnel for 2 hours. The desired wall pressure was adjusted after noting the flow rate. Temperature and gas content were recorded at the same time. The camera was started by a button on the stroboscope, the proper delay time and shutting off of the camera was done by automatic timers in the unit.

Data obtained from the film record were projected on a large piece of graph paper with a film strip projector. The actual distance in a projected photograph was obtained by projecting the previously obtained photograph of the threaded rod on the graph paper. The data obtained for each frame were the bubble diameter and its horizontal and vertical coordinates. Bubbles which were out of focus were not included in the observations. Since the bubbles had shapes which were quite often anything but spherical, the diameter was defined as the square root of the product of the major and minor diameters.

Because of the narrow depth of field (0.03" at a magnification of 3), quite often bubbles would move in and out of focus. A misleading value for size would be obtained from out-of-focus bubbles. Thus it was necessary to consider only sharply defined bubbles.

Bubble distributions were obtained by counting bubbles in horizontal sections of the photographs. The photographs were selected at random to insure a good statistical sampling. The data for the critical radius were obtained by examining

approximately 1,000 frames to find the smallest bubble which would expand while passing through the field of view of the camera. Growth data were obtained from the plotting of bubble size from frame to frame, the time between frames being known.

V. PRESENTATION AND DISCUSSION OF RESULTS

5.1 Scope of Test Program

Table 5.1 is a summary of the experimental work performed during this investigation referred to by run numbers. Not included in the table are the various runs to determine tunnel pressure gradient and to calibrate transducers and velocity probes. The pertinent data are tabulated in the Appendix. Four types of runs were made; mean velocity profiles, turbulence, cavitation inception and photographic investigation of cavitating flow.

5.2 Mean Velocity Data

5.2.1 Law of the Wall

Figure 5.1 is a summary of the smooth wall velocity data plotted in the form

$$\frac{\bar{u}}{u_*} = \psi\left(\frac{u_* y}{\nu}\right) \tag{5.1}$$

where $\bar{u}$ is the temporal mean velocity

u_* is the shear velocity, $\sqrt{\tau_o/\rho}$

y is the distance from the wall

ν is the kinematic viscosity

Near the wall, for the small values of $(u_* y/\nu)$, the data are represented by a straight line given by the equation:

$$\frac{\bar{u}}{u_*} = 5.6 \log \frac{u_* y}{\nu} + 5.1 \tag{5.2}$$

This equation is as suggested by Clauser (1956) except for the constant, which Clauser gives as 4.9. Also shown is a power law equation given by

$$\frac{\bar{u}}{u_*} = 8.61 \left(\frac{u_* y}{\nu}\right)^{1/7} \tag{5.3}$$

Table 5.1

Summary of Test Program

Type of Surface	Station*	Run Number: Velocity Profiles	Turbulence	Inception	Photography Record
Smooth	2	5,6			
	4	14,15			
	5	21,22	49,50,62-65,76,77		
	6	7-15,23,24			
	Flume	35,36	35,36		
k = .0125"	3	57			
	4	56		C12,C13	P47-P55
	5	55			
	6	52-54	74,75		
k = .025"	2	48			
	3	45			
	4	46		C10,C11	P43-P47
	5	47			P38-P42
	6	43,44	72,73		
k = .050"	3	61			
	4	60			
	5	59		C14	P56-P62
	6	58	70,71		
k = .100 (Protrusions)	3	27,28			
	4	29,30			
	5	31,32			
	6	25,26			P6-P26
k = .100 (Grooves)	3	34			
	5			C5-C9,C15	P27-P37
	6	33	37-41,66-69		P63-P67

*Location for inception varied, approximate station shown.

Equation (5.3), as shown in the Appendix, is equivalent to the calibration equation presented by Preston (1954) for determining wall shear with a pitot tube. It is interesting to note that this equation appears to fit the data in Figure 5.1 better and over a greater portion of the boundary layer. Another point to make is that these measurements have been obtained in a relatively thin boundary layer (the maximum thickness was 0.3 inches). Deviation from the law of the wall is noted at relatively low values of $u_* y/\nu$, of the order 250 to 600. The velocity distribution in thick boundary layers under a zero pressure gradient appears to obey the law of the wall to much larger values of $u_* y/\nu$. For example, Willmarth and Wooldridge (1962) report agreement with the law of the wall up to $u_* y/\nu = 6{,}000$ in a 5-inch-thick boundary layer. This is not an unexpected result if one hypothesizes that the upper limit on agreement is given by some fraction of the boundary layer thickness, for example for $y/\delta = 0.15$. For a flat plate, at relatively low Reynolds numbers, a simple formula for the value of $u_* y/\nu$ at $y/\delta = 0.15$ may be derived using the familiar power law expressions for skin friction and boundary layer growth:

$$\delta = 0.37 \frac{x}{R_x^{1/5}} \tag{5.4}$$

$$\frac{u_*}{U} = \frac{0.172}{R_x^{1/10}} \tag{5.5}$$

$$R_x = \frac{Ux}{\nu} \tag{5.6}$$

where U is maximum velocity (constant for flow over a flat plate)
x is distance from the leading edge
δ is the boundary layer thickness

By making the substitutions:

$$y = 0.15\delta$$

$$u_* = \frac{u_*}{U} U$$

into u_*y/ν, the upper limit of the law of the wall is obtained:

$$\left(\frac{u_*y}{\nu}\right)_{ul} = 0.00953 \left(\frac{Ux}{\nu}\right)^{0.7} \tag{5.7}$$

A further remark on Figure 5.1 should be made. Originally the smooth wall velocity profiles were normalized using the Squire-Young equation

$$\frac{U}{u_*} = 5.89 \log \frac{U\theta}{\nu} + 3.56 \tag{5.8}$$

where θ is the momentum thickness. When the data were plotted they fell below the accepted law of the wall and no consistency between runs could be found. The first hypothesis was that the roof was not smooth. However, assuming this to be true, the set of velocity profiles obtained was still not compatible. Finally, the Preston tube technique was used to determine skin friction which resulted in the consistent data shown in Figure 5.1. The reason for the differences is explained by the fact that the Squire-Young formula is based on flat plate experiments. The pressure gradients encountered in the present smooth wall studies ranged from nearly zero, where good agreement was found between the Preston tube and the Squire-Young formula, to mildly adverse where deviations as high as 9.4% were noted. The Squire-Young formula always predicted higher values, which is in agreement with the fact that the measurements were made in an adverse pressure gradient.

Several rough wall velocity profiles are shown in Figure 5.2. Depending on the value of u_*k/ν , where k is the mechanical roughness height, each curve

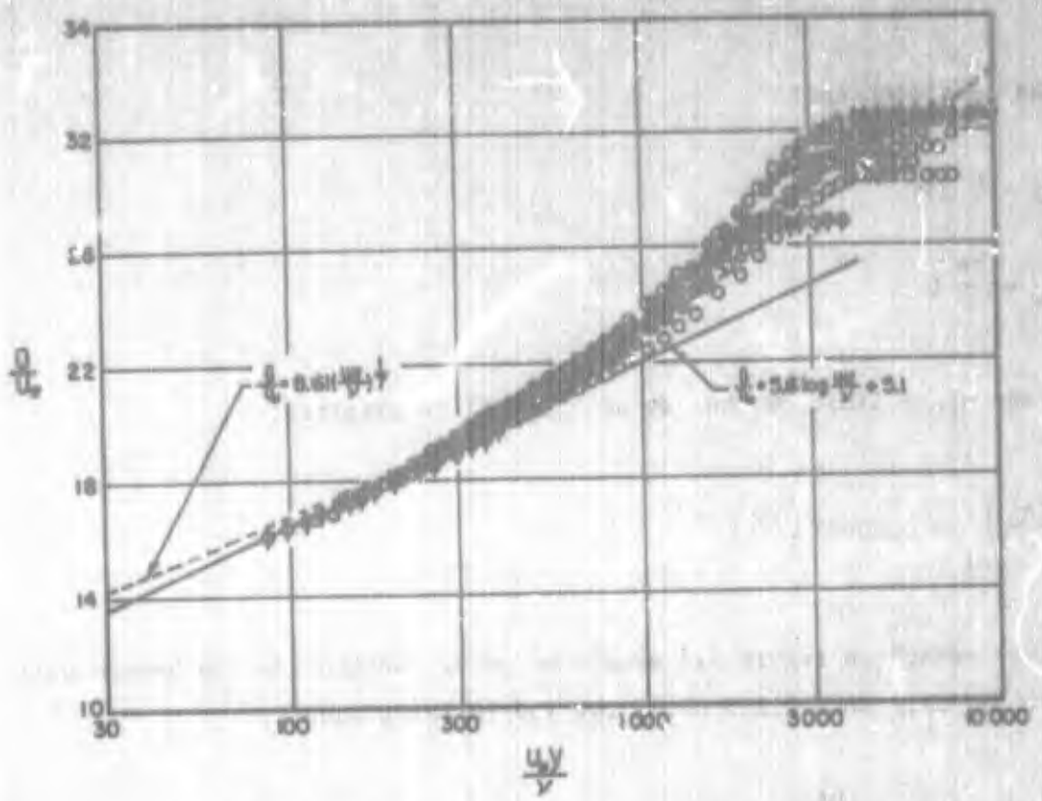

Figure 5.1: Law of the Wall for Smooth Boundaries

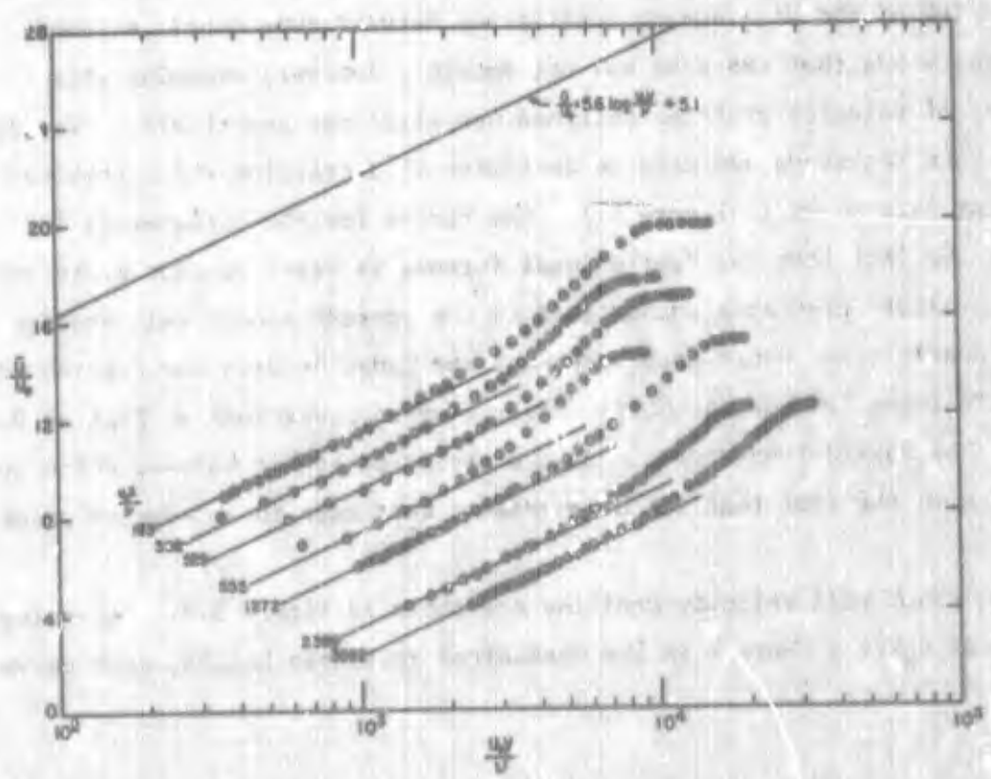

Figure 5.2: Law of the Wall for Rough Boundaries

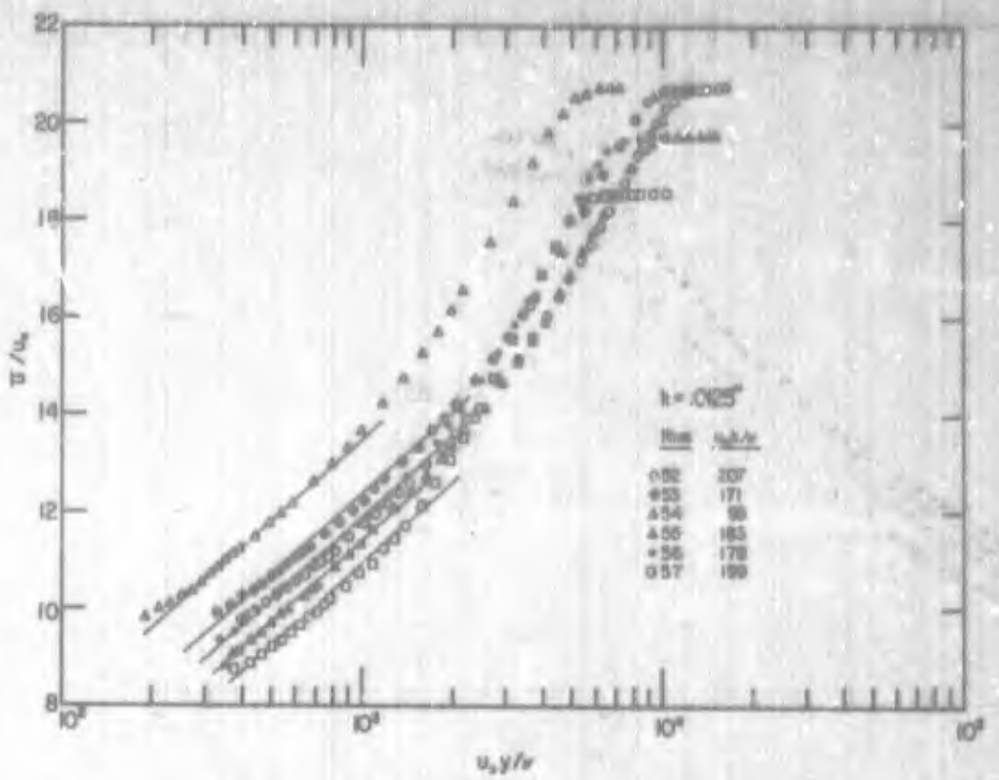

Figure 5.3: Velocity Data, k = 0.0125"

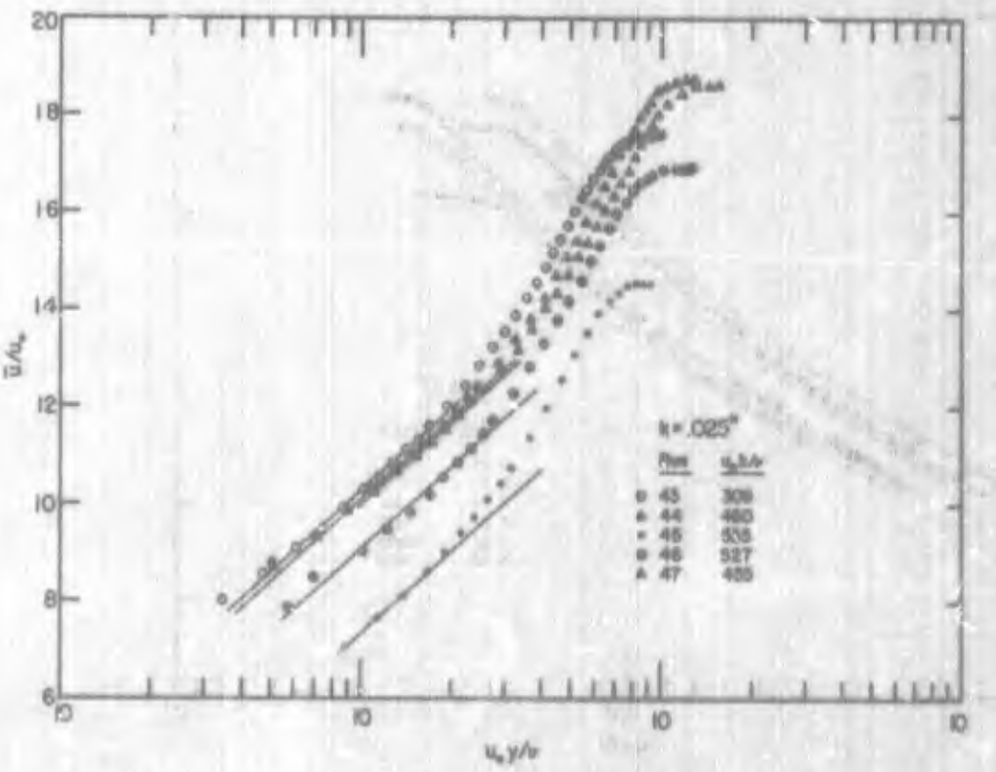

Figure 5.4: Velocity Data, k = 0.025"

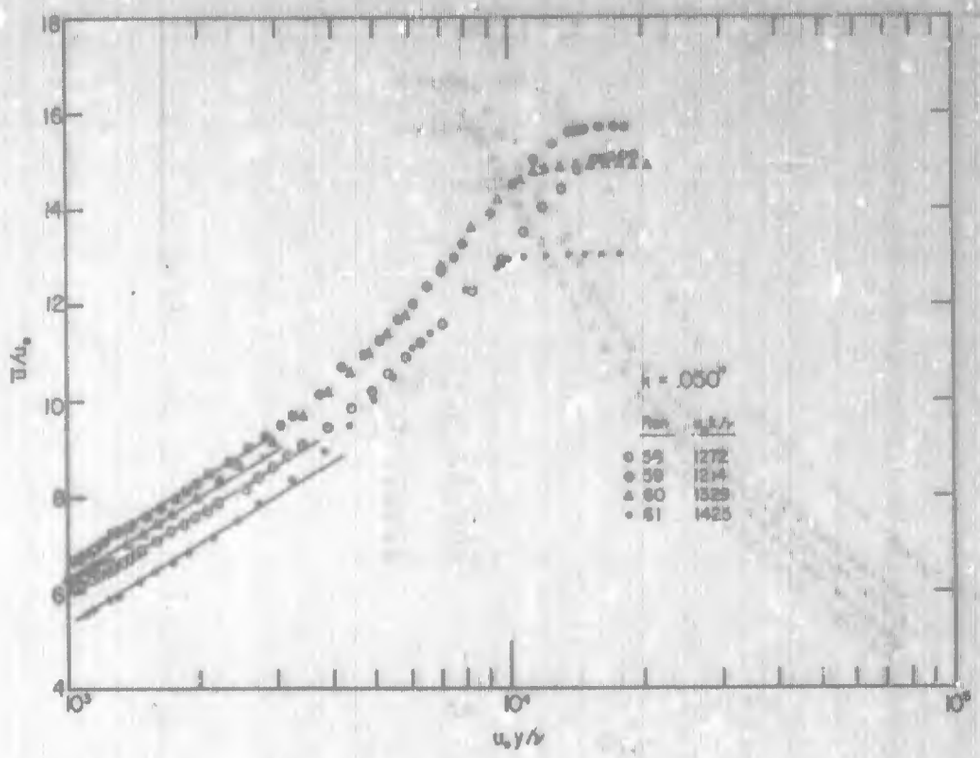

Figure 5.5: Velocity Data, k = 0.050"

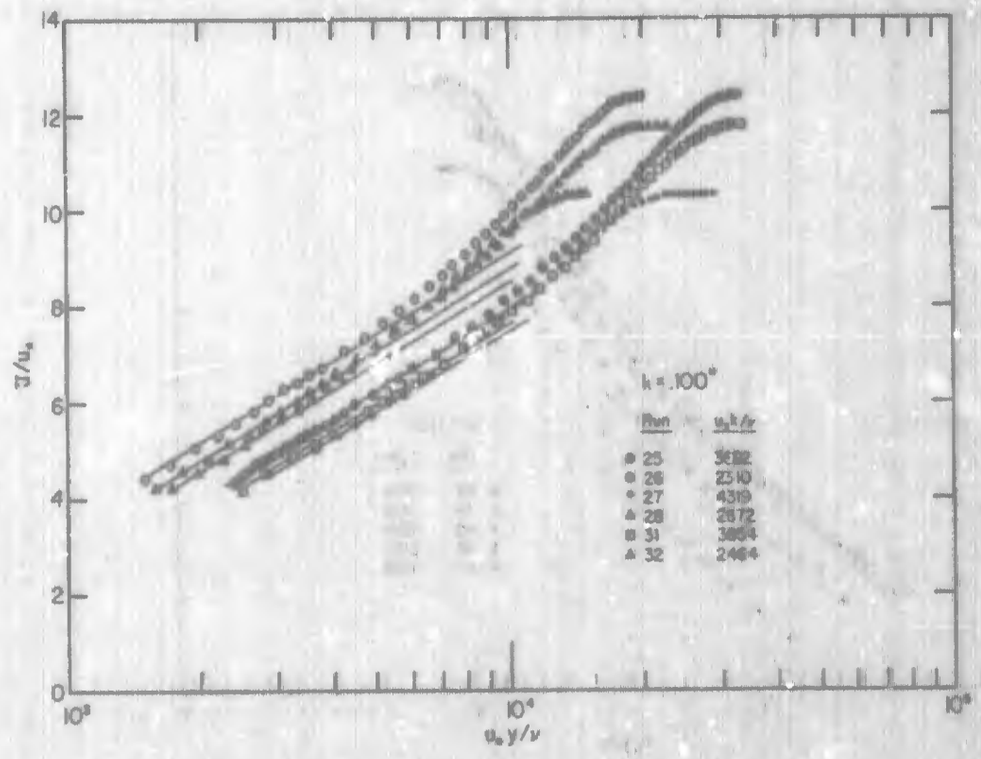

Figure 5.6: Velocity Data, k = 0.100"

falls below the smooth curve by an amount $\Delta\bar{u}_1/u_*$. For relatively low values of u_*y/ν a logarithmic law of the wall exists, given by the relation:

$$\frac{\bar{u}}{u_*} = 5.6 \log \frac{u_* y}{\nu} + 5.1 - \frac{\Delta\bar{u}_1}{u_*} \tag{5.9}$$

Only selected profiles from each surface studied in this investigation are shown in Figure 5.2; however, all rough wall velocity data are given in Figures 5.3 - 5.6.

5.2.2 Velocity Defect Law

In Figure 5.7 the velocity defect law for data obtained under zero or close to zero pressure gradient is shown. The length parameter is given by

$$\Delta = \frac{U}{u_*} \delta_* \tag{5.10}$$

where δ_* is the displacement thickness. This parameter is more easily defined than the boundary layer thickness, δ. In addition, an analogy exists with the length, ν/u_*, which is known to have significance near the wall where viscosity is important. Clauser (1956) has shown that in the outer 80 to 90% of the boundary layer the eddy viscosity, ε, is given by the relation

$$\varepsilon = C_1 U \delta_* \tag{5.11}$$

where C_1 is a constant of proportionality. Thus, the quantity Δ is given by

$$\Delta = C_1 \frac{\varepsilon}{u_*} \tag{5.12}$$

which is analogous to the viscous length, ν/u_*. The important result to be noted in Figure 5.7 is the excellent agreement between smooth wall and rough wall data and the curve proposed by Hama (1954).

For non-zero gradients, the velocity defect law is no longer universal as shown in Figure 5.8. Close to the wall there is a logarithmic portion which is

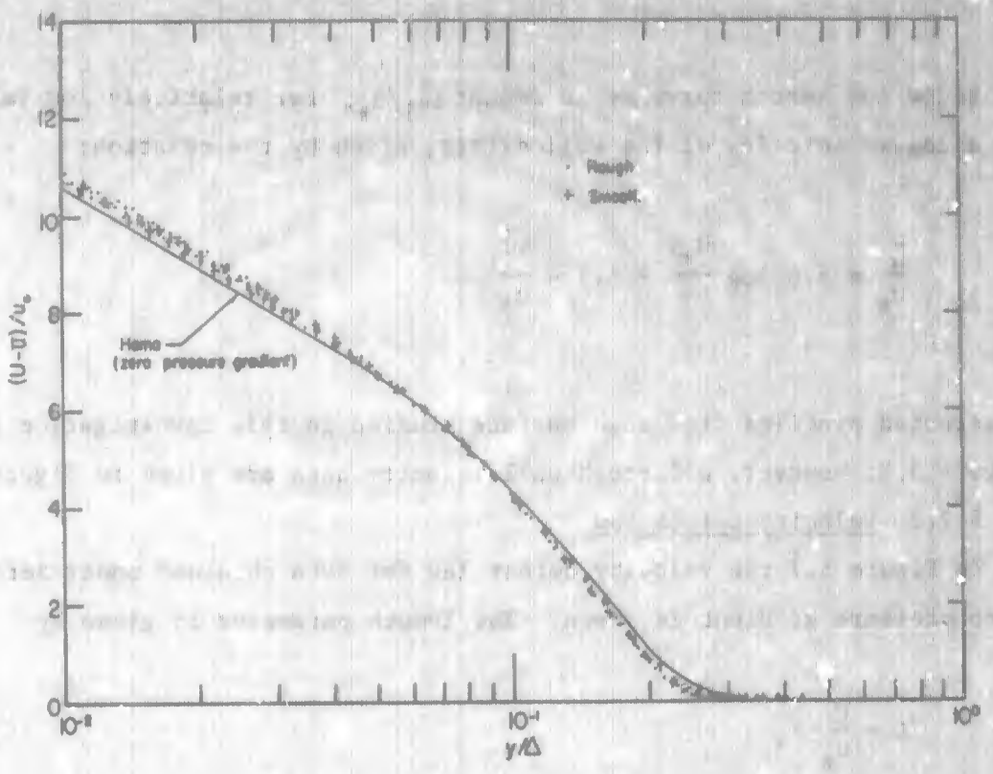

Figure 5.7: Velocity Defect Law, $\frac{dp}{dx} = 0$

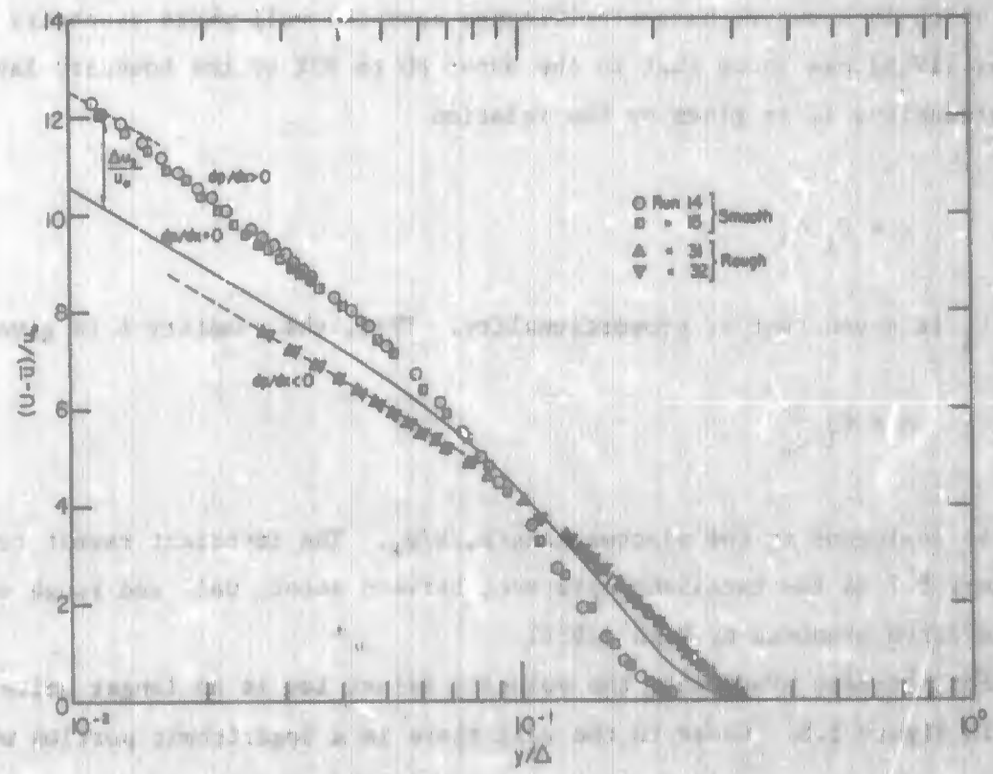

Figure 5.8: Velocity Defect Law, with Pressure Gradient

displaced from the zero gradient law by an amount $\Delta u_2/u_*$. The amount and direction of this displacement is a function of the pressure gradient. As is shown in the next section, the deviation is greater for adverse gradients than for favorable pressure gradients. Of importance here is the logarithmic portion of the profile near the wall which may be written in the form

$$\frac{\bar{u} - U}{u_*} = 5.6 \log \frac{u_* y}{U\delta_*} + 0.6 - \frac{\Delta\bar{u}_2}{u_*} \tag{5.13}$$

Unfortunately, the functional relationship

$$\frac{\Delta\bar{u}_2}{u_*} = \psi\left(\frac{dp}{dx}\right) \tag{5.14}$$

is not known and is probably ill-defined since the previous development of the boundary layer would have to be known also in the general case. The only correlation that appears possible at the moment is

$$\frac{\Delta\bar{u}_2}{u_*} = \psi\left[\frac{U}{u_*}\left(\frac{H-1}{H}\right)\right] \tag{5.15}$$

where H is the ratio of displacement thickness, δ_*, to momentum thickness, θ. This correlation is shown in Figure 5.13 for smooth and rough data. Data for the three profiles examined by Clauser are also shown in the figure. The agreement is good, indicating that the profiles studied in this investigation are similar to the equilibrium profiles of Clauser.

5.2.3 Wall Shear Determination

Figures 5.9 through 5.11 summarize the results obtained for the variation of skin friction along the roughened surfaces used in this study. The variation of $\Delta u_1/u_*$ as a function of $u_* k/\nu$ is plotted in Figure 5.9. A large amount of scatter is evident, which appears to be due to errors in probe location relative to the datum. A small error when normalized with respect to ν/u_* can sometimes

be significant, especially for the smaller roughness heights. For example, after the roof roughened with 0.0125" grooves was fabricated, it was sent out for inspection. The inspection report indicated the true roughness height to be 0.010" at Stations 3, 4, and 5; whereas Station 6 was reported to have a roughness height of 0.014". Using the value 0.014", the data for Station 6 fell well below the sand grain roughness curve in Figure 5.9. When the value 0.010" was used, the results agreed with the values obtained at other positions along the roughened surface. Based on this result, a careful determination was made of the number of grooves per inch at this location and was found to be exactly 40 per inch, which corresponds to the specified k of 0.0125". In fact, it was found that for each roof the number of grooves per inch was exactly as specified, yet there were variations of a few thousands of an inch in the depth of grooves. This might explain the unexpected trend of the data. Theoretically, the data were expected to follow a logarithmic law of the form

$$\frac{\bar{\Delta u}_1}{u_*} = 5.6 \log \frac{u_* k}{\nu} + C \tag{5.16}$$

This result is obtained from the law of the wall for fully rough flow

$$\frac{\bar{u}}{u_*} = 5.6 \log y/k + B \tag{5.17}$$

wherein B is a constant determined by the type of roughness employed, and from the smooth law of the wall

$$\frac{\bar{u}}{u_*} = 5.6 \log \frac{u_* y}{\nu} + 5.1 \tag{5.18}$$

Subtracting equation (5.17) from (5.18):

$$\frac{\bar{\Delta u}_1}{u_*} = 5.6 \log \frac{u_* k}{\nu} + (5.1 - B) \tag{5.19}$$

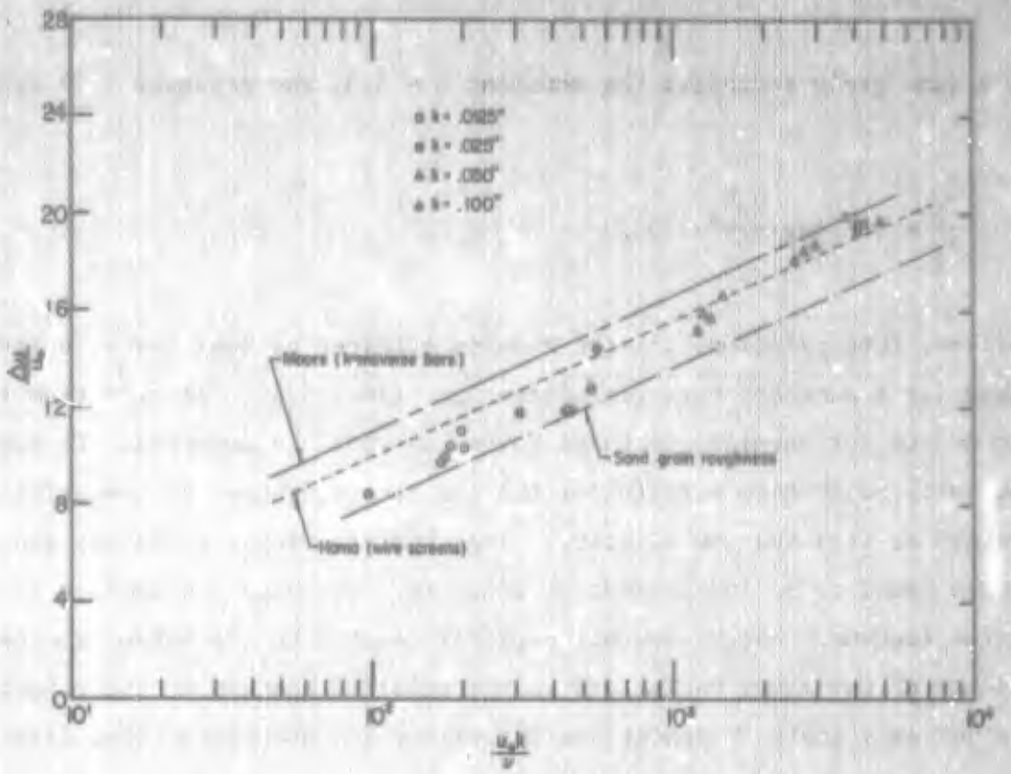

Figure 5.9: Roughness Effect $\Delta\bar{u}_1/u_*$ For Triangular Grooves

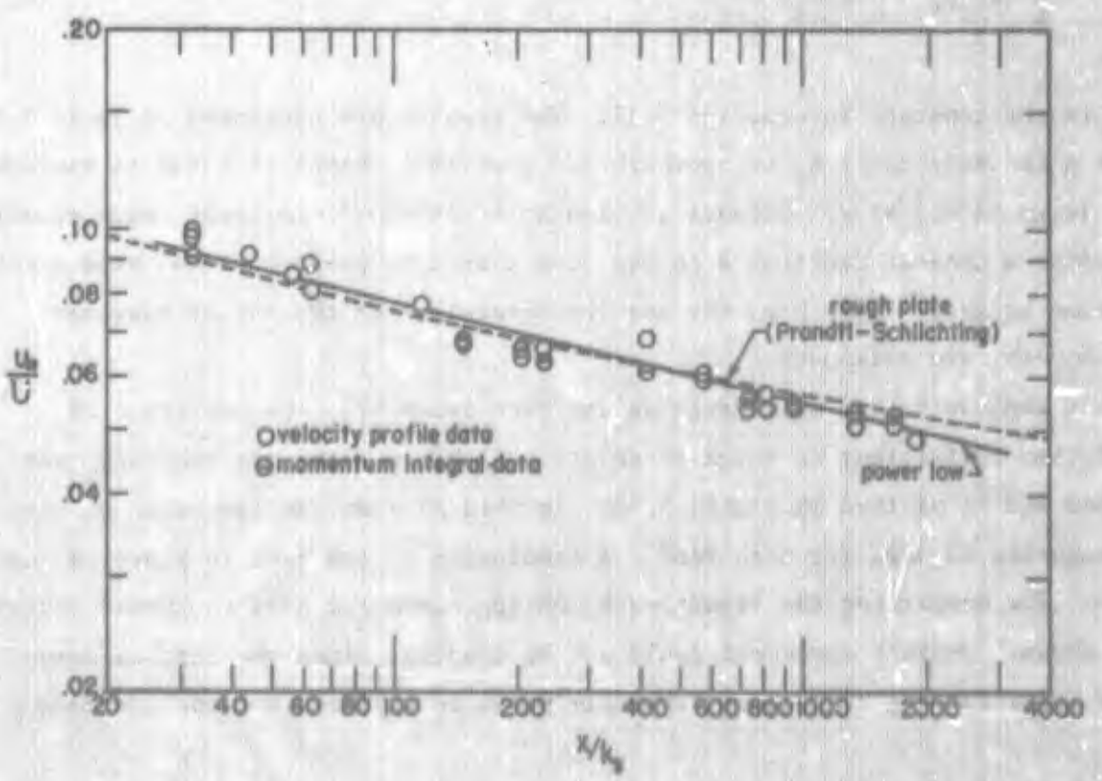

Figure 5.10: Skin Friction Variation

Thus, for a sand grain roughness the constant B = 8.3, and equation 5.19 reduces to

$$\frac{\Delta\bar{u}_1}{u_*} = 5.6 \log \frac{u_* k_s}{\nu} - 3.2 \qquad (5.20)$$

For comparison, this relation, and the results obtained by Hama for wire screen and by Moore for transverse bars are plotted in Figure 5.9. The data from the present study are not parallel to these curves as would be expected. It was determined that fully rough flow existed for the smallest roughness by comparing results obtained at high and low velocity. The skin friction coefficient and velocity profiles were found to be independent of velocity. The only explanation is that the effective roughness height was not directly related to the actual roughness height because of the minor variations in the relative spacing of the roughness. The equivalent sand grain roughness was determined for each data point from the relation

$$\frac{k_s}{k} = \log^{-1}\left(\frac{8.3 - B}{5.6}\right) \qquad (5.21)$$

where B is the constant in equation 5.17. The results are presented in Table 5.2. There is a tendency for k/k_s to approach 1.0 for small values of k and to approach 1/3 for large values of k. Because the roughness is two-dimensional, each element should offer a greater resistance to the flow than a three-dimensional sand grain of the same height. Therefore, the results obtained with the larger roughness heights appear more reasonable.

Using the equivalent sand grain height from Table 5.2, the variation of skin friction coefficient in terms of relative distance along the roof x/k_s was determined and is plotted in Figure 5.10. In this plot an average value of sand grain roughness is used for each roof. A tabulation of the data is given in the Appendix. For comparison the Prandtl-Schlichting curve for sand roughened plates is also shown. Perfect agreement could not be expected since the results were obtained under varying degrees of favorable pressure gradient and the distance x

Table 5.2

Equivalent Sand Grain Roughness

Nominal k (inch)	Station	Run	k_s/θ	k_s (inch)
0.0125	3	57	1.611	0.016
	4	56	1.218	0.012
	5	55	1.090	0.011
	6	52	1.279	0.013
	6	53	1.279	0.013
	6	54	1.279	0.013
0.025	3	45	2.43	0.054
	4	46	1.29	0.031
	5	47	1.01	0.024
	6	43	1.34	0.031
	6	44	1.03	0.024
0.050	3	61	2.41	0.123
	4	60	1.78	0.098
	5	59	1.70	0.088
	6	58	2.06	0.107
0.100 (Protrusions)	3	27	3.20	0.326
	3	28	3.49	0.356
	4	29	4.05	0.446
	4	30	5.53	0.608
	5	31	4.03	0.431
	5	32	3.49	0.373
	6	25	3.30	0.366
	6	26	3.19	0.354
(Grooves)	3	34	3.64	0.379
	6	33	4.33	0.437

is not a definite quantity, being defined in this case as the distance from the nozzle. The roughened portion of the roof starts at x = .". Because of the boundary layer growth, it was felt that the distance from the nozzle would give better agreement than the distance from the beginning of the roughness. However, the data appears to be consistent, although perfect agreement with the flat plate law cannot be expected anyway. Skin friction values obtained from the velocity profile method and the momentum integral method of VonKarman are in good agreement. The momentum integral technique is based on the relation

$$\frac{C_f}{2} = \frac{d\theta}{dx} + \left(\frac{\delta_*}{\theta} + 2\right)\frac{\theta}{U}\frac{dU}{dx} \tag{5.22}$$

where θ is the momentum thickness
δ_* is the displacement thickness
U is the free stream velocity

In the case of the 0.100" roughness, good agreement between the two methods of determining skin friction could only be obtained for the early stages of boundary layer growth. At stations farther downstream, the boundary layer thickness on the roof was very large compared to the height of the test section, possibly merging with the smooth wall boundary layer developed from the bottom. The second term in equation 5.22 is based on the assumption of potential flow. If a potential core flow no longer exists, this term would have to be replaced with a pressure gradient term, as for example in the case of pipe flow. The consistency of the data is best illustrated using the method suggested by Clauser. Figure 5.10 presents the skin friction data plotted in the form

$$\sqrt{\frac{2}{C_f}} = \psi\left(\frac{F_2}{F_1}, \frac{U\delta_*}{\nu}\right) \tag{5.23}$$

where $$F_2 = \log^{-1}\left(\frac{\Delta u_2}{5.6u_*}\right) \tag{5.24}$$

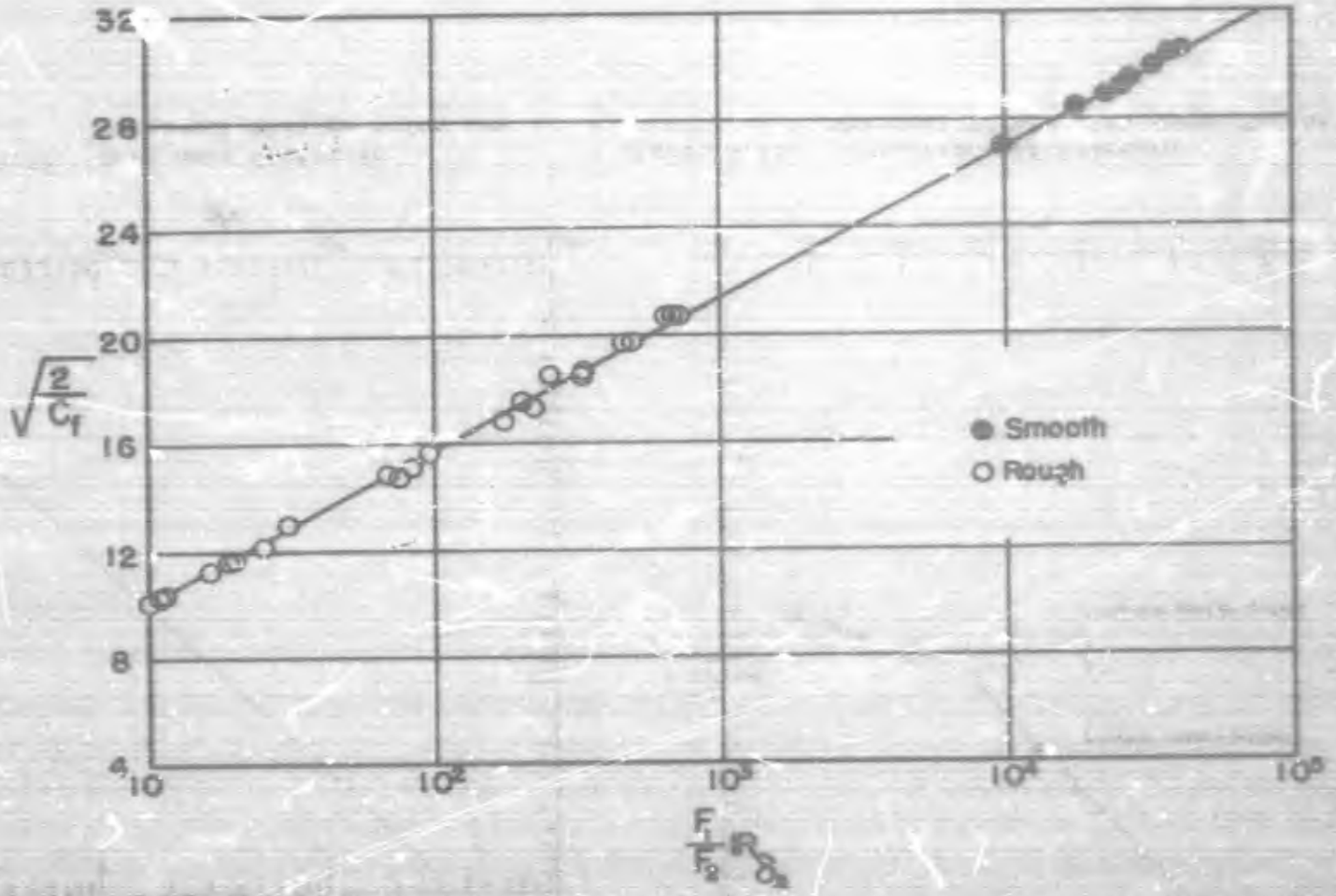

Figure 5.11: Universal Skin Friction Law

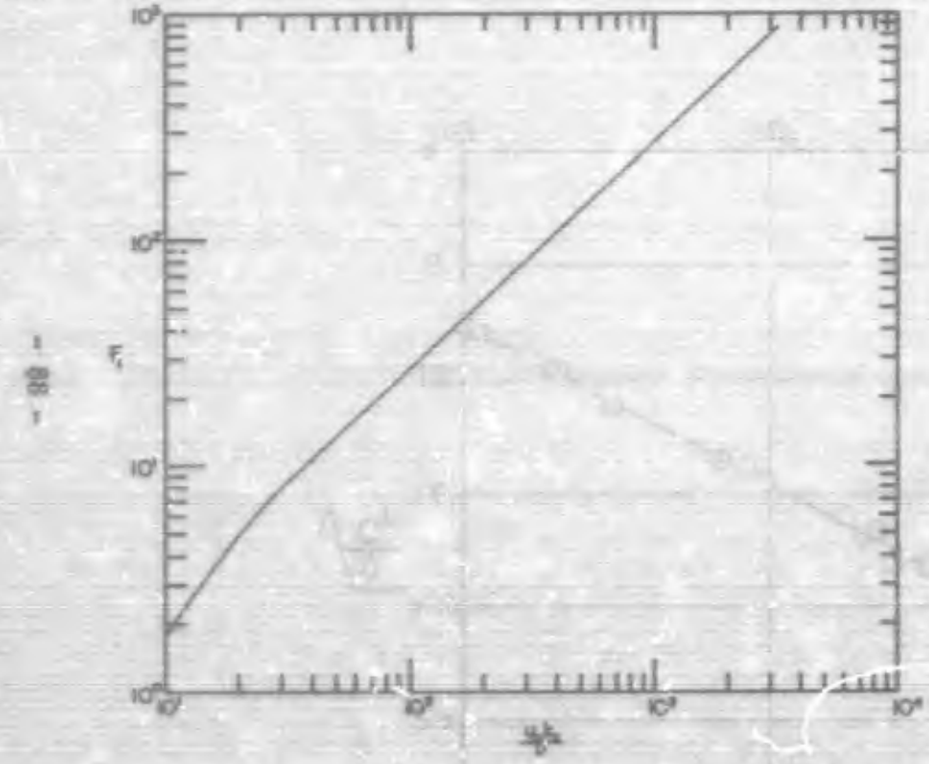

Figure 5.12: Roughness Factor in Universal Skin Friction Law

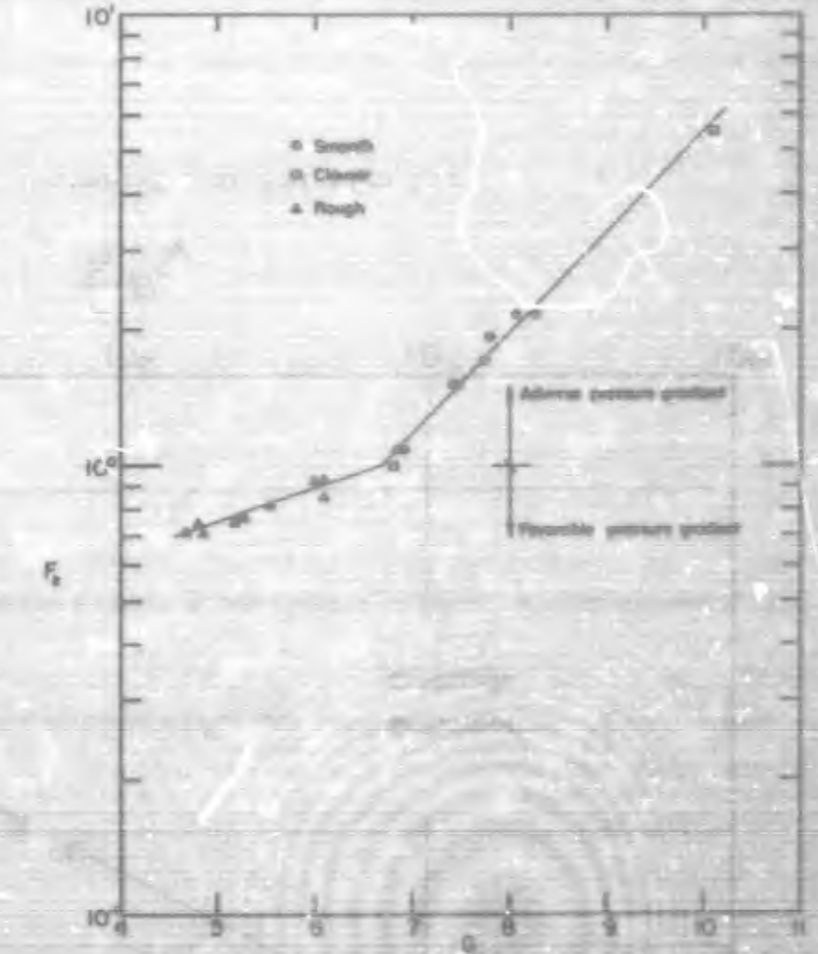

Figure 5.13: Correlation of Pressure Gradient Effect with Shape Factor

$$F_1 = \log^{-1}\left(\frac{\Delta u_1}{5.6u_*}\right) \tag{5.25}$$

The relation given by equation 3.67,

$$\sqrt{\frac{2}{C_f}} = 5.6 \log\left(\frac{F_2}{F_1}\right)\left(\frac{U_* \delta}{\nu}\right) + 4.5$$

appears to fit the experimental results for smooth and rough walls very well. Unfortunately, this law is difficult to apply in practice, since velocity profiles are required to determine the skin friction. For reference, the factors F_1 and F_2 are plotted in Figures 5.12 and 5.13. F_1 is given as a function $u_* k_s/\nu$ where k_s is the equivalent sand grain roughness. F_2 is presented as a function of the shape parameter, (see equation 5.15):

$$G = \frac{U}{u_*}\left(\frac{H - 1}{H}\right) \tag{5.26}$$

The data obtained by Clauser for three equilibrium profiles are also presented; the agreement between the two experimental investigations is quite acceptable.

3.2.4 Boundary Layer Growth

The variation of momentum thickness with distance along the roof is given in Figure 5.14 for each roughness height. In Figure 5.15 the same data are plotted versus the relative distance x/k_s. A reasonable approximation to a power law is noted. A simple argument for a power law variation is given by the following derivation. Neglecting pressure gradients, the Von Karman momentum integral relation is given by

$$\frac{d\theta}{dx} = \frac{C_f}{2} = \left(\frac{u_*}{U}\right)^2 \tag{5.27}$$

An approximation for the velocity profile is given by a power law in the form

$$\frac{u}{U} \propto \left(\frac{y}{\delta}\right)^{1/n} \tag{5.28}$$

A relation for shear stress may be given by

$$\tau_o = C_D \rho \bar{u}_k^2 \tag{5.29}$$

where C_D is a constant

$\bar{u}_k$ is the velocity at the peak of the roughness

Since by definition:

$$\frac{\tau_o}{\rho} = u_*^2 \tag{5.30}$$

and from equation 5.28:

$$u(k) = U \left(\frac{k}{\delta}\right)^{1/n} \tag{5.31}$$

it follows that

$$\frac{u_*}{U} = \sqrt{C_D} \left(\frac{k}{\delta}\right)^{1/n} \tag{5.32}$$

Within the power law approximation the ratio θ/δ is a constant defined by

$$\frac{\theta}{\delta} = \frac{n}{(n+1)(n+2)} \tag{5.33}$$

therefore, equation (5.32) may be written in the form

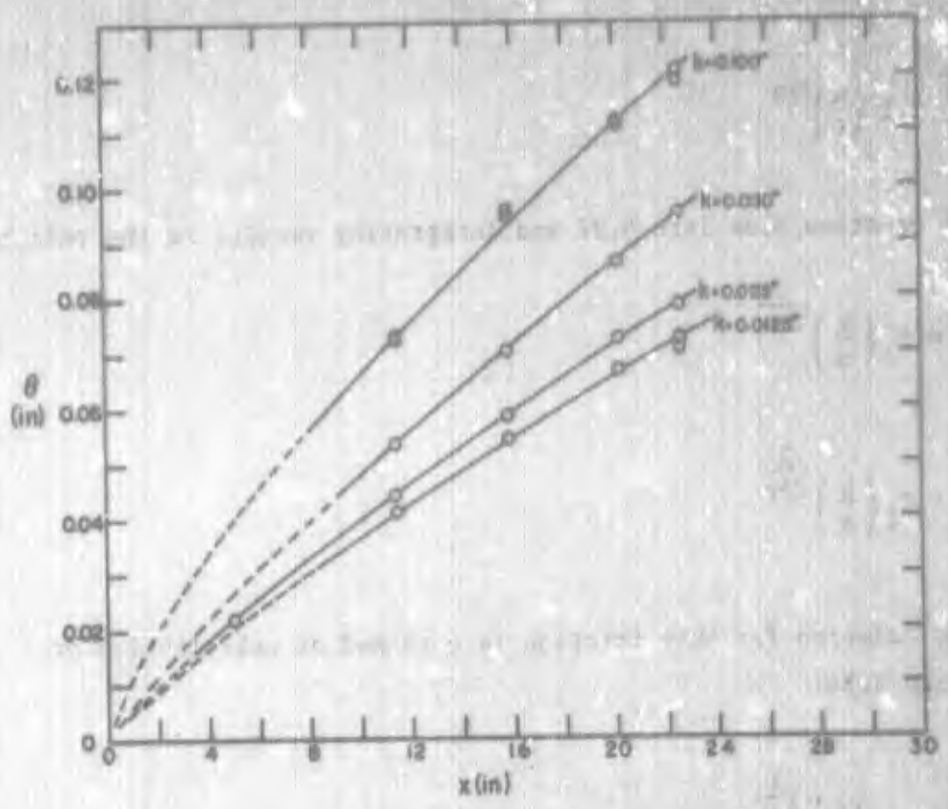

Figure 5.14: Boundary Layer Growth

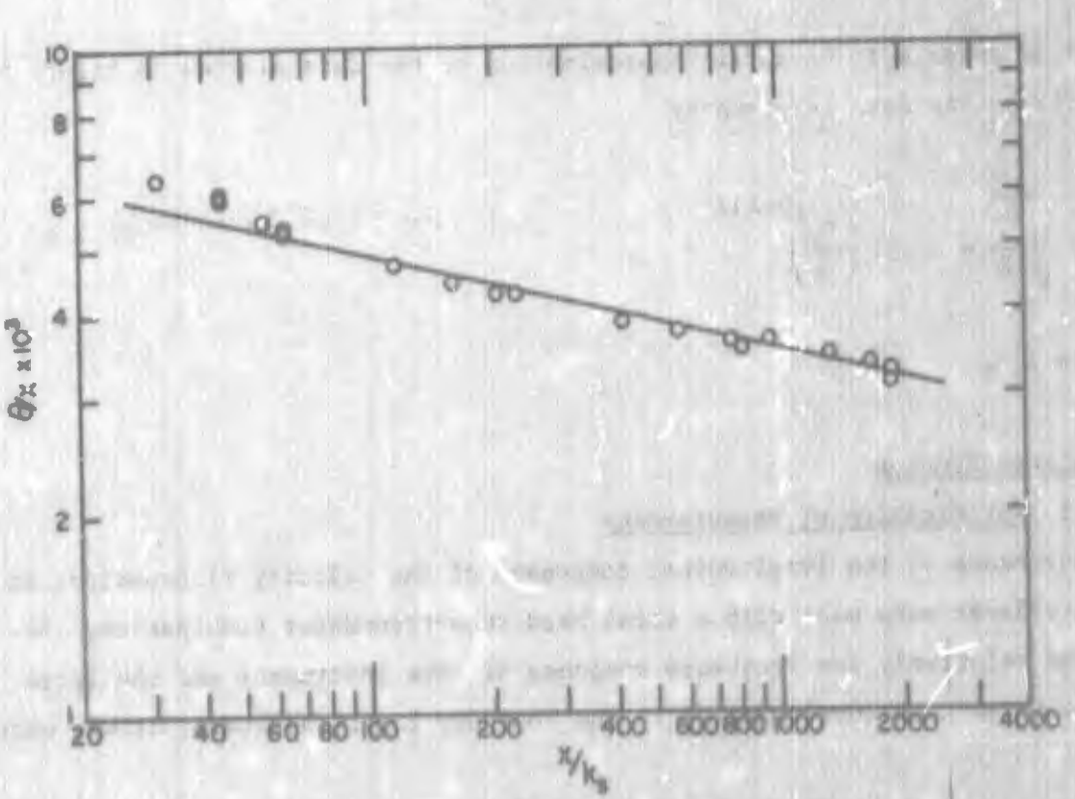

Figure 5.15: Normalised Boundary Layer Growth

$$\left(\frac{u_s}{U}\right)^2 = C\left(\frac{k}{\theta}\right)^{2/n} \tag{5.34}$$

Substitution of equation 5.34 into 5.27 and integrating results in the relations:

$$\frac{\theta}{x} = C_1\left(\frac{k}{x}\right)^{\frac{2}{2+n}} \tag{5.35}$$

$$\frac{\delta}{x} = C_2\left(\frac{k}{x}\right)^{\frac{2}{2+n}} \tag{5.36}$$

Also a power law relation for skin friction is obtained by substitution of equation 5.35 into 5.34:

$$\sqrt{\frac{C_f}{2}} = C_3\left(\frac{k}{x}\right)^{\frac{1}{2+n}} \tag{5.37}$$

Equation 5.37 appears to be a fair approximation to the data plotted in figure 5.10. The best fit to the data is given by

$$\sqrt{\frac{C_f}{2}} = 0.157\left(\frac{k_s}{x}\right)^{0.152} \tag{5.38}$$

wherein n = 4.6.

5.3 Turbulence Studies

5.3.1 Verification of Measurements

Measurements of the longitudinal component of the velocity fluctuations in the boundary layer were made with a total head tube-transducer combination. Because of the relatively low frequency response of this instrument and the large size of the total head tube relative to the boundary layer thickness, it was necessary

to perform some experiments which could be compared with previous hot-wire investigations. The measurements closely parallel to the present study were the experiments of Klebanoff (1955) on a smooth flat plate. The boundary layer studied by Klebanoff was "tripped" to insure a fully turbulent flow at the working section. However, Bull, et. al., (1963) found that the turbulence characteristics in a boundary layer with a natural transition from laminar to turbulent flow are somewhat different. For comparison purposes, several turbulence runs were made near the smooth roof used in this study. The boundary layer on the roof may be considered as tripped since there is some slight mismatch (.002") between the nozzle and the test section. Therefore, the best agreement should be expected with Klebanoff's data. The smooth roof is probably the worst possible case for study since the boundary layer is very thin, being approximately 0.3 inches thick. Thus, the highest frequencies encountered in this study can be expected for this case along with the greatest probe interference effects. In Figure 5.16, the results of four runs ranging in Reynolds number $U\delta/\nu$ from 3.88×10^4 to 9.76×10^4 are compared with Klebanoff's data (1955) in air at a Reynolds number of 7.39×10^4. The data, which are normalized with respect to shear velocity, compare quite favorably over most of the boundary layer especially in light of the fact that Klebanoff's experiments were performed in a boundary layer nearly 10 times thicker than the one investigated in the present study. There is some scatter at the outer portion of the boundary layer but this could be due to the differences in free stream turbulence in the two facilities. The data of Bull, et. al., (1963) are also plotted in the figure, which cover a Reynolds number range of 1.14×10^5 to 3.76×10^5. The disagreement is marked and remains to be explained. However, both the present results and the Klebanoff data agree in the inner portion of the boundary layer with the mean of previous investigations of the turbulent flow in smooth conduits cited by Graveto (1967). Disagreement must be expected in the outer portion, since there the turbulence is intermittent. It was concluded that reliable values of turbulence intensity could be obtained with the total head tube.

A further correlation with hot wire data is made in Figure 5.17. The results of experiments performed near the roofs having 0.0125 inch and 0.025 inch grooves are compared with the data of Corrsin and Kistler (1955) which were determined near a corrugated surface. Their roughness height was equal to 4.35% of the boundary

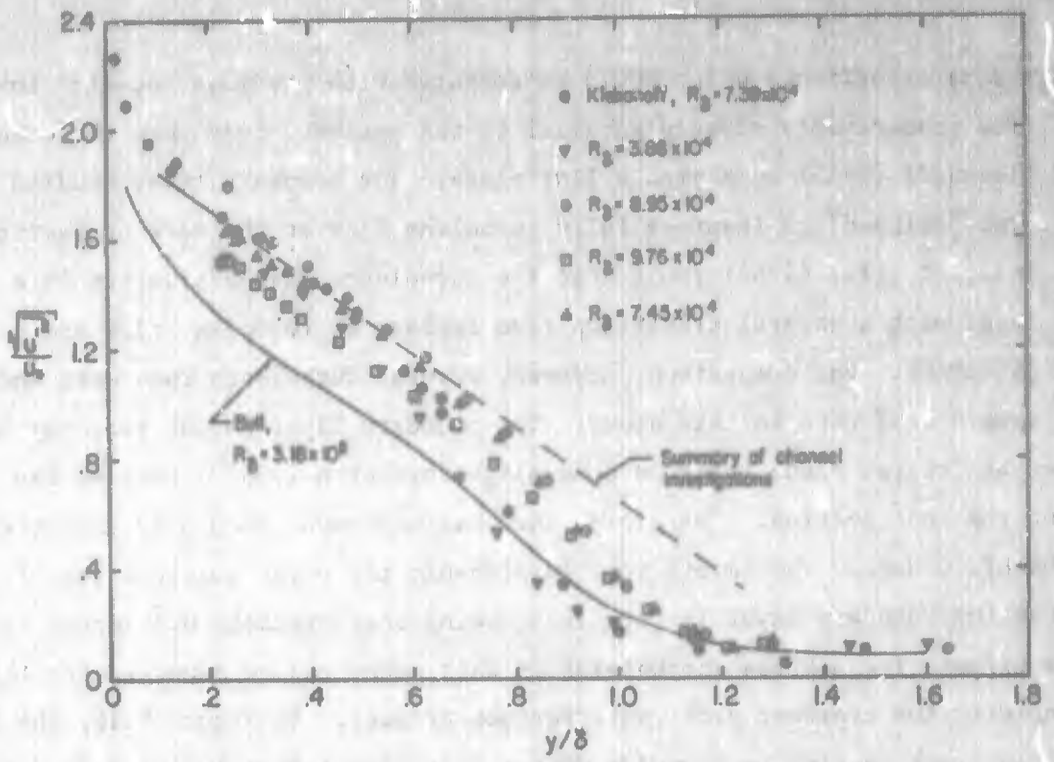

Figure 5.16: Verification of Turbulence Measurements (Smooth Wall)

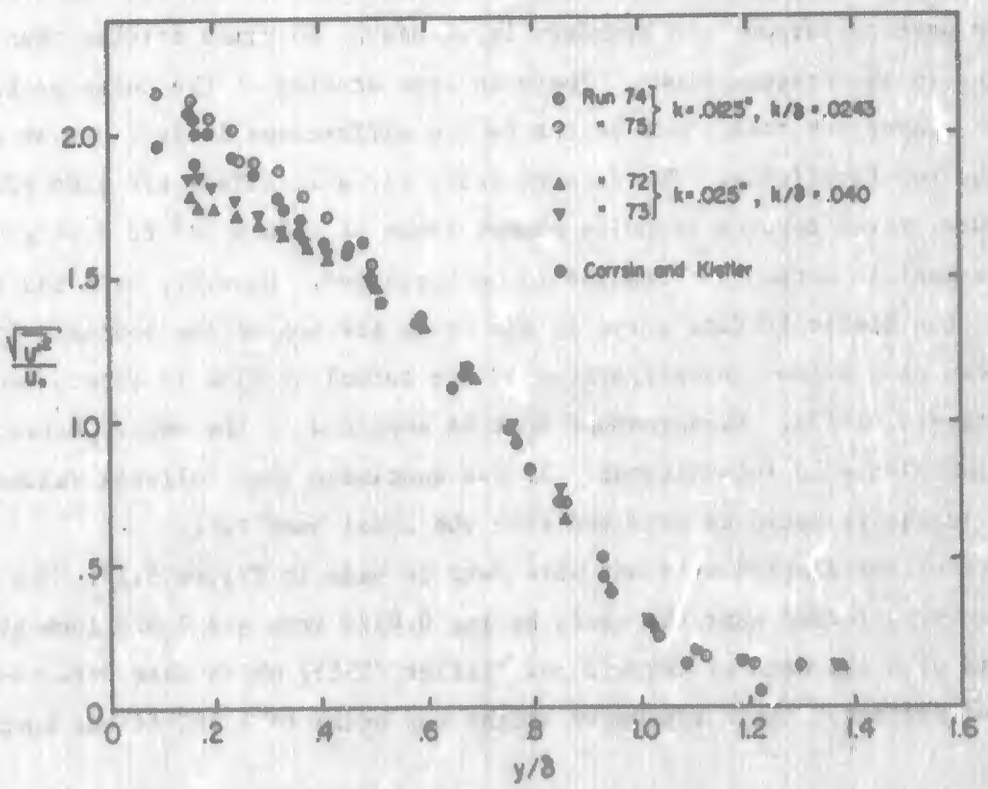

Figure 5.17: Verification of Turbulence Measurements (Rough Wall)

layer thickness and the ratio of shear velocity to free stream velocity was 0.0505. Some of the data of the present study had a relative roughness, k/δ, of 0.040 and 0.024, and the ratios of shear velocity to free stream velocity were 0.0536 and 0.0482 respectively. Therefore, the data obtained would be expected to bracket the Corrsin and Kistler results at distances of 10% to 80% of the boundary thickness from the wall. Resonably good agreement is apparent from inspection of Figure 5.17. This lends further weight to the reliability of the measuring technique used in this study.

5.3.2 Results of Turbulence Measurements near Rough Boundaries

The variation of turbulence intensity with distance from the wall is given in Figure 5.18. Four representative runs are shown for each roughened roof. The root mean square values of velocity fluctuations are normalized with respect to shear velocity, and the distance from the wall is expressed in terms of roughness height. The main feature immediately apparent from this presentation is the apparent lack of correlation with a length parameter equal to the roughness height when distances are greater than a few roughness heights from the wall. When the data are normalized with respect to boundary layer thickness as shown in Figure 5.19, there is substantial agreement in the outer portion of the boundary layer but a consistent deviation in the inner portion. This result is somewhat unexpected. As shown in Figure 5.20, normalization of the data with respect to length parameter,

$$\Delta = \frac{U}{u_*}\,\delta_*$$

results in the same trend except for the very good agreement between the various cases at a distance from the wall of $y/\Delta = 0.12$. This value corresponds to approximately 40% of the boundary layer thickness. Therefore, in the region of cavitation inception the turbulence intensity may be considered directly related to the wall shear. Closer to the wall, some as yet undefined additional parameter is apparently required to describe the turbulence. The region of disagreement extends to distances from the wall much greater than the region where the individual roughness protrusions could be expected to have some influence.

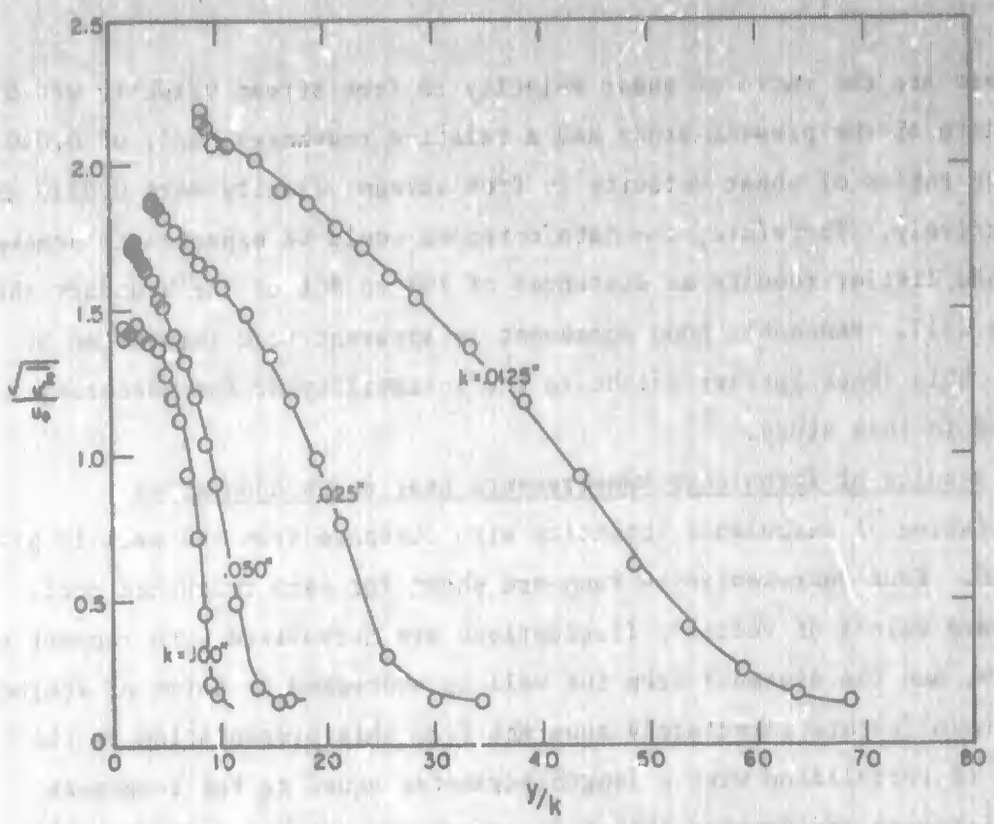

Figure 5.18: Turbulence Intensity near Rough Walls

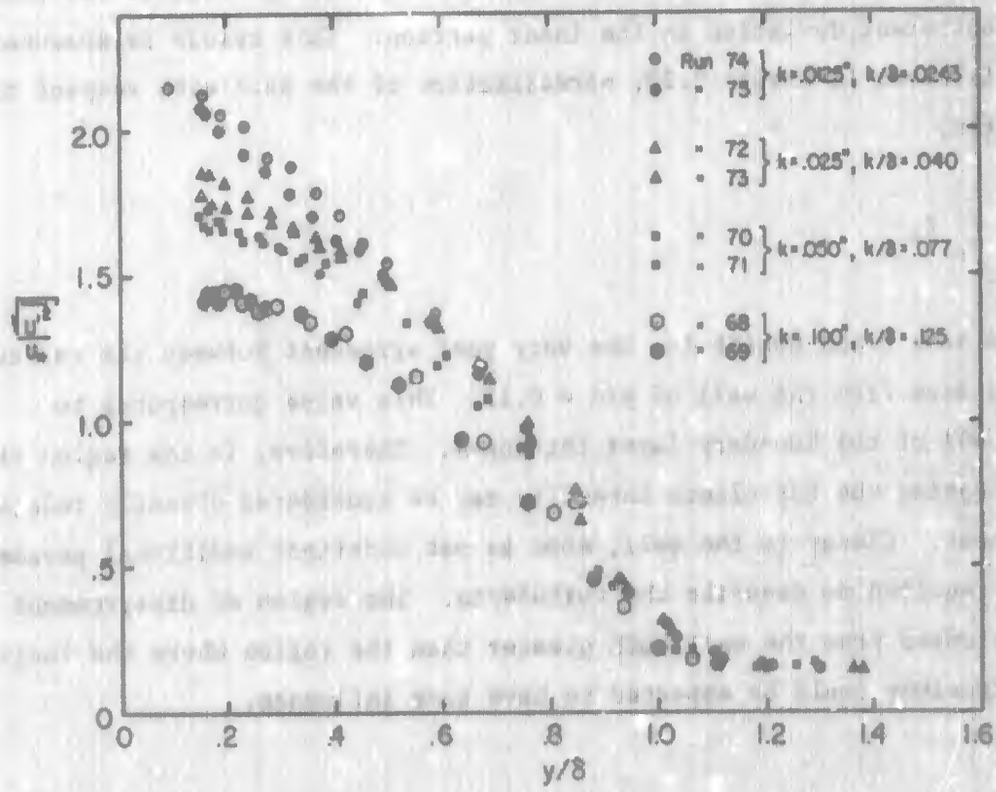

Figure 5.19: Variation of Turbulence Intensity Through Boundary Layer, Rough Walls

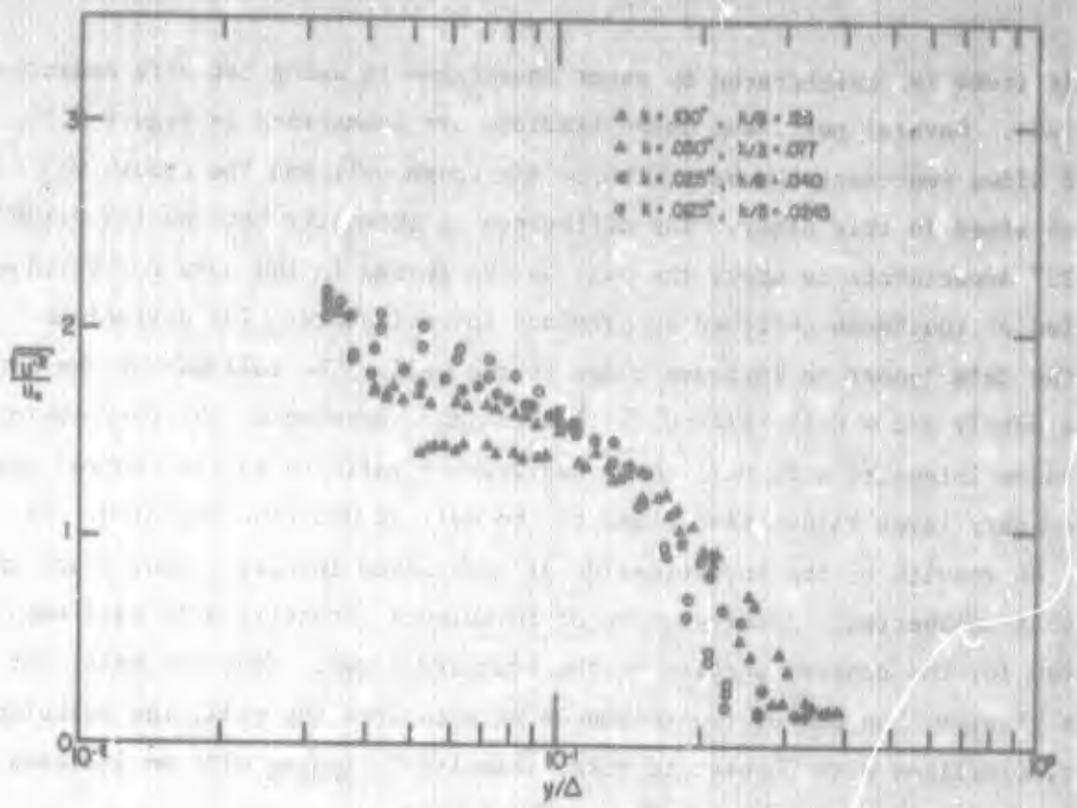

Figure 5.20: Variation of Turbulence Intensity Through Boundary Layer

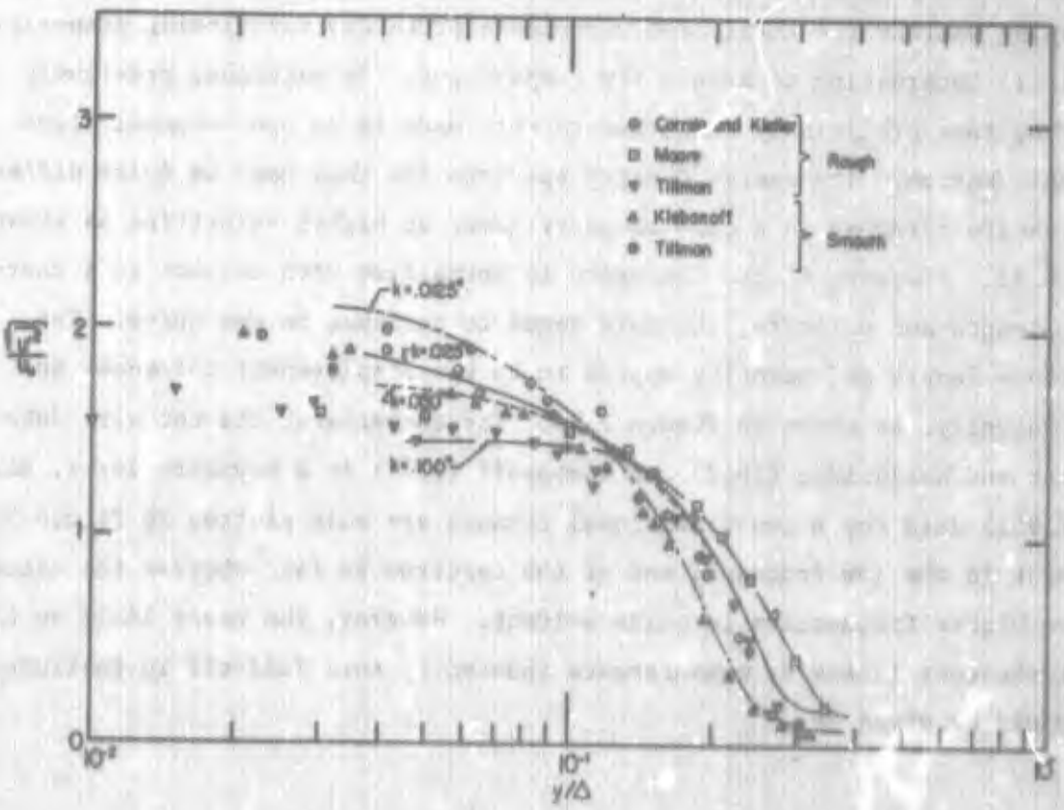

Figure 5.21: Comparison of Rough Wall Turbulence Data with Previous Investigations

This trend is corroborated by other investigators using hot wire measurements in air. Several pertinent investigations are summarized in Figure 5.21. The solid lines represent the best fit for the rough wall and the smooth wall results obtained in this study. The difference in intensity between the 0.100" and 0.0125" experiments is about the same as the spread in the data for various intensities of roughness obtained by previous investigators. The deviations between the data appear to increase close to the wall. The collapse of the data at approximately $y/\Delta = 0.12$ ($y/\delta \simeq 0.4$) is striking. Apparently the correlation of turbulence intensity with wall shear has greater validity in the central portion of the boundary layer rather than close to the wall as would be expected. In summary, the results of the investigation of turbulence intensity near rough walls are somewhat unexpected. A correlation of turbulence intensity with wall shear is achieved for the central portion of the boundary layer. Near the wall, but at distances greater than one or two roughness heights from the wall, the turbulence intensity, normalized with respect to shear velocity, decreases with an increase in roughness. This point warrants further investigation.

5.3.3 Energy Density Spectra

Energy density spectra were determined in this study only for the purpose of determining whether the total head turbulence probe was functioning properly. However, it is interesting to make a few comparisons. As mentioned previously in Chapter 4, some preliminary measurements were made in an open-channel flume with a smooth bottom. The energy density spectrum for this case is quite different from the results obtained in a thin boundary layer at higher velocities as shown in Figure 5.22. However, if the frequency is normalized with respect to a characteristic length and velocity, the data tends to collapse to one curve. The best reference length and velocity appear to be the displacement thickness and the local velocity, as shown in Figure 5.23. For comparison, the hot wire data of Willmarth and Wooldridge (1962) and Klebanoff (1955) in a boundary layer, and Laufer's (1951) data for a two-dimensional channel are also plotted in Figure 5.23. The agreement in the low frequency end of the spectrum is fair whereas the distortion in the higher frequencies is quite evident. However, the upper limit on the error in turbulence intensity measurements induced by this fall-off in instrument response would be given by

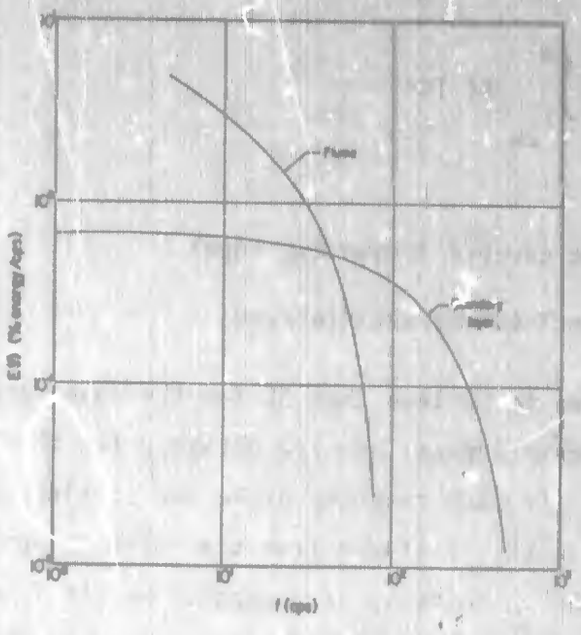

Figure 5.22: Energy Density Spectra for Plume and Boundary Layer

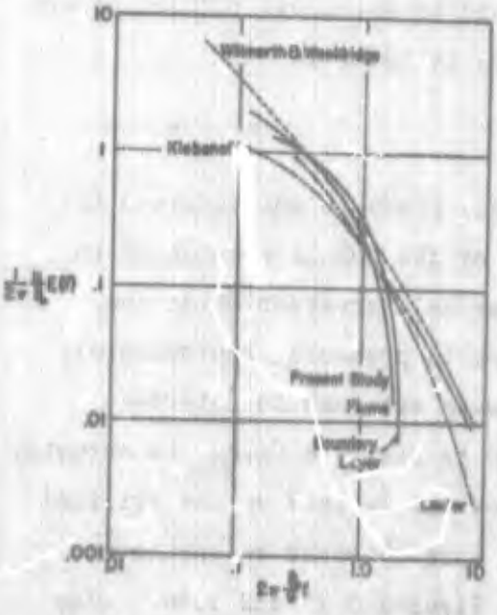

Figure 5.23: Normalized Energy Density Spectra for Smooth Boundaries

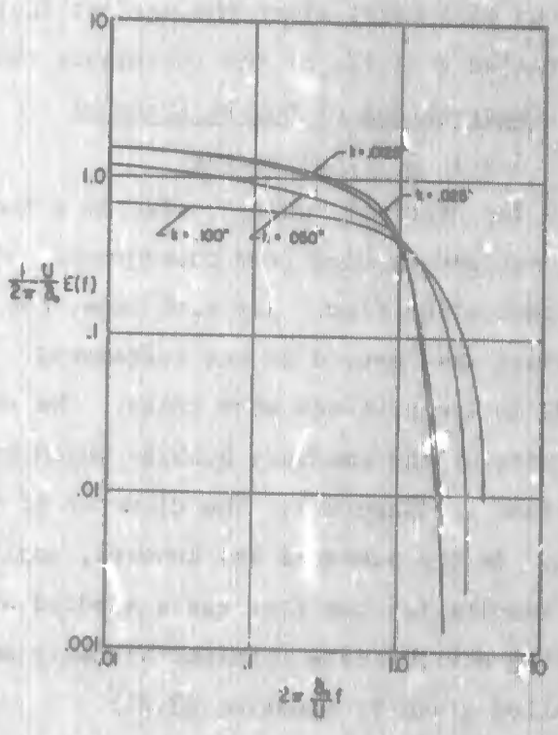

Figure 5.24: Energy Density Spectra for Rough Boundaries

$$\% \text{ Error} < \int_{f_{cu}}^{\infty} E(f)df$$

where f_{cu} is the cut-off frequency, (cps)

$E(f)$ is the % energy/cycle/second

This error is estimated to be less than 5% for the cases studied in this investigation. Typical energy density spectra obtained for the roughened roofs are shown in Figure 5.24. In each case the probe was resting on the crests of the roughness thus the effective distance from the datum is approximately half the probe diameter or 0.060". In terms of roughness height from the datum, the distances were 6.5, 2.9, 1.9, and 1.2 for the respective roughness heights of 0.0125, 0.025, 0.050, and 0.100 inch. The energy density spectra for the smaller roughness heights agree quite well with the spectra obtained near smooth boundaries. Spectra obtained for the rougher surfaces show some influence of the roughness as indicated in Figure 5.24. However, no further mention of energy density spectra will be made here, since the present instrument should be developed further before a detailed analysis of the turbulence characteristics is feasible.

5.4 Observations of Bubble Dynamics

5.4.1 Critical Radius

The critical bubble radius as a function of wall pressure was obtained for each surface studied from photographic observations of the bubble population in the cavitating flow. For each case, the velocity was held constant while the pressure was lowered in set increments. At each step in pressure, approximately 1,000 motion pictures were taken. The photographs were examined to determine the size of the smallest bubbles which were observed to cavitate (i.e., to abruptly increase in diameter). The diameter of these bubbles was defined as the critical size. As the pressure was lowered, smaller bubbles were observed to cavitate. The results for the four cases studied are shown in Figures 5.25 and 5.26. Also plotted are the data obtained by Daily and Johnson (1956) and the bubble stability relation given by Equation (3.21)

$$p^* = -\frac{4\sigma}{3R^*}$$

The value of surface tension used in equation 3.21 was .00494 lb/ft which corresponds to a temperature of 25.7°C. This was the average temperature of the water during this phase of the test program. The dotted lines in the figure represent the theoretical relation shifted upward by a constant amount of pressure, the value of which corresponds to the difference between the wall pressure and the minimum pressure in the boundary layer. The theoretical relation appears to fit the data for the smooth wall and for the lowest intensity of roughness. However, with increasing degree of roughness there is less agreement. This could be due to an attenuation of the turbulence intensity with an increase in the intensity of cavitation, thus, reducing the difference between the wall pressure and the minimum pressure in the flow. Unfortunately, the velocity for each set of runs was not constant, thus direct comparison between data for various roughness heights is not possible in Figures 5.25 and 5.26. For reference, experimental points are replotted in Figure 5.27 where pressure has been normalized with respect to free stream dynamic pressure. At large values of the critical radius the data should be asymptotic to the value of the incipient cavitation index defined as

$$\sigma_i = \frac{p_{wall} - p_{vp}}{\rho \frac{U^2}{2}} \tag{5.39}$$

One set of data, (k = .050) was inconsistent, the values of normalized pressure were higher than the incipient cavitation index indicating an error in pressure measurements, since the pressure values should be lower than for incipient cavitation. These data were shifted downward by an amount equal to 1% of the velocity head. The difference in the cavitation characteristics for the case k = 0.100" is rather startling. When the pressure was lowered below the incipient value by relatively small amounts (10-30 mm of mercury) the cavitation process was observed

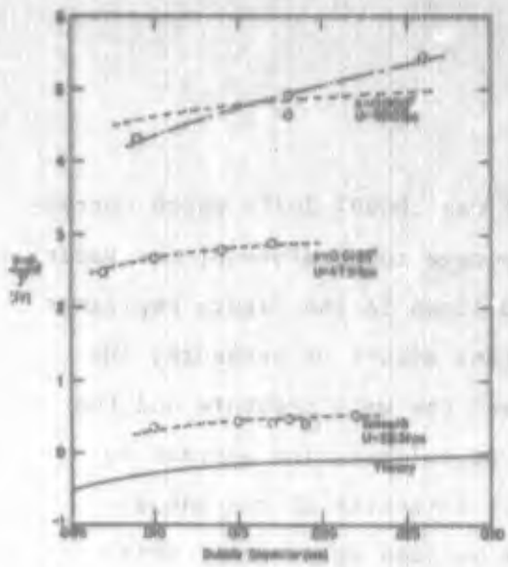

Figure 5.25: Wall Pressure versus Critical Radius

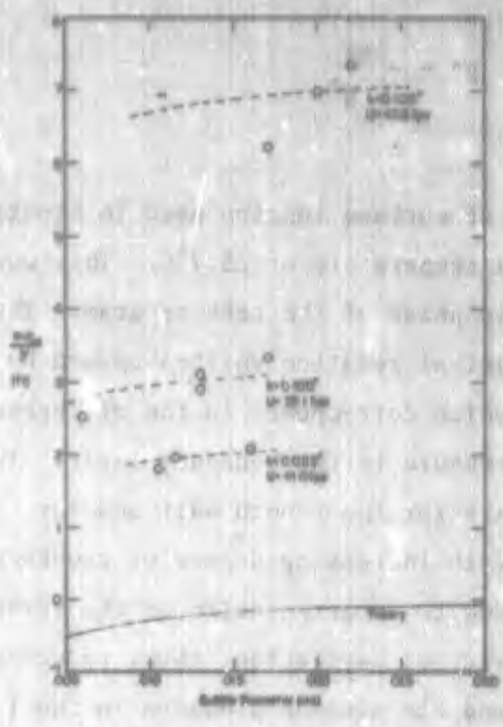

Figure 5.26: Wall Pressure versus Critical Radius

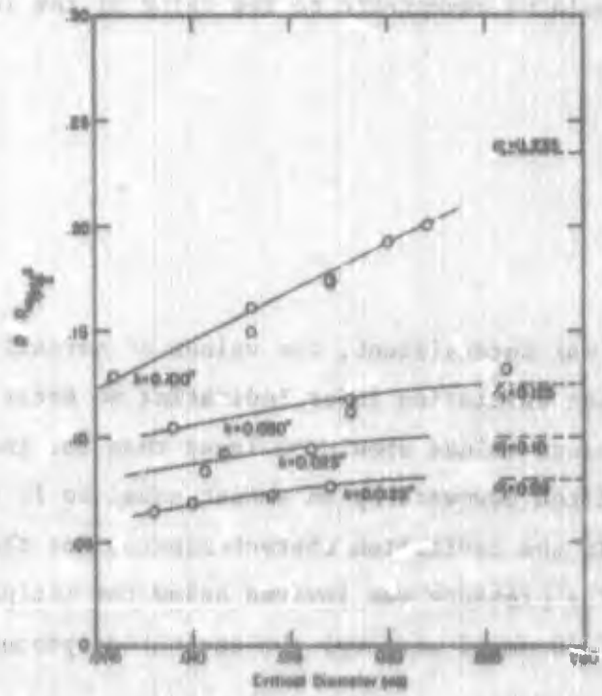

Figure 5.27: Normalized Wall Pressure versus Critical Radius

to be quite profuse. It is suggested that cavitation alters the pressure distribution through the boundary layer. The extreme case would be a fully developed cavity adjacent to the wall, where the pressure would be equal to the vapor pressure everywhere. Therefore, it is hypothesized that the relatively large reduction in wall pressure required to lower the value of the critical radius does not correspond to the same reduction in the pressure outside the bubbles. As noted in Chapter 3, the stability theory is based on a simple equilibrium between the external and internal pressure and the surface tension. Therefore, it is the local value of pressure and not the wall pressure that is pertinent. This local value is not a mean value, but a value corresponding to the negative peak of turbulent pressure fluctuations. These turbulent pressure fluctuations are related to the vorticity in the flow and the fluid density. As portions of the fluid are vaporized, there are drastic reductions in density. For angular momentum to be conserved, there must be a reorientation of the vorticity distribution which in turn will modify the nature of the pressure fluctuations.

5.4.2 Bubble Growth

Typical photographs of expanding bubbles taken at 3,000 frames per second are shown in Figures 5.28 and 5.29. A plot of the bubble radius versus time for the two cases shown is given in Figure 5.30. A good portion of the growth phase may be approximated by a straight line as predicted by equation 3.19:

$$R' = \frac{2}{3}\sqrt{\frac{P_{vp} - P_{\infty}}{\rho}}$$

Using this relation, and the measured R' given by the slopes of the straight lines in the graph, it is possible to compute the quantity $P_{vp} - P_{\infty}$. The values obtained from the bubble growth data agree reasonably well with the values computed from the stability theory as shown in Table 5.3. These results lend further support to the hypothesis that relatively large reductions in wall pressure below the incipient point do not necessarily produce corresponding reductions in the pressure external to the bubble.

Another observation is that quite often bubbles appeared to grow beyond a steady state value and then began to collapse at approximately the same rate they

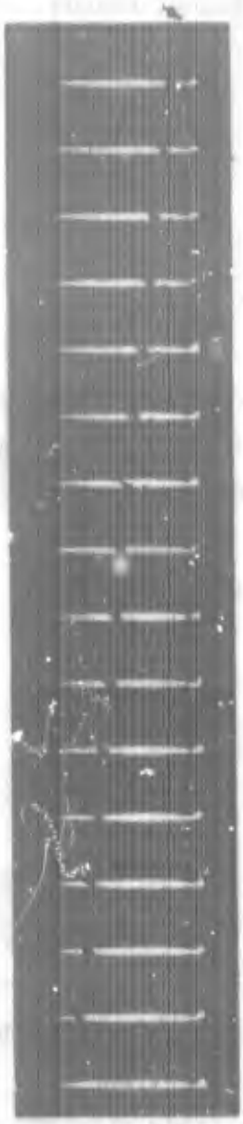

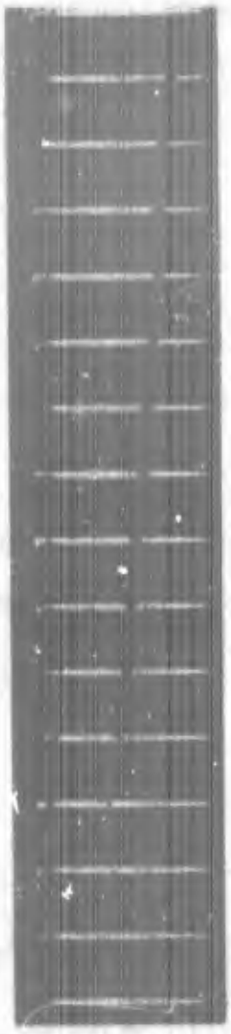

Run P47
k = 0.025"

Run P35
k = 0.100"

Figures 5.28 and 5.29:
Typical Bubble Sequences

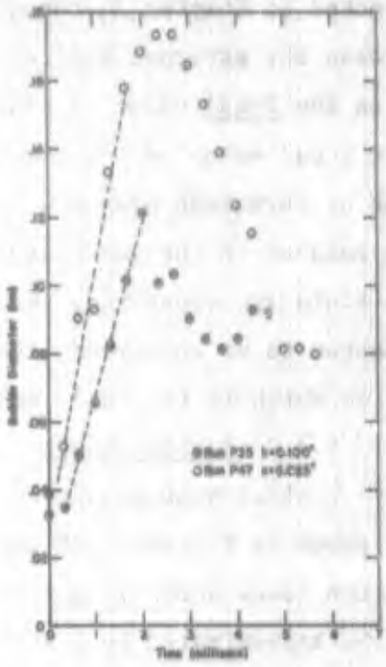

Figure 5.30: Typical Bubble Growth History

Table 5.3

Summary of Bubble Growth Data

k (inches)	Run No.	$\frac{P_{vg} - P_\infty}{\gamma}$ (Growth Data - Ft.)	d_{cr} (inches)	$\frac{P_{vg} - P_\infty}{\gamma}$ (Stability Data - Ft.)
0.100	P33	0.48	0.013	0.195
		0.10		
		0.25		
		1.54		
		0.67		
	P34	1.23	0.013	0.195
		0.76		
		0.29		
		0.69		
		0.34		
	P35	0.77	0.006	0.422
		0.48		
	P37	0.26	0.017	0.149
0.050	P59	0.53	0.026	0.097
		1.46		
	P60	0.76	0.009	0.281
		0.58		
	P61	0.47	0.018	0.141
	P62	0.81		
		0.18		
0.025	P43	0.30	0.010	0.253
		0.21		
	P44	3.81	0.016	0.158
		1.07		
	P47	2.28	0.012	0.220
		1.50		
0.0125	P51	1.97	0.014	0.181
		0.[illegible]		
		1.89		
	P52	0.54	0.017	0.149
		0.28		
		1.07		
	P53	1.56	0.010	0.253
		1.01		
		1.06		
	P54	0.44	0.007	0.361

had grown. The bubbles leave the field of view many times larger than the initial value but smaller than the observed maximum size. The pressure gradient was very mild for all phases of this study and actual collapse of bubbles did not occur in the test section. Collapse always occurred in the transition part downstream of the test section. Thus, the observations in this study are quite different from those of Knapp (1948), where within the field of view of the camera, the bubbles traversed through a distinct minimum pressure region into a higher pressure region. In Knapp's experiments a variation of p_∞ was approximated by the variation in mean static pressure sensed by the bubble as it passed through the minimum pressure region. In the present study, the important factor is the temporal variation of pressure due to turbulence.

5.4.3 Bubble Distribution

The distribution of bubbles through the boundary layer was also obtained from high speed photographs of the cavitating flow. The number of bubbles in each of 10 strips of 1/10 of a boundary layer thickness were counted in random frames. The total number of bubbles counted for each run was about 2,000. For each case the procedure was repeated to determine the distribution of only the cavitating bubbles. The resulting histograms are shown in Figures 5.31 through 5.45. The solid lines indicate the percentage of all bubbles at each portion of the boundary layer. The dotted lines display the percentage of expanding bubbles as a function of distance through the boundary layer. Figures 5.46 through 5.49 are a summary of the data obtained for each of the four roughness patterns studied. The striking feature of these data is the fact that in all cases cavitation is observed to occur roughly in the center of the boundary layer. On the other hand the maximum percentage of all bubbles is close to the wall. The only explanation for this phenomenon is that the minimum peaks in instantaneous pressure occur in the center of the boundary layer and not close to the wall where the mean static pressure is a minimum as predicted by equation 3.43.

Daily and Johnson (1956) also observed cavitation to occur in the center of the boundary layer adjacent to a smooth roof. They theorized that the boundary layer is composed predominately of large scale eddies having a diameter approximately equal to the boundary layer thickness. It was concluded that the cavitation nuclei were entrained in the cores of these eddies, and cavitation would occur in

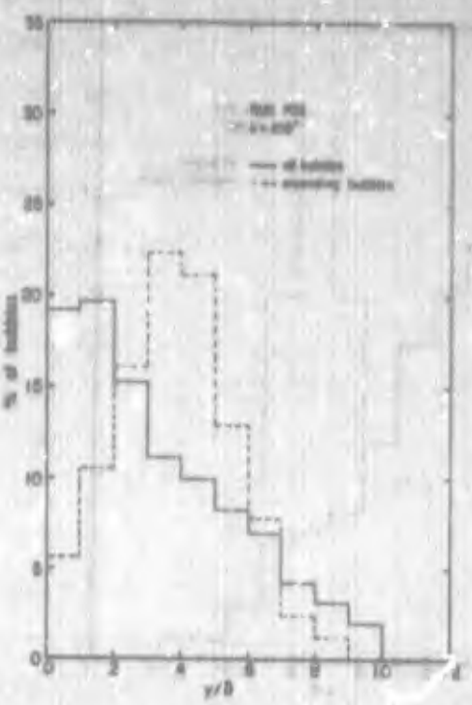

Figure 5.31: Bubble Distribution Data, k = .100"

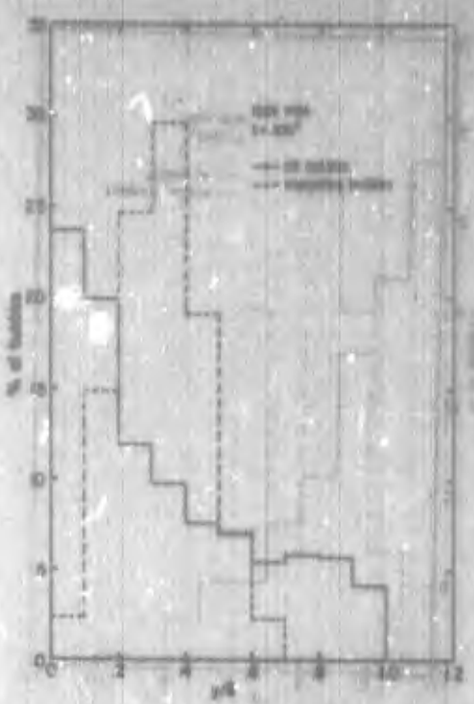

Figure 5.32: Bubble Distribution Data, k = .100"

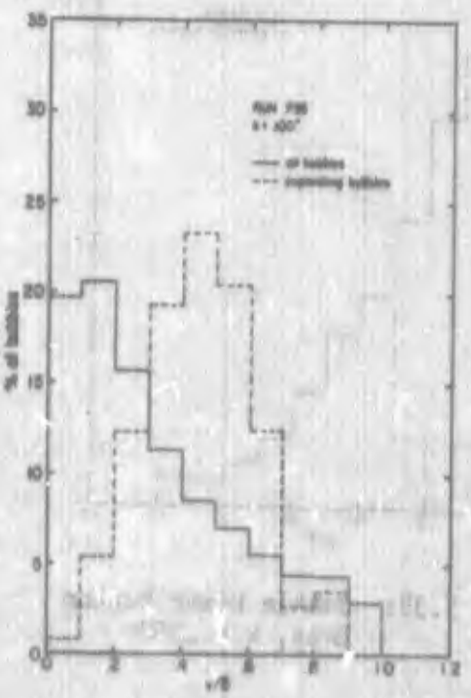

Figure 5.33: Bubble Distribution Data, k = .100"

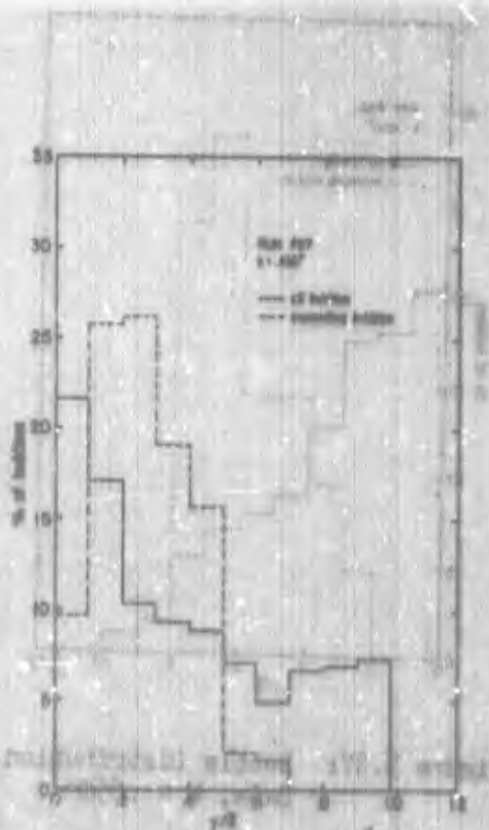

Figure 5.34: Bubble Distribution Data, k = .100"

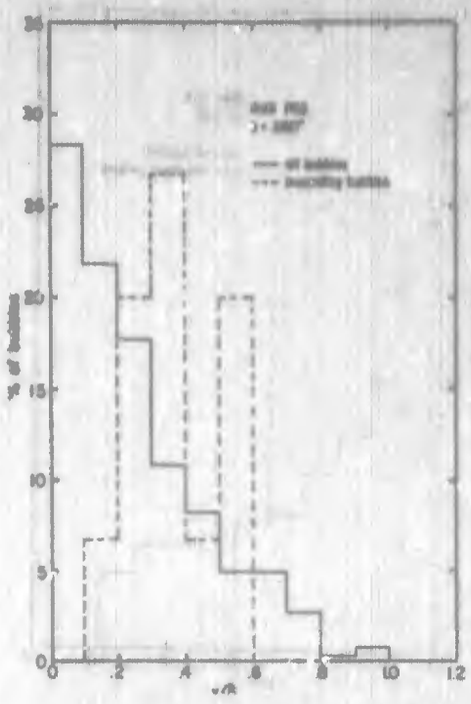

Figure 5.35: Bubble Distribution Data, k = .050"

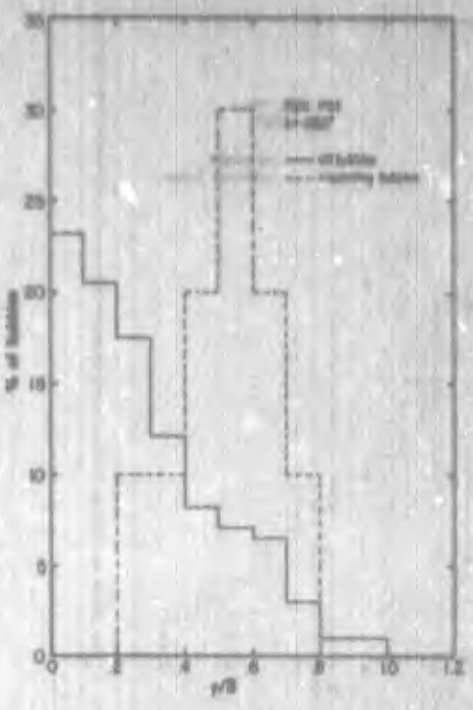

Figure 5.36: Bubble Distribution Data, k = .050"

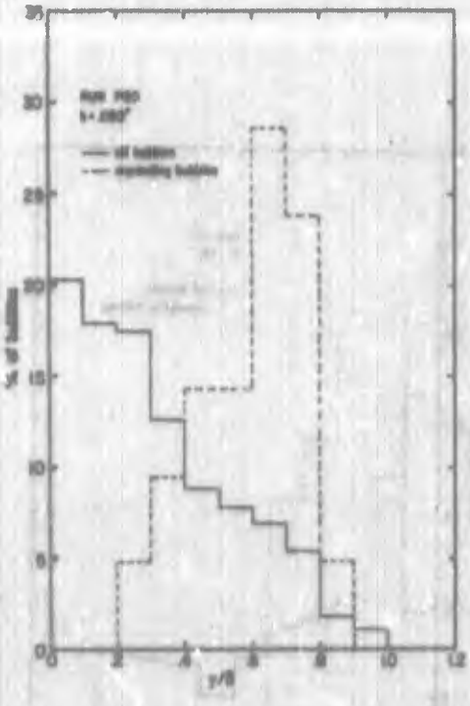

Figure 5.37: Bubble Distribution Data, k = .050"

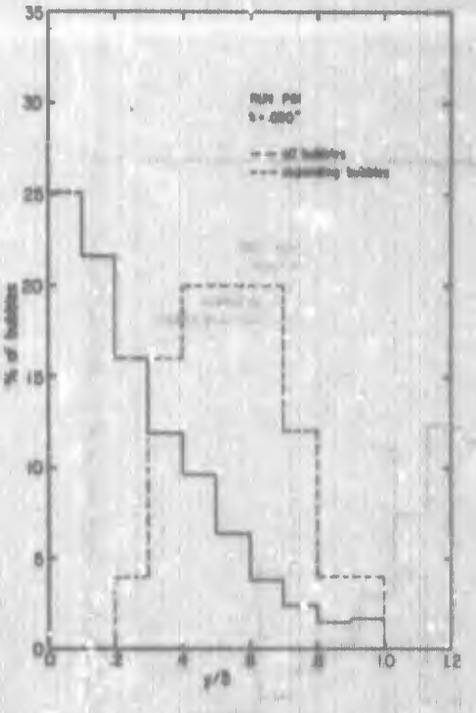

Figure 5.38: Bubble Distribution Data, k = .050"

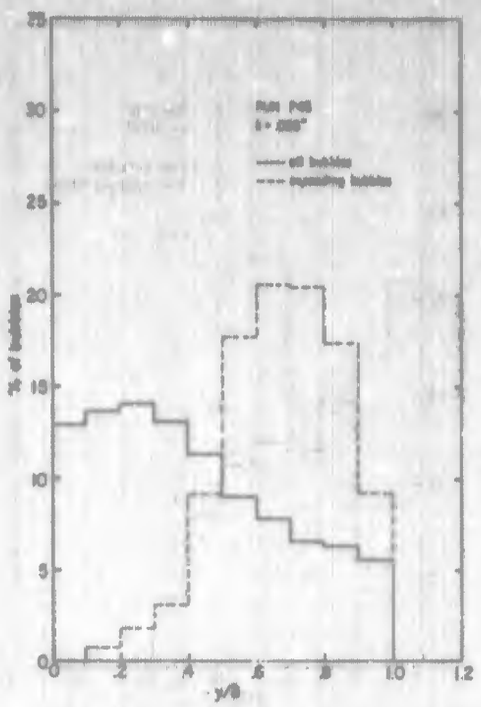

Figure 5.39: Bubble Distribution Data, k = 0.025"

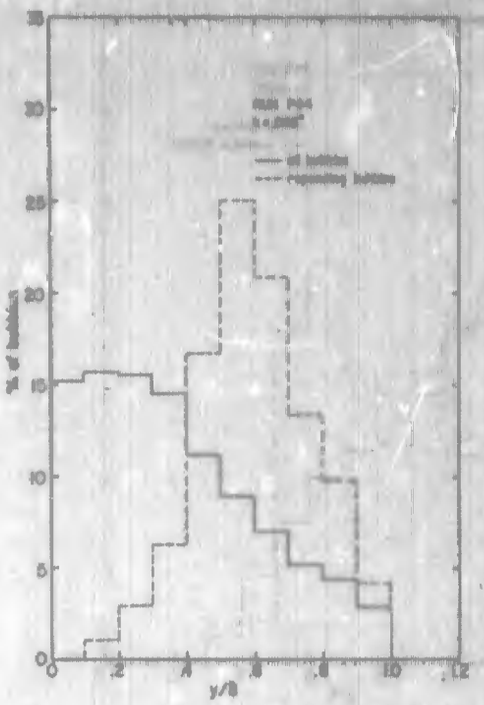

Figure 5.40: Bubble Distribution Data, k = 0.025"

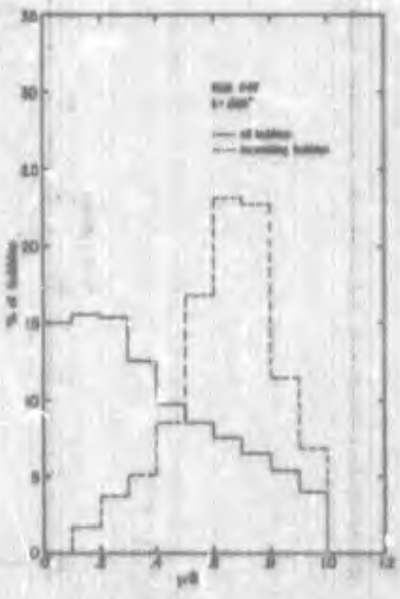

Figure 5.41: Bubble Distribution Data, k = 0.025"

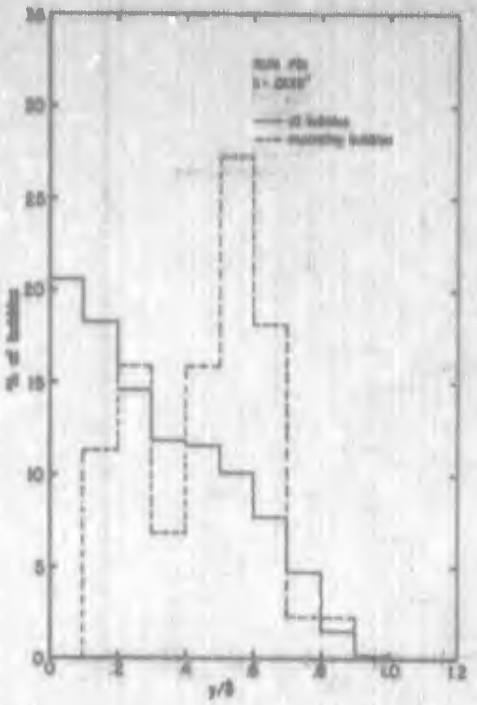

Figure 5.42: Bubble Distribution Data, k = 0.0125"

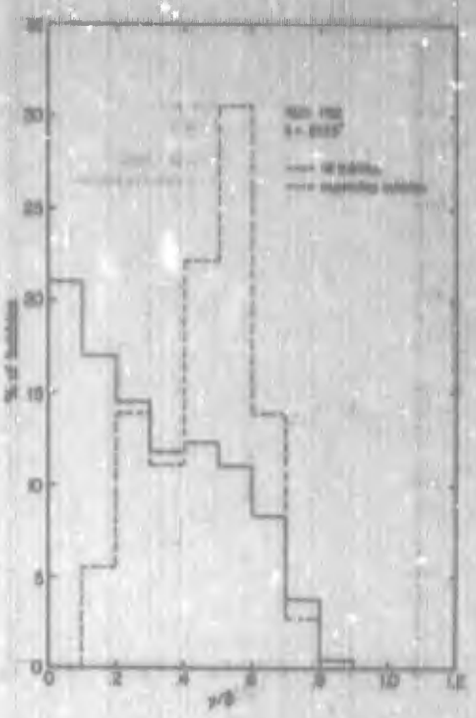

Figure 5.43: Bubble Distribution Data, k = 0.0125"

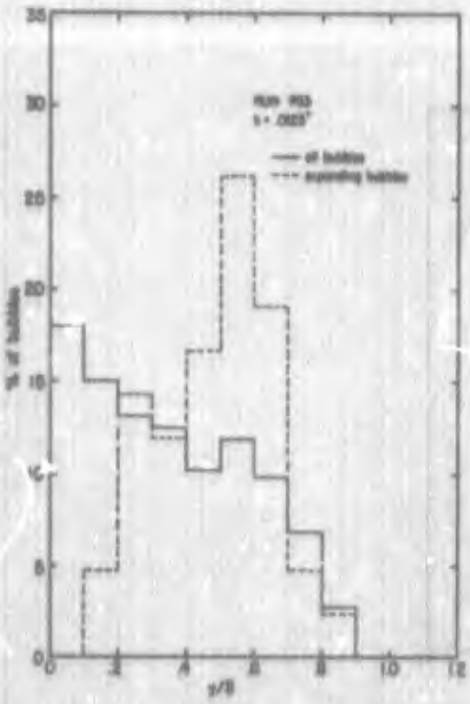

Figure 5.44: Bubble Distribution Data, k = 0.0125"

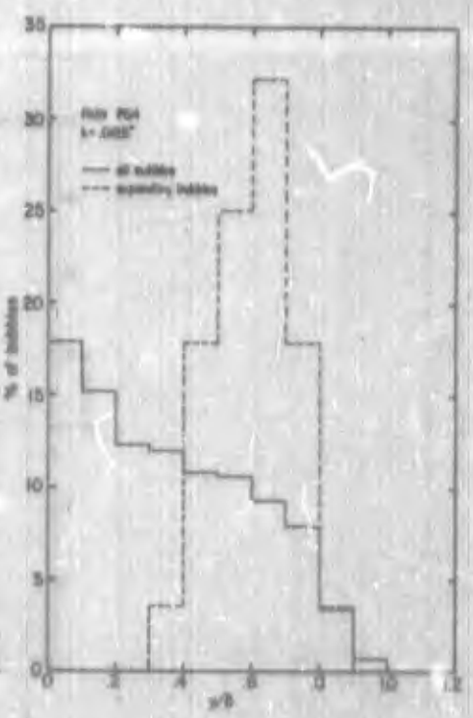

Figure 5.45: Bubble Distribution Data, k = 0.0125"

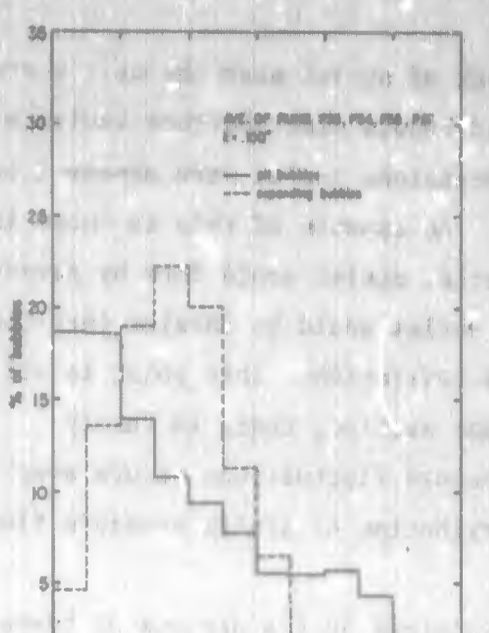

Figure 5.46: Summary of Bubble Distribution Data, k = 0.100"

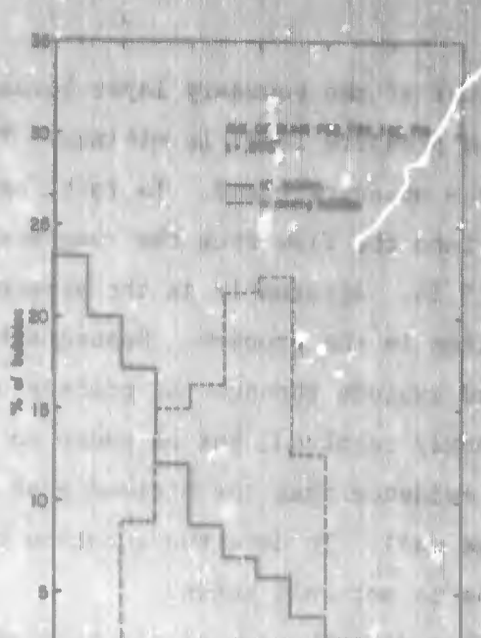

Figure 5.47: Summary of Bubble Distribution Data, k = 0.050"

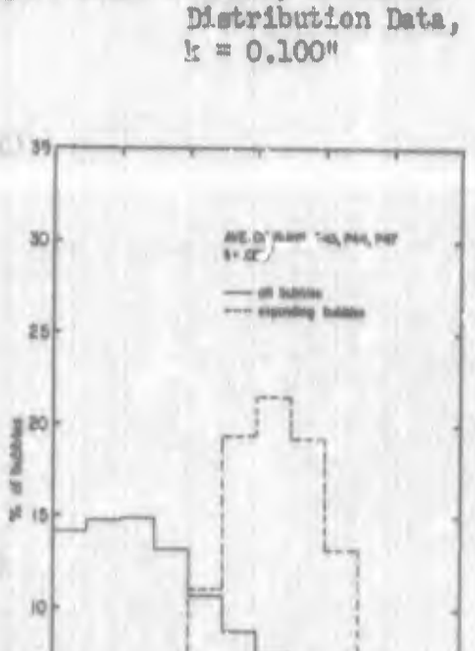

Figure 5.48: Summary of Bubble Distribution Data, k = 0.025"

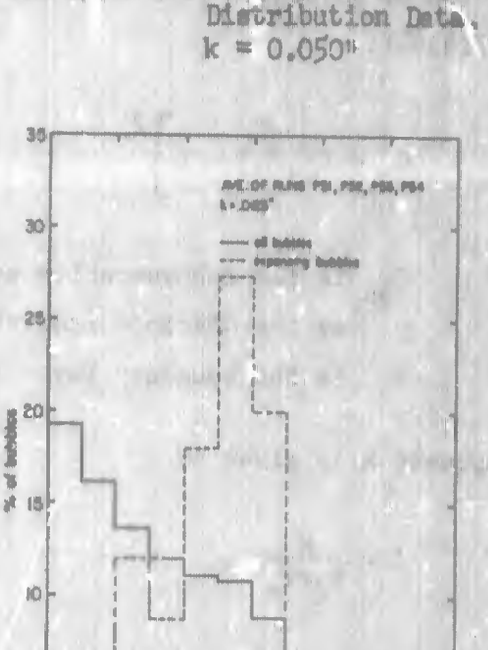

Figure 5.49: Summary of Bubble Distribution Data, k = 0.0125"

the center of the boundary layer because of a lack of nuclei near the wall where the mean pressure level is minimum. The observed bubble distributions indicate quite the opposite trend. In fact, on several occasions nuclei were observed to be fed into the flow from the roughness grooves. An example of this is shown in Figure 5.54. Apparently as the pressure is lowered, nuclei could form by gaseous cavitation in the grooves. Subsequently, these nuclei would be carried into the flow and explode through the process of vaporous cavitation. This point is still not clearly resolved, but as shown in a subsequent section, there is fairly strong evidence that the minimum peak in the pressure fluctuations occurs away from the wall. To date the question of the distribution of static pressure fluctuations is not well known.

This distribution of all bubbles may be explained by the process of turbulent diffusion. This problem is analogous to the sediment transport phenomenon, where small particles are suspended by the turbulent velocity fluctuations. The concentration of suspended load in a uniform, turbulent shear flow is given by (cf Rouse [1938]):

$$C_o = C_{md}\left[\frac{\delta}{y} - 1\right]^Z \tag{5.40}$$

where C_{md} is the concentration at mid-depth
y is the distance from the boundary
δ is the boundary layer thickness

The exponent Z is given by

$$Z = \frac{\omega}{\beta_d \kappa u_*} \tag{5.41}$$

where ω is the fall velocity of the particle
κ is the Von Karman constant
β_d is the ratio between the mass diffusion coefficient and the eddy viscosity.

Equation 5.40 was derived originally for uniform flow in open channels. The distribution of shear stress is a linear relationship given by

$$\tau = \tau_o(1 - y/\delta) \tag{5.42}$$

where τ_o is the wall shear. A logarithmic velocity defect law is assumed as:

$$\frac{\bar{u} - U}{u_*} = \frac{2.3}{\kappa} \log \frac{y}{\delta} \tag{5.43}$$

which is valid throughout the velocity field. The well known mixing length theory was used to approximate the variation of eddy viscosity through the flow. These assumptions are not completely valid in a developing boundary layer. However, there is an analogy between the sediment transport problem and the bubble distribution noted in this investigation. In the latter case sediment tends to fall to the bottom due to gravity and the settling effect is offset by the action of turbulence. In the present situation, the problem is turned up side down, the tendency for bubbles to rise to the roof being offset by the turbulence. Using this analogy, the average bubble distributions were plotted on log-log paper in the form (%) versus (δ/y - 1). It was assumed that the percentage of bubbles was related to the concentration of bubbles. Thus, the exponent Z could be obtained from the slope of the best straight line through the data shown in Figures 5.50 through 5.53. Assuming β_d to be 1, κ to be 0.41 and using the measured value of u_*, the velocity of rise w was obtained using equation 5.41. The bubble diameter corresponding to this velocity of rise was obtained by approximating the bubble by a sphere acting under a force equal to the product of bubble volume and fluid density. The relation applied is presented in Figure 5.55, and as shown in Table 5.4, reasonable values for the bubble diameters occur. For each case the diameter is in good agreement with the average of bubble diameters observed in the flow.

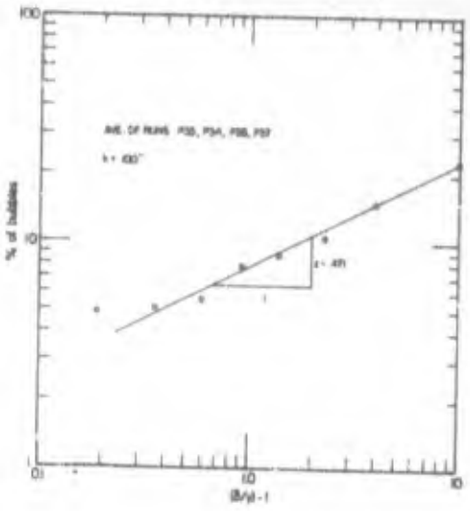

Figure 5.50: Determination of Bubble Rise Velocity from Distribution Data, k = 0.100"

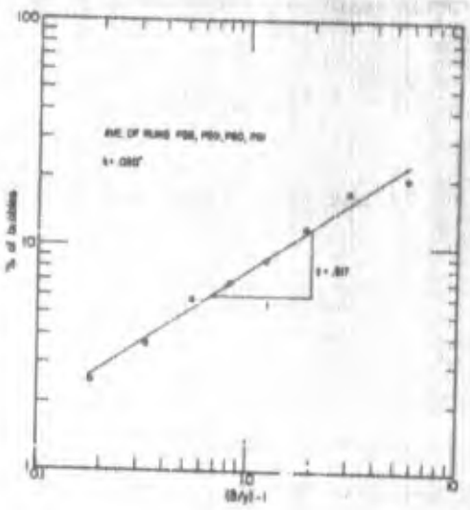

Figure 5.51: Determination of Bubble Rise Velocity from Distribution Data, k = 0.050"

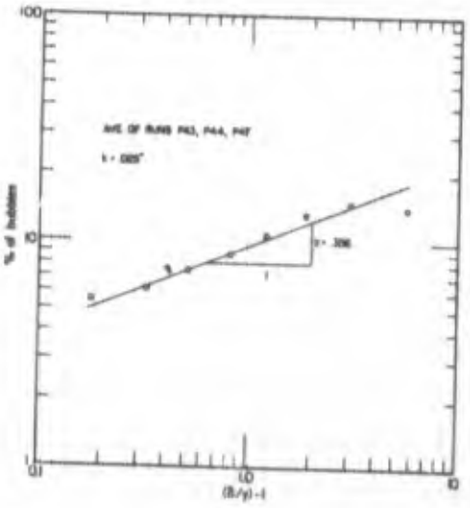

Figure 5.52: Determination of Bubble Rise Velocity from Distribution Data, k = 0.025"

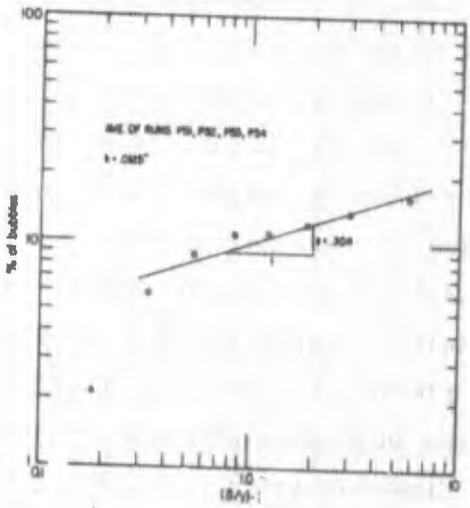

Figure 5.53: Determination of Bubble Rise Velocity from Distribution Data, k = 0.0125"

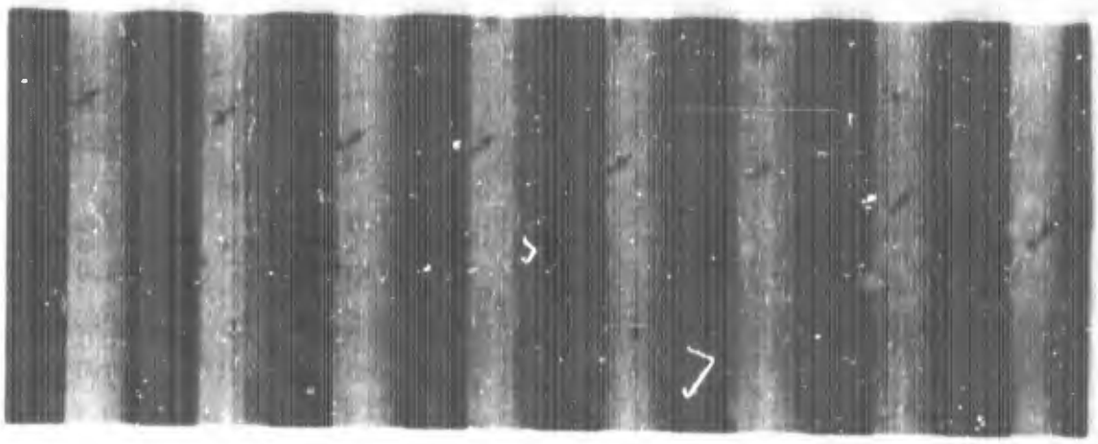

Figure 5.54: Example of Cavitation Nuclei Leaving Roughness Groove

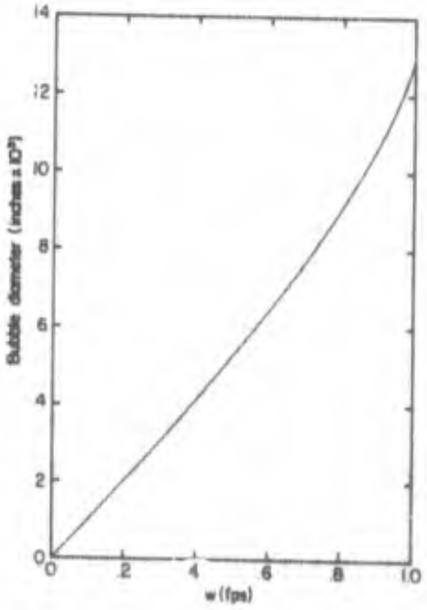

Figure 5.55: Bubble Diameter versus Rise Velocity

Table 5.4

Bubble Distribution Computations

k (inch)	Z	u_* (ft/sec)	u' (ft/sec)	d_b (inch)
.0125	0.304	2.42	0.402	0.0310
.025	0.336	2.18	0.300	0.0304
.050	0.617	3.12	0.789	0.0890
.100	0.471	2.96	0.571	0.0605

5.5 Cavitation Inception Data

Cavitation inception data for the four roughness patterns investigated are presented in Figure 5.56. The majority of these were collected in water with a gas content ranging from 0.14% to 0.28% by volume at NTP. Data for the 0.100" grooves were collected in water having a gas content ranging from 0.28% to 0.47%. The 0.100" results show a definite tendency to rise with a decrease in velocity. The flow is fully rough under these conditions and there is no reason to believe that there is a change in the relative turbulence level. In fact, the previously cited turbulence measurements indicated that the turbulence level was directly proportional to the free stream dynamic pressure. Hence, the indication is definite that this phenomenon is an effect of gas content.

The maximum gas content of 0.47% corresponds to a saturation pressure head of 7.9 ft; thus, from equation 3.29, there would be a scale effect given by $7.9/\frac{U^2}{2g}$. When the absolute pressure head was below 7.9 feet, this corresponds to a velocity of approximately 43.9 feet per second for the 0.100" roughness experiments. As shown in Figure 5.56, there is an upward trend in the data at velocities below 45 feet per second. The scale effect is not as large as predicted by equation 3.29. Theoretically, the increase in σ_i at 30 feet per second should be 0.5, whereas a maximum increase of 0.05 was noted in this experiments. It is very unlikely that the diffusion time in the minumum pressure zone is long enough for bubbles to grow completely by gaseous cavitation as is assumed in equations 3.29. Thus, there appears to be some effect of gas content in these experiments, but of a minor nature. The remaining data shown were obtained at

a lower gas content and indicate very little increase in σ_i with a reduction in velocity. For comparison the data obtained by Daily and Johnson for a smooth wall are also plotted in Figure 5.56 which give a much more obvious variation in σ_i with velocity. Some of this is due to the variation in relative turbulence. It is well known that the turbulence intensity is relatively higher for smooth walls at lower velocities. Thus, at lower velocities, the difference between the wall pressure and minimum pressures in the boundary layer is a correspondingly larger fraction of the free stream dynamic pressure, indicated by an increase in the cavitation index. At the same time the wall pressure required for cavitation in the test section with a smooth wall is even lower than for the rough wall experiments performed in this investigation. The saturation pressure in the Daily and Johnson experiments was of the same order of magnitude as in the present study. Therefore, a greater scale effect due to gas content can be expected in the smooth wall tests.

In comparing the effect of skin friction on cavitation inception, the minimum values of the cavitation index obtained at high velocity were compared with the corresponding values of the local skin friction coefficient in Figure 5.57. As predicted by equation 3.57, a linear relationship between cavitation index and skin friction coefficients is indicated, given by:

$$\sigma_i = 15.92\ C_f \approx 16\ C_f \tag{5.44}$$

For comparison, some data from Daily and Johnson are plotted also. The values of skin friction had to be estimated; and, hence, only a fair agreement could be expected. The important point to note is that relatively large differences exist between the mean wall pressure and the negative peak of the pressure fluctuations, which are predicted by equation 5.34. Both the bubble growth and bubble stability experiments previously cited, indicate that inception occurred at pressures very close to vapor pressure in this study. Therefore, σ_i is a direct indication of the difference between the wall pressure and the local pressure at the point of inception. This pressure level corresponds to some negative peak in the pressure fluctuations. The first question must be directed to the required duration of a pressure fluctuation for cavitation inception. Considering a bubble to be a

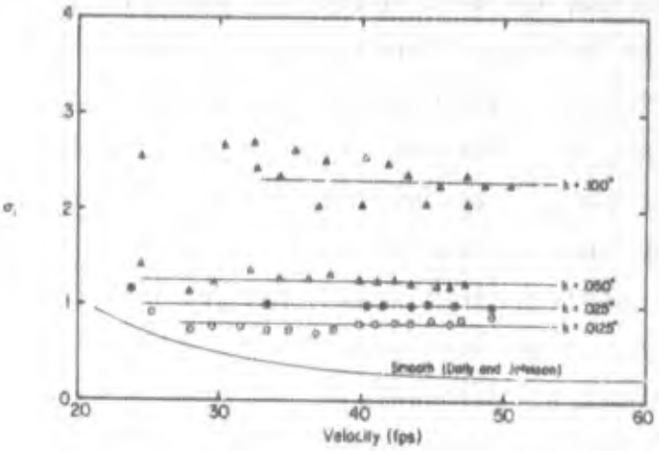

Figure 5.56: Cavitation Inception Data

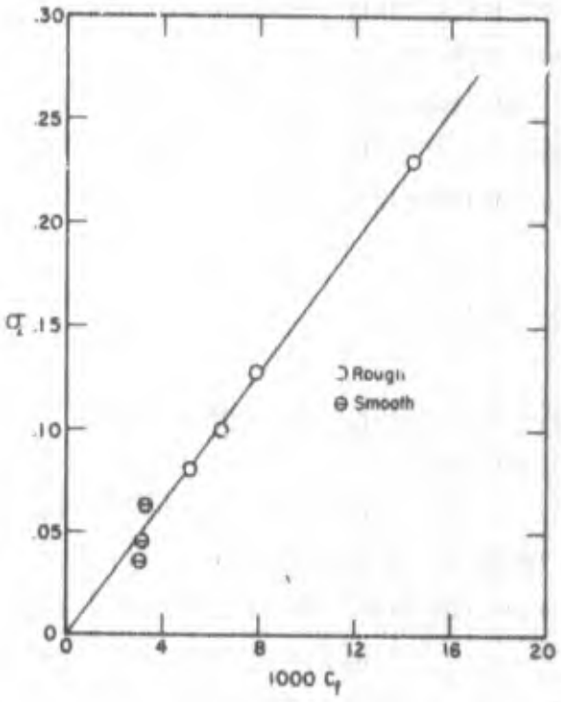

Figure 5.57: Boundary Layer Cavitation Law

simple, one degree of freedom, spring-mass system, a steady state response can be expected from a pulse having a duration equal to at lease one half of the natural period. Thus, in first approximation, pressure fluctuations with a frequency of less than twice the natural frequency of a nucleus can create cavitation. Minnaert (1933) has computed the natural frequency of an air bubble. He reported the relation

$$f_n = \frac{1}{2\pi r}\left(\frac{3\eta p_g}{\rho}\right)^{1/2} \tag{5.45}$$

where f_n = natural fequency in cps

r = mean radius of the bubble

p_g = internal gas pressure

ρ = mass density of water

η = ratio of specific heats

This relation was used to estimate the natural frequency of the nuclei, which were assumed to be filled with gas at a pressure equal to the vapor pressure. The result is

$$f_n = \frac{18.78}{r}$$

where r is in inches. Thus, a bubble having a radius of 0.01 inches has a natural frequency of 1,878 cps. Reported energy density spectra for wall pressure fluctuations indicate that practically all the energy in pressure fluctuation signals is contained at frequencies below 1,000 cps. It should be expected then, that the negative peak in the pressure fluctuations and not the mean pressure level will be the important factor in cavitation inception.

Assuming the negative peaks to occur less than 5% of the time, the magnitude of the peaks would be

$$p_{min} = 1.64\sqrt{\overline{p'^2}} \tag{5.46}$$

if the temporal variations follow a Gaussian distribution. Using the value of root mean square wall pressures reported by Willmarth and Wooldridge (1962):

$$\frac{\sqrt{\overline{p'^2}}}{\frac{1}{2}\rho U^2} = 2.19\ C_f \tag{5.47}$$

and assuming cavitation inception at vapor pressure the expected cavitation relation would be

$$\sigma_i = 3.59\ C_f$$

which is certainly in disagreement with the experimental results. In a private communication to Professor J.W. Daily, Willmarth quoted measurements of negative peaks in wall pressure as high as 4 times the root mean square value. This would correspond to the relation

$$\sigma_i = 8.76\ C_f$$

which is still in disagreement with the experimental results expressed by equation 5.44.

However, this cavitation law is not in disagreement with previous cavitation experiments. Rouse (1953) reported the results of inception studies in a water jet. He obtained the value

$$\sigma_i = 10\ \frac{\sqrt{\overline{p'^2}}}{\rho\frac{U_o^2}{2}}$$

where $\sqrt{\overline{p'^2}}$ is the maximum value of the pressure fluctuations

U_o is the maximum jet velocity

For comparison, the results of this study, using Willmarth and Wooldridge's (1962) wall pressure measurements, indicate a value given by

$$\sigma_i = 7.27 \frac{\sqrt{\overline{p'^2}}}{\rho \frac{U^2}{2}} \tag{5.48}$$

In the same paper Rouse (1953) reported the ratio

$$\frac{\sqrt{\overline{p'^2}}}{\rho \frac{\overline{u'^2}}{2}} = 2.15$$

At the observed point of inception ($y/\delta = 0.5$) in the boundary layer, the turbulence intensity was found to be

$$\rho \frac{\overline{u'^2}}{2} = 1.12\tau_o \tag{5.49}$$

Using the previously cited wall pressure measurements by Willmarth and Wooldridge and equation 5.49 the relation

$$\frac{\sqrt{\overline{p'^2}}}{\rho \frac{\overline{u'^2}}{2}} = 1.96 \tag{5.50}$$

was found for this study which is in good agreement with the result for a turbulent jet. Daily and Johnson estimated the relation between the cavitation index and the root mean square value of the pressure fluctuations for a smooth wall boundary layer from the turbulence intensity deduced from photographs of bubble motion in the flow. They used the Batchelor (1951) relation between pressure and velocity fluctuations:

$$\sqrt{\overline{p'^2}} = 0.583\rho\overline{u'^2}$$

to obtain the value

$$\frac{\sigma_i}{\sqrt{\overline{p'^2}}} \rho \frac{U^2}{2} = 5.5 \text{ to } 7.9$$

In summary, it appears that negative pressure peaks of a magnitude many times larger than the root mean square value are responsible for cavitation. If these peaks are estimated from wall pressure measurements and the temporal variations in pressure are assumed to follow a Gaussian distribution, the frequency of occurence is practically zero (i.e. zero to 4 decimal places). This is a ridiculous conclusion, indicating that the temporal variations are not quite Gaussian in nature and probably have larger negative peaks at the center of the boundary layer than at the wall.

For engineering purposes the interesting comparison lies in the difference of cavitation inception for an isolated irregularity and a distributed roughness. For example, the cavitation index for the 0.100 inch grooves was found to be 0.235, the relative roughness, k/δ, at the point of inception was 0.13. Holl (1959) cites a cavitation index of 0.82 for an isolated irregularity with a relative height, $k/\delta = 0.13$.

To illustrate this point, the cavitation performance of a smooth body is compared to that of the same body with a roughened surface. Substitution of equation 5.44 into equation 3.60 results in the relation

$$\frac{\sigma_i}{\bar{\sigma}_i} = 1 + 16\, C_f \frac{1 + \bar{\sigma}_i}{\bar{\sigma}_i} \tag{5.51}$$

where σ_i is the cavitation index of a rough body

$\bar{\sigma}_i$ is the cavitation index of an identical smooth body

Using equation 5.51 and C_f given by the Prandtl - Schlichting skin friction law, the increase in cavitation index for a hydrofoil having a $C_{pmin} = -0.5$ located 2 inches from the leading edge has been computed. This was done in order to compare directly with the example cited by Holl (1959) for an isolated irregularity. A comparison of the results is given in Table 5.5.

Table 5.5

Comparison of Cavitation Inception due to Isolated and Distributed Roughness, $\sigma_i = 0.5$

k (inches)	x/k	$C_f \times 10^3$	% Increase in σ_i Distributed	Isolated
0.001	2000	5.51	26.4	102
0.002	1000	6.50	31.2	135
0.004	500	7.43	35.6	201
0.008	250	8.71	41.8	270

The comparison is quite startling, and graphically illustrates the favorable interference effect of adjacent protuberances. Therefore, it may be concluded that if an isolated irregularity is unavoidable, for example, due to limitations on tolerances for the mating of parts, it may be advantageous to artificially roughen the entire surface upstream of the irregularity.

VI SUMMARY AND CONCLUSIONS

Measurements of wall shear, temporal mean velocity, turbulence intensity and of the cavitation inception index were made in boundary layers adjacent to both smooth and rough surfaces. High speed photography was used to observe the boundary layer flow under cavitating conditions. The distribution of cavitating and non-cavitating bubbles through the boundary layer, bubble growth rate and critical radius was determined from the photographs. Four rough surfaces were used in this study, each roughness pattern consisting of uniform triangular grooves transverse to the flow direction having roughness heights of 0.0125 inch, 0.025 inch, 0.050 inch and 0.100 inch, respectively. The free stream velocity ranged from 16 to 51 feet per second. The following conclusions were reached:

1. Cavitation inception in a turbulent boundary layer may be correlated with wall shear for both smooth and rough boundaries.

2. An isolated irregularity on a smooth surface is more susceptible to cavitation than a surface of distributed roughness of equivalent roughness height.

3. For all cases studied vaporous cavitation inception occurred in the center of the boundary layer. The frequency of occurrence of cavitating nuclei near the wall was very low. Gaseous cavitation was observed in the roughness grooves, and, occasionally, nuclei were seen to leave the roughness grooves.

4. The greatest concentration of non-cavitating bubbles existed close to the wall. For the particular case of cavitation on the roof of the test section, the observed bubble distributions agree essentially with the theory developed for the variation of concentration of sediment in a fully turbulent shear flow.

5. It could be inferred from observations of critical radius and bubble growth that the instantaneous local static pressure external to the nucleus at inception was very close to the vapor pressure of the liquid. Computations from bubble growth data resulted in tensions of only 1 to 2 feet of water.

6. Since the observed tension in the liquid was low, measurements of the wall pressure at cavitation inception were direct indications of the magnitude of negative peaks in static pressure. Based on root mean square values of static pressure at the wall made by others, these peaks correspond to a frequency of occurrence of zero to 4 decimal places, if a Gaussian distribution is assumed for temporal variations. It is suggested that the negative peaks do not follow

a Gaussian distribution and are greater in magnitude away from the wall.

7. Turbulence intensity in boundary layers adjacent to both smooth and rough walls is primarily a function of wall shear. Good correlation was found between turbulence measurements made with a hot wire in air by other investigators and the measurements made with the total head tube in water.

8. Wall shear measurements indicated a universal dependence on a Reynolds number based on displacement thickness and corrected for the effects of roughness and pressure gradient. In addition, it was established that the Prandtl - Schlichting resistance law for rough flat plates was a reasonable approximation to the data obtained in this study under varying degrees of favorable pressure gradient.

9. Temporal mean velocity measurements showed good agreement with the "law of the wall" for both smooth and rough walls. The experimental velocity defect laws resulting from smooth and rough boundaries under zero pressure gradients were identical and agreed with the results of previous investigators. All velocity profiles examined were shaped very similar to the equilibrium profiles examined by Clauser (1954).

10. The present study clearly illustrates the strong relation between cavitation inception and flow noise problems in a turbulent boundary layer. The need for a close investigation of temporal variations in static pressure away from the boundary in a turbulent shear flow is evident. Reliable pressure sensors for measurements within a turbulent shear flow need to be developed to answer the problem of fluctuations in static pressure more definitely. More information on temporal variations in pressure is required, along with further studies of cavitation inception near boundaries with three-dimensional roughness elements. This is of direct interest in the problem of cavitation inception, and of the related cavitation damage and is indirectly related to the effect of roughness on flow noise and vibration.

REFERENCES CITED

1. Abecasis, F. M., "Fluctuations of Pressure at a Flat Plate in Contact with a High Speed Flow", Paper #287, National Laboratory of Civil Engineering, Lisbon, 1966 (In French)

2. Ambrose, H. H., "The Effect of Surface Roughness on Velocity Distribution and Boundary Resistance", Department of Civil Engineering, University of Tennessee, Final Report, Contract Nonr 811(03) 1956.

3. Batchelor, G. K., "Pressure Fluctuations in Isotropic Turbulence", Proc. Camb. Phil. Soc., 47, Part 2, April 1951, P. 369.

4. Benson, B. W., "Cavitation Inception on Three Dimensional Roughness Elements", David Taylor Model Basin, Report 2104, May 1966

5. Benson, D. B., "The Influence of Roughness on the Inception of Cavitation", M.I.T. S. M. Thesis, 1958.

6. Bull, M. K., Wilby, J. F., and Blackman, D. R., "Wall Pressure Fluctuations in Boundary Layer Flow and Response of Simple Structures to Random Pressure Fields", Univ. of Southhampton Final Report, Contract No. AF61(052)-358, July 1963.

7. Burril, F., "Sir Charles Parsons and Cavitation", Trans. Inst. of Marine Engineers, Vol. 63, No. 8, 1951

8. Calehuff, G. L., and Wislicenus, G. F., "ORL Investigations of Scale Effects on Hydrofoil Cavitation", Ordnance Research Laboratory, Penn. State Univ. TM 19.4212-03, February 1956.

9. Carper, H. J., Heilbacker, J. K. and Logan, E., "The Effect of a Change in Wall Roughness on Turbulence Intensity and Shear Stress Distribution in a Two-Dimensional Channel Flow", Developments in Mechanics, Permagon Press, New York, 1965.

10. Clauser, F. H., "The Turbulent Boundary Layer", Advances in Applied Mechanics 4, pp. 1 - 51, Academic Press, 1956.

11. Clauser, F. H., "Turbulent Boundary Layers in Adverse Pressure Gradients", Jour. Aeronaut. Sci., 21, 1954, pp. 91 - 108.

12. Coles, D., "The Law of the Wake in the Turbulent Boundary Layer", J. Fluid Mech. 1, Part 2, 1956, pp. 191/226.

13. Colgate, D., "Cavitation Damage of Roughened Concrete Surfaces", Proc. A.S.C.E. Paper 2241, 85, HY11, October 1959.

14. Corrsin, S., and Kistler, A. L., "Free Stream Boundaries of Turbulent Flows", NACA Report 1244, 1955.

15. Daily, J. W. and Johnson, V. E., "Turbulence and Boundary Layer Effects on the Inception of Cavitation from Gas Nuclei", M.I.T., Hydrodynamics Laboratory Report No. 21, July 1955.

16. Daily, J. W., and Johnson, V. E., "Turbulence and Boundary Layer Effects on Cavitation Inception from Gas Nuclei", Trans. A.S.M.E., Vol. 78, 1956, pp. 1695 - 1706.

17. Daily, J. W., Lin, J. D., and Broughton, R. S., "The Distribution of the Mean Static Pressure in Turbulent Boundary Layers in Relation to Inception of Cavitation", M.I.T. Hydrodynamics Laboratory Report No. 21, June 1959.

18. Eisenberg, P., "Effect of Small Errors in Body Shape and Angle on Pressure Distribution and Cavitation Limits", David Taylor Model Basin Report 792, October 1951.

19. Eisenberg, P., "Cavitation", International Sciences and Technology, February 1963.

20. Epstein, P. S., and Plesset, M. S., "On the Stability of Gas Bubbles in Liquid-Gas Solutions", Jour. of Chem. Phys. 18, No. 11, November 1950, pp. 1505/1509.

21. Fage, A., "Fluid Flow in Rough Pipes", Aero. Res. Council R. & M., 1585, 1933.

22. Graveto, V., "Correlations Between Turbulence Parameters and Mean Flow Characteristics in Fluid Flow", SM. Thesis, M.I.T., January 1967.

23. Hama, F. R., "Boundary Layer Characteristics for Smooth and Rough Surfaces", Trans. SNAME, 62, 1954.

24. Harvey, E. N., Mc Elroy, W. D., and Whiteley, A. H., "On Cavity Formation in Water", J. Appl. Physics 18, 1947, pp. 162/172.

25. Holl, J. W., "The Inception of Cavitation on Isolated Surface Irregularities", Journal of Basic Engineering, Trans. A.S.M.E., Paper No. 59-Hyd-12 1959.

26. Holl, J. W., and Wislicenus, G. F., "Scale Effects on Cavitation", Jour. Basic. Eng., Trans. A.S.M.E., Paper No. 60-WA-151, 1960.

27. Holl, J. W., "An Effect of Air Content on the Occurence of Cavitation", Jour. Basic Eng., Trans. A.S.M.E. 82, No. 4, November 1960.

28. Holl, J. W., and Treaster, A. L., "Cavitation Hysteresis", Jour. Basic Eng., Trans. A.S.M.E., March 1966, pp. 199/212.

29. Hsieh, D. H., and Plesset, M. S., "Theory of Rectified Diffusion of Mass into Gas Bubbles", Jour. Acoust. Soc. Am. 33, No. 2, February 1961.

30. Ippen, A. T., Tankin, R. S., and Raichlen, F., "Turbulence Measurements in Free Surface Flow with an Impact Tube - Transducer Combination", M.I.T. Hydrodynamics Laboratory Report No. 20, July 1955.

31. Johnson, V. E., and Eisenberg, P., "Environmental and Body Conditions Governing the Inception and Development of Natural and Ventilated Cavities", Eleventh International Towing Tank Conference, Japan, November 1966.

32. Karman, T., von, "Mechanishe Ahnlichkeit und Turbulenz", Proc. 3rd Intern. Congress Applied Mech., Stockholm, 1930, Available as NACA TM 611 (1931).

33. Kelvin, Lord, "On the Formation of Coreless Vortices by the Motion of a Solid Through on Inviscid Incompressible Fluid", Phil. Mag. 23 (1897), pp. 255 - 257.

34. Kermeen, R. W., McGraw, J. T., and Parkin, B. R., "Mechanism of Cavitation Inception and the Related Scale Effects Problem", Trans. A.S.M.E. 77, 1955 pp. 533/541.

35. Klebanoff, P. S., "Characteristics of Turbulence in a Boundary Layer with Zero Pressure Gradient", NACA Report No. 1247, 1955.

36. Knapp, R. T., and Hollander, A., "Laboratory Investigations of the Mechanism of Cavitation", Trans. A.S.M.E. 70, 1948, pp. 419/439.

37. Kraichen, R., "Pressure Fluctuations in Turbulent Flow Over a Flat Plate", J. Acoust. Soc. Am., 28, No. 3, May 1956.

38. Ibid, "Noise Transmission from Boundary Layer Pressure Fluctuations", J. Acoust. Soc. Am., 29, No. 1, January 1957.

39. Laufer, J., "Investigation of Turbulent Flow in a Two-Dimensional Channel", NACA Report No. 1053, 1951.

40. Laufer, J., "The Structure of Turbulence in Fully Developed Pipe Flow", NACA Report No. 1174. 1954.

41. Liu, C. K., Kline, S. J., and Johnston, J. P., "An Experimental Study of Turbulent Boundary Layer on Rough Walls", Report MD-15, Stanford University, July 1966.

42. Logan, E., and Jones, J. B., "Flow in a Pipe Following an Abrupt Increase in Surface Roughness", Jour. Basic Eng., Trans. A.S.M.E., March 1963, pp. 35/40.

43. Ludwieg, H., and Tillman, W., "Untersuchungen über die Wandshubspannung in Turbulenten Reibungsschichten", Ing.-Arch. 17, 1949, pp. 288/299. Available as NACA T.M. No. 1285, 1950.

44. MacMillan, F. A., "Experiments on Pitot Tubes in Shear Flow", Aeronautical Research Council Technical Report, R. & M. No. 3028, 1957.

45. Maestrello, L., "Measurement and Analysis of the Response Field of Turbulent Boundary Layer Excited Panels", J. Sound Vib. 2, No. 3, 1965, pp. 270/292.

46. McNulty, P. J.. "The MERL Gas Content Apparatus", National Engineering Laboratory Report No. 41, June 1962.

47. Millikan, C., "A Critical Discussion of Turbulent Flows in Channels and Circular Tubes", Proc. 5th Int. Cong. Appl. Mech., Cambridge, Mass. 1938.

48. Minnaert, M., "On Musical Air Bubbles and the Sounds of Running Water", Phil. Mag., Ser. 7, Vol. 16, 104, August 1933, pp. 235 - 248.

49. Moore, W. F., "An Experimental Investigation of the Boundary Layer Development Along a Rough Surface", Ph.D. Dissertation, State University of Iowa, 1951.

50. Nikuradse, J., "Widerstandsgesetz und Geschwindigheitsverteilung von turbulenten Wasserströmung in glatten und rauhen Rohren, Proc. 3rd Int. Cong. Appl. Mech., Stockholm, 1930, pp. 239/248.

51. Nikuradse, J., "Stromungsgesetze in rauhen Rohren", VDI - Forschungsheft 361, 1933. Available as NACA T.M. 1292, 1950.

52. Numachi, F., Oba, R., and Chida, I., "Effects of Surface Roughness on Cavitation Performance of Hydrofoils - Report 1", Jour. Basic Eng. Trans. A.S.M.E. 87, 1965a, pp. 495/503.

53. Ibid, "-------Report 2", Symposium on Cavitation in Fluid Machinery, Winter Annual Meeting, A.S.M.E., November 1965b, pp. 16 - 31.

54. Numachi, F., "------Report 3", Jour. Basic Eng., Trans. A.S.M.E., Paper No. 66 - WA/FE-26, November 1966.

55. Oshima, R., "Theory of Scale Effects on Cavitation Inception on Axially Symmetric Bodies", Jour. Basic Eng. Trans. A.S.M.E., Paper No. 60 - WA-136, 1960.

56. Perkins, F. E., and Eagleson, P. S., "The Development of a Total Head Tube for High Frequency Pressure Fluctuations in Water", M.I.T. Hydrodynamics Laboratory T. N. No. 5, July 1959.

57. Perry, A. E. and Joubert, P. N., "Rough Wall Boundary Layers in Adverse Pressure Gradients", J. Fluid Mech., 17, part 2, October 1963, pp. 193/211.

58. Plesset, M., and Shaffer, P., "Cavity Drag in Two and Three Dimensions", Journal of Appl. Phys., Vol. 19, October 1948.

59. Plesset, M. S., "The Dynamics of Cavitation Bubbles",Jour. of Appl. Mech. 16, 1949, pp. 277 - 282.

60. Plesset, M. S., and Zwick, S. A., "The Growth of Vapor Bubbles in Superheated Liquids", Jour. of Appl. Phys. 25, No. 4, April 1954, pp. 493/500.

61. Plesset, M. S., and Hsieh, D. Y., "Theory of Gas Bubble Dynamics in Oscillating Pressure Fields", Physics of Fluids 3, No. 6, December 1960

62. Plesset, M. S., "Bubble Dynamics", Proc. of Symp. on Cavitation in Real Fluids, General Motors Research Laboratories, Warren, Michigan, 1964.

63. Prandtl, L., "Uber die ausgebildete Turbulez", ZAMM 5, 136, (1925) and Proc. 2nd Intern. Congr. Appl. Mech., Zurich, 1926.

64. Prandtl, L., and Schlichting, H., "Das Widerstandsgesetz rauher Platlen", Werft, Reederei, Hafen 1 - 4, 1934.

65. Preston, J., "The Determination of Turbulent Skin Friction by Means of Pitot Tubes", J. Royal Aero. Soc. 58, 1954, pp. 109/121.

66. Rayleigh, Lord, "On the Pressure Developed in a Liquid During the Collapse of a Spherical Cavity", Phil. Mag., 34, 1917, pp. 94 - 98

67. Reichardt, H., "The Laws of Cavitation Bubbles at Axially Symmetrical Bodies in a Flow", Report U.M. 6628, MAP Volkenrode, October 1945. Available in English as Reports and Translations Number 766, Ministry of Aircraft Production (Great Britain). August 1946.

68. Reynolds, O., "Papers on Mechanical and Physical Subjects", Vol. 2, p. 578, 1901.

69. Ripkin, J. F., and Olsen, R., "A Study of the Influence of Gas Nuclei on Cavitation Scale Effects in Water Tunnel Tests", Univ. of Minn. St. Anthony Falls Hydraulic Lab. Report 58, February 1958.

70. Ripkin, J. F., "The Influence of Free Gas Content on the Inception of Cavitation on a 1.5 Caliber Ogive Mounted in a Closed Jet Water Tunnel", Univ. of Minn. St. Anthony Falls Hydraulic Lab. Advance Report, 1959.

71. Robertson, J. M., McGinley, J. H., and Holl, J. W., "On Several Laws of Cavitation Scaling", La Houille Blanche, No. 4, September 1957.

72. Robertson, J. M., and Martin, J. D., "Turbulence Structure Near Rough Surfaces", AIAA Journal 4, No. 4, December 1966, pp. 2242/2245.

73. Rotta, J., "Uber die Theorie der Turbulenten Grenzschicten", Mitteilungen aus dem Max-Planck-Institut fur Strömungsforschung (Göttingen), No. 1, 1950. Available as NACA T.M. 1344, 1953.

74. Rouse, H., Fluid Mechanics for Hydraulic Engineers, McGraw-Hill, New York 1938.

75. Rouse, H., "Cavitation in the Mixing Zone of a Submerged Jet", La Houille Blanche, February 1953.

76. Rundstadler, P. W., Kline, S. J., and Reynolds, W. C., "An Investigation of the Flow Structure of the Turbulent Boundary Layer", Report MD-8, Thermosciences Div., Stanford University, 1963.

77. Sams, K. W., "Experimental Investigations of Average Heat Transfer and Friction Coefficients for Air Flowing in Circular Tubes having Square-Threads Type Roughness", NACA Res. Mem. RME 52017, (1952).

78. Schlichting, H., Boundary Layer Theory, McGraw-Hill, New York, New York, 1960.

79. Schlichting, H., "Experimentelle Untersuchungen zum Rauhigkeitsproblem", Ing. Arch. 7, 1936, pp. 1/34. Available as NACA TM. 823, 1937.

80. Shalnev, K. K., "Cavitation due to Factors in a Slot", Eng. Mag., Vol. 8, Inst. of Mech., Acad. of Sci., U.S.S.R., 1950, pp. 3/39.

81. Ibid., "Cavitation of Surface Roughness", Jour. Theoret. Phys. (U.S.S.R.), Vol.21, No. 2, 1951, pp. 206 - 220. Available as DTMB Translation 259, December 1955.

82. Strasberg, M., "Measurements of the Fluctuating Static and Total-Head Pressures in a Turbulent Wake", David Taylor Model Basin Report 1779, 1963.

83. Strasberg, M., "Influence of Air-Filled Nuclei on Cavitation Inception", David Taylor Model Basin Report 1078, May 1957.

84. Streeter, V., and Chu, F., "Fluid Flow and Heat Transfer in Artificially Roughened Pipes", Final Report Project 4918, Armour Research Foundation, 1949.

85. Taylor, G. I., "The Mean Value of the Fluctuations in Pressure and Pressure Gradient in a Turbulent Fluid", Proc. Cambridge, Phil. Soc., 1936, pp. 380/384.

86. Tillman, W., "Untersuchungen über Besonderheiten bei turbulenten Reibungschichten an Platten", Kaiser-Wilhelm Institut für Strömungsforschung UM 6627, Gottingen, 1945. (See Rotta 1950).

87. Tulin, M. P. and Burkart, M. P., Linearized Theory for Flows about Lifting Foils at Zero Cavitation Number", David Taylor Model Basin Report C-638, February 1955.

88. Wooldridge, C. E. and Willmarth, W. W., "Measurements of the Correlation Between the Fluctuating Velocities and Fluctuating Wall Pressure in a Thick Turbulent Boundary Layer", University of Michigan Report 02920-2-T, 1962.

89. Willmarth, W. W., and Wooldridge, C. E., "Measurements of the Fluctuating Pressure at the Wall Beneath a Thick Turbulent Boundary Layer", J. Fluid Mech. 14, 1962.

90. Ibid., "Measurements of the Correlation Between the Fluctuating Velocities and the Fluctuating Wall Pressure in a Thick Turbulent Boundary Layer", AGARD Report 456, April 1963.

APPENDIX A

THE PRESTON TUBE FOR THE DETERMINATION OF WALL SHEAR

Consider a round total head tube of diameter d resting upon a smooth plane surface as shown in Figure A.1:

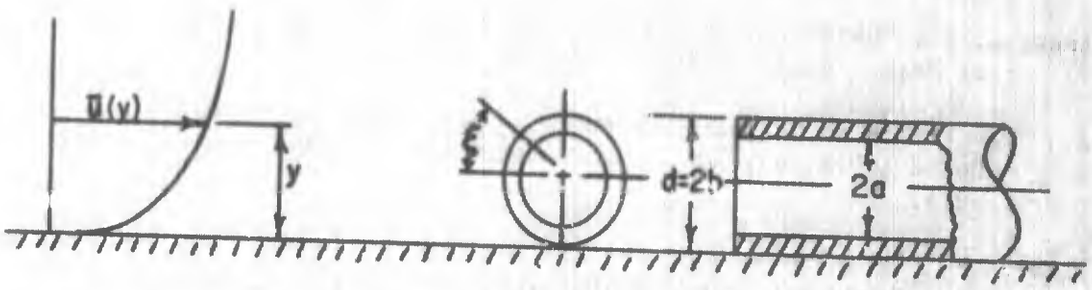

Figure A.1 Schematic Representation of Preston Tube

The total pressure sensed by such a tube is an average value which depends on the shape of the velocity profile and on the shape of the tube itself. For tubes much larger than the thickness of the laminar sub-layer, a velocity profile of the form

$$\frac{\bar{u}}{u_*} = C\left(\frac{u_* y}{\nu}\right)^{1/7} \tag{A.1}$$

may be assumed. The difference between the total pressure sensed by the tube and the static wall pressure is given by the integral of the dynamic pressure over the internal cross sectional area of the tube:

$$\Delta p = \frac{\rho}{2\pi a^2} \int_A \bar{u}^2 \, dA \tag{A.2}$$

where $\bar{u}$ is the local velocity

A is the cross sectional area

For a round tube:

$$dA = 2\sqrt{a^2 - (b - y)^2}\, dy \tag{A.3}$$

where 2b is the outside diameter

2a is the internal diameter

or noting the geometric identity:

$$y - b = a \sin \xi \tag{A.4}$$

where ξ is measured as shown in Figure A.1.

Hence

$$dA = 2a^2 \cos^2 \xi \, d\xi \tag{A.5}$$

Substitution of A.4, A.5, and A.1 into A.2 results in the expression

$$\Delta p = \frac{\rho}{\pi} C^2 u_*^2 \left(\frac{u_* b}{\nu}\right)^{2/7} I\left(\frac{a}{b}\right) \tag{A.6}$$

where

$$I\left(\frac{a}{b}\right) = \int_{-\pi/2}^{\pi/2} \left(1 + \frac{a}{b} \sin \xi\right)^{2/7} \cos^2 \xi \, d\xi \tag{A.7}$$

Since $d = 2b$, and defining

$$C_1 = \left[\frac{\pi C^2}{I\left(\frac{a}{b}\right)}\right]^{7/8} \tag{A.8}$$

Equation A.6 may be rewritten in the form

$$u_* = \frac{C_1^{1/2}}{2^{5/16}} \sqrt{\frac{2\Delta p}{\rho}} \Big/ \left(\sqrt{\frac{2\Delta p}{\rho}} \, \frac{d}{\nu}\right)^{1/8} \tag{A.9}$$

It is easily shown that Equation A.9 is equivalent to Preston's (1954) calibration equation in the form

$$\log \frac{\tau_o d^2}{4\rho\nu^2} = \log C_1 + \frac{7}{8} \log \frac{\Delta p d^2}{4\rho\nu^2} \tag{A.10}$$

Using Preston's result $\log C_1 = -1.392$, Equation A.9 reduces to the form used in the computer program:

$$u_* = 0.1622 \, \frac{\sqrt{\frac{2\Delta p}{\rho}}}{\left(\sqrt{\frac{2\Delta p}{\rho}} \, \frac{d}{\nu}\right)^{1/8}} \tag{A.11}$$

A similar result may be derived for a flattened probe, by assuming the probe to be two dimensional (infinite aspect ratio). For this case

$$\Delta p = \frac{\rho}{4a} \int_{b-a}^{b+a} \bar{u}^2 \, dy \qquad (A.12)$$

where $2b$ is the external probe thickness

$b - a$ is the wall thickness

Again employing the power law as the universal law of the wall

$$\frac{\bar{u}}{u_*} = C \left(\frac{u_* y}{\nu} \right)^{1/7} \qquad (A.13)$$

in Equation (A.12):

$$\Delta p = \frac{\rho}{2} C^2 u_*^2 \left(\frac{u_* b}{\nu} \right)^{2/7} I\left(\frac{a}{b}\right) \qquad (A.14)$$

where

$$I\left(\frac{a}{b}\right) = \frac{b}{a} \int_{1-\frac{a}{b}}^{1+\frac{a}{b}} \eta^{2/7} \, d\eta \qquad (A.15)$$

Rearranging Equation A.14 results in:

$$u_* = 1.090 \left[\frac{1}{I\left(\frac{a}{b}\right) C^2} \right]^{7/16} \frac{\sqrt{\frac{2\Delta p}{\rho}}}{\left[\sqrt{\frac{2\Delta p}{\rho}} \frac{d}{\nu} \right]^{1/8}} \qquad (A.16)$$

wherein $d = 2b$

In the present study a probe was fabricated from 0.120" OD tubing which has a flattened tip .035" thick. For this case

$2b = 0.035$ inch

$2a = 0.009$ inch

so that $\frac{a}{b} = 0.257$

$$I\left(\frac{a}{b}\right) = 2.000$$

Using C = 8.61 Equation A.16 reduces to

$$u_* = 0.1222 \frac{\sqrt{\frac{2\Delta p}{\rho}}}{\left[\sqrt{\frac{2\Delta p}{\rho}} \frac{d}{\nu}\right]^{1/8}}$$

This particular probe was calibrated using a round tube as standard. The variation of wall shear stress with flow rate was determined with the smooth roof installed in the test section using a 0.022 inch OD probe and Equation A.11. The results are plotted in Figure A.2 in terms of shear velocity versus nozzle reading. The flattened tube was then calibrated using this curve as a standard, as given by Figure A.3. The variation with the parameter

$$\sqrt{\frac{2\Delta p}{\rho}} \frac{d}{\nu}$$

is as predicted. However the experimentally determined constant is 0.1757 which differs radically from the theoretical value of 0.1222 suggesting that three dimensional effects are important.

Attempts were made to extend the Preston tube technique to the rough wall experiments. Following the same type of development as cited above, it was found that the results, both theoretically and experimentally were very sensitive to the location of the probe relative to the datum. A reliable calibration curve in terms of probe diameter to roughness height could not be achieved in this study. Therefore this technique was discarded for the determination of rough wall shear.

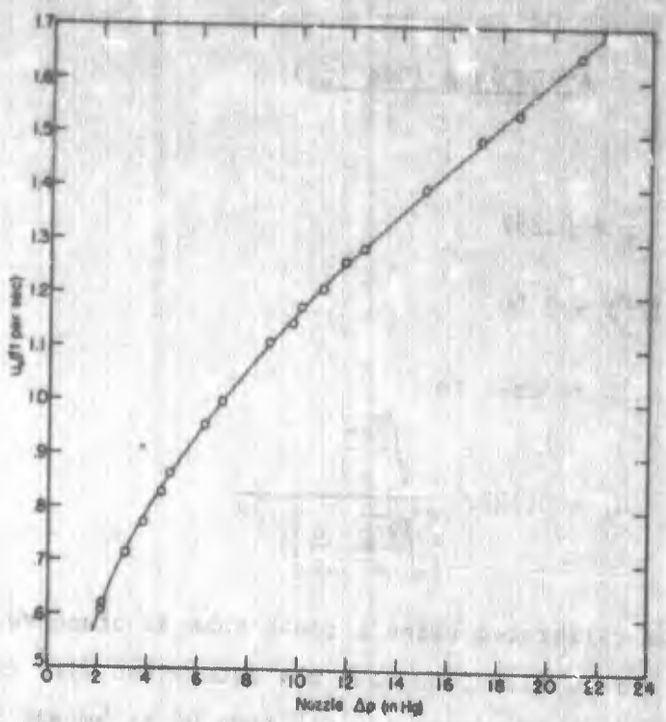

Figure A.2: Variation of Smooth Wall Friction with Flow Rate

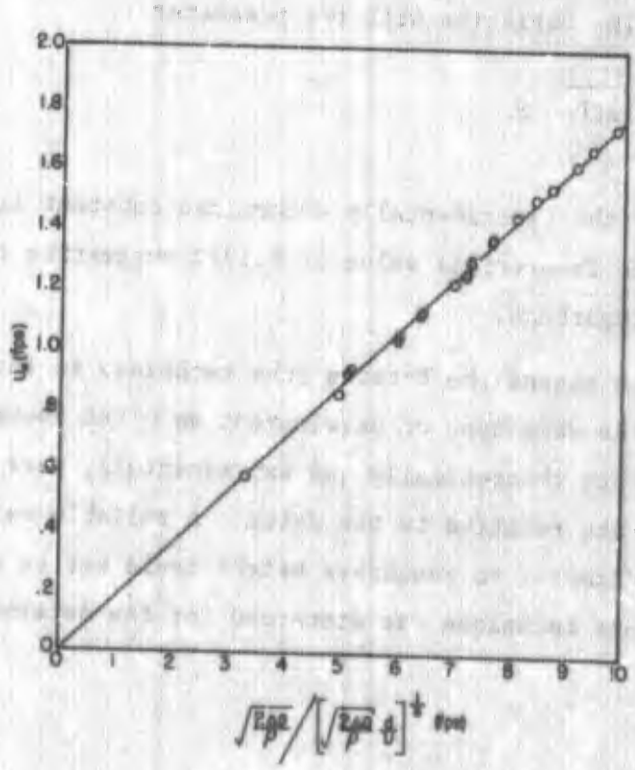

Figure A.3: Calibration Curve for Flattened Preston Tube

APPENDIX B

DISCUSSION OF POSSIBLE ERRORS IN THE DETERMINATION OF TEMPORAL MEAN AND FLUCTUATING VELOCITIES WITH A TOTAL HEAD TUBE

A critical discussion of the errors inherent in the determination of both mean and fluctuating components of velocity with a total head tube is given by Ippen et. al., (1955) and Perkins and Eagleson (1959). For the sake of completeness a brief review is presented here.

To estimate the errors inherent in the use of a total head tube, the Bernoulli equation is assumed to apply. The total pressure sensed by the tube is then:

$$p_t = \frac{\rho}{2} (\bar{u} + u')^2 + \bar{p} + p' \tag{B.1}$$

where $\bar{u}$ is the temporal mean velocity

u' is the fluctuating component of velocity

$\bar{p}$ is the mean static pressure

p' is the fluctuating pressure component

Expanding equation B.1 and taking the time average results in the following

$$p_t - \bar{p} = \frac{\rho}{2} \bar{u}^2 + \frac{\rho}{2} \overline{u'^2} \tag{B.2}$$

The accepted equation

$$\bar{u} = \sqrt{\frac{2}{\rho} \left(\bar{p}_t - \bar{p} \right)} \tag{B.3}$$

is incorrect by a factor which depends on the turbulence intensity. By taking the square root of equation B.2 and expanding the right-hand side using the binomial theorem, the following is obtained:

$$\sqrt{\frac{2}{\rho} \left(\bar{p}_t - \bar{p} \right)} = \bar{u} + \frac{1}{2} \frac{\overline{u'^2}}{\bar{u}} + \text{h.o. terms} \tag{B.4}$$

Thus, the error in equation B.3 is given by

$$\text{Error} \simeq + \frac{1}{2} \frac{\overline{u'^2}}{\bar{u}^2} \tag{B.5}$$

For $\sqrt{\overline{u'^2}}/\bar{u} < 0.1$ this error amounts to 1/2%.

An equation for the determination of root mean square turbulence intensity is obtained by expanding equation B.1:

$$p_t = \frac{\rho}{2} \bar{u}^2 + \rho \bar{u} u' + \frac{\rho}{2} u'^2 + \bar{p} + p' \tag{B.6}$$

By neglecting p' in equation B.6 and defining

$$p_t' = p_t - \bar{p}_t \tag{B.7}$$

where

$$\bar{p}_t = \frac{\rho}{2} \bar{u}^2 + \frac{\rho}{2} \overline{u'^2} + \bar{p} \tag{B.8}$$

and also neglecting u' compared to $\bar{u}$:

$$\sqrt{\overline{p_t'^2}} = \rho \bar{u} \sqrt{\overline{u'^2}} \tag{B.9}$$

Equation B.9 was used in this study to obtain values of the turbulence intensity. An estimate of the error in equation B.9 is obtained by subtracting equation B.8 from B.6, squaring the result and taking the mean square value:

$$\sqrt{\overline{p'^2}} = \left[\overline{\left(\rho \bar{u} u' + \frac{\rho}{2} u'^2 - \frac{\rho}{2} \overline{u'^2} + p' \right)^2} \right]^{1/2} \tag{B.10}$$

Expanding B.10 results in

$$\sqrt{\overline{p'^2}} = \rho\bar{u}\sqrt{\overline{u'^2}}\left[1 + \frac{\overline{u'^4}}{4\bar{u}^2\,\overline{u'^2}} - \frac{\left(\overline{u'^2}\right)^2}{4\bar{u}^2\,\overline{u'^2}}\right.$$

$$\left. + 2\frac{\overline{u'p'}}{\rho\bar{u}\,\overline{u'^2}} + \frac{\overline{u'^2p'}}{\rho\bar{u}^2\,\overline{u'^2}} + \frac{\overline{p'^2}}{\rho^2\bar{u}^2\,\overline{u'^2}} + \frac{\overline{u'^3}}{\bar{u}\,\overline{u'^2}}\right]^{1/2} \qquad (B.11)$$

For a symmetrical distribution of u', $\overline{u'^3}$ is zero. Further, assuming the following orders of magnitude:

$$\sqrt{\overline{u'^2}} \leq 0.1\,\bar{u}$$

and $$\overline{p'u'} \leq \frac{\rho}{2}\left(\overline{u'^2}\right)^{3/2}$$

the terms in equation B.11 may be estimated:

$$\frac{\overline{u'^4}}{4\bar{u}^2\,\overline{u'^2}} \leq 0.10 \qquad \frac{\left(\overline{u'^2}\right)^2}{4\bar{u}^2\,\overline{u'^2}} \leq 0.0025$$

$$\frac{2\overline{u'p'}}{\rho\bar{u}\,\overline{u'^2}} \leq 0.10 \qquad \frac{\overline{u'^2\,p'}}{\rho\bar{u}^2\,\overline{u'^2}} < 0.0050$$

$$\frac{\overline{p'^2}}{\rho^2\bar{u}^2\,\overline{u'^2}} \leq 0.0025$$

Thus, the error in equation B.9 is approximately 5% or less.

APPENDIX C

DESCRIPTION OF TECHNIQUE FOR CALIBRATING MEAN VELOCITY PROBES

The miniature wind tunnel used to calibrate the velocity probes is shown in Figure (C.1). Essentially, the apparatus consists of a contraction, a cylindrical test section, another contraction and a diffuser section. The tunnel is connected to the suction side of a blower rated at 50 cubic feet per minute at 20.8 inches of water. Throttling of the flow is achieved with a globe valve located at the compressor discharge. The inlet nozzle, through which the flow accelerates from the atmosphere into the test section, has the same variation in cross-sectional area as the efflux from a sharp edged orifice. The diameter of the test section is greater than the nozzle, allowing a free jet. The probes are placed in position along the centerline of the tunnel such that the tip is in line with four static pressure taps in the test section.

Isentropic flow is assumed from the atmosphere into the test section. Thus, the total pressure in the test section, p_t, is equal to the atmospheric pressure p_o. The incompressible pressure coefficient is defined as

$$C_p = \frac{\Delta p}{\rho U^2/2} \qquad (C.1)$$

where Δp is the difference between the total pressure sensed by the probe and the static pressure

$\rho U^2/2$ is the dynamic pressure

Neglecting compressibility effects on the pressure coefficient, the difference between the total pressure sensed by the probe and the static pressure is given by

$$\Delta p = C_p(p_t - p) \qquad (C.2)$$

where p_t is the true total pressure

p is the static pressure

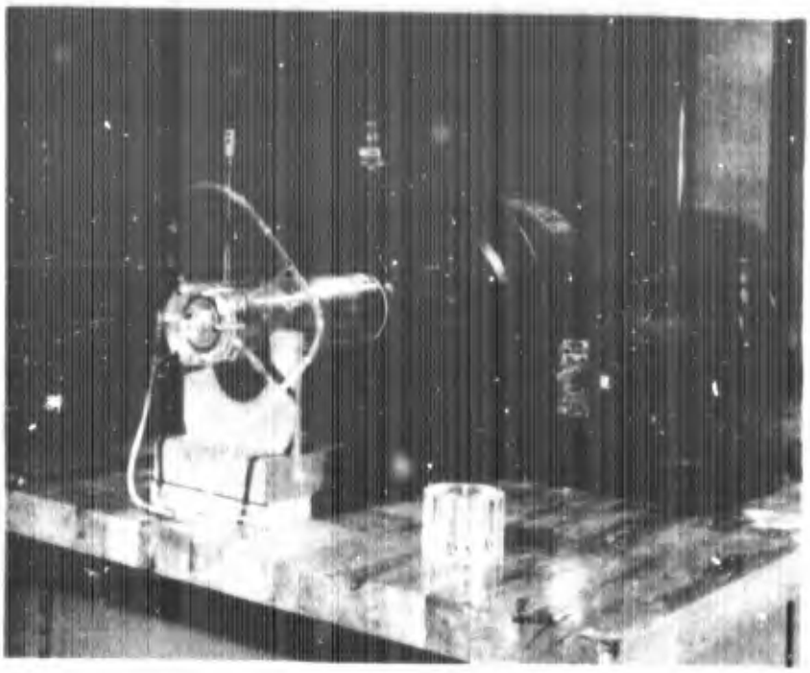

Figure C.1: View of the Probe Calibration Tunnel

Since, $P_t = P_o$ the following is true

$$C_p = \frac{\Delta p}{P_o - P} \tag{C.3}$$

Thus, the probe calibration is determined from the ratio of pressure difference between the probe and the static taps and the pressure difference between the atmosphere and the static taps. Compressibility is neglected only in terms of the calibration constant itself. The maximum Mach number was approximately 0.22 so that this assumption is valid.

APPENDIX D

DESIGN EQUATION FOR THE TURBULENCE GAGE

For an analysis of the response of a total head tube-transducer combination it is useful to consider the apparatus as a one degree of freedom system as shown in Figure D.1:

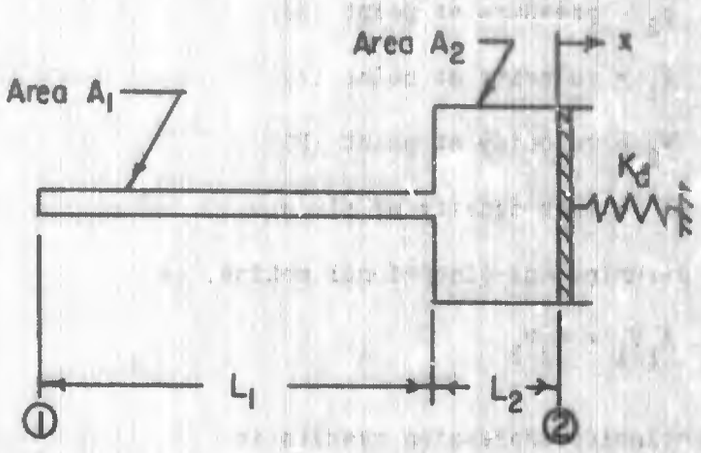

Figure D.1: Schematic Representation of Turbulence Probe

The spring constant, K_d, in Figure D.1 is a virtual quantity which represents the stiffness of a clamped circular membrane. The value of K_d is equal to force divided by the <u>average</u> deflection of the membrane. Using this definition, K_d is given by

$$K_d = \frac{192\pi}{r_d^2} \quad \frac{E_y t^3}{12(1 - \nu_p^2)} \qquad \text{(D.1)}$$

where

r_d is the radius of the membrane

ν_p is the Poisson's ratio

t is the membrane thickness

E_y is Young's modulus

The integral of the equation of motion is given by

$$P_1 + \rho \frac{V_1^2}{2} - P_2 = \rho \frac{V_2^2}{2} = \rho \int_1^2 \frac{\partial V}{\partial t} dx \qquad (D.2)$$

where

P_1 = pressure at point (1)

P_2 = pressure at point (2)

V_i = velocity at point (1)

V_2 = velocity at point (2)

ρ = mass density of fluid

The continuity equation, assuming one-dimensional motion, is

$$A_1 V_1 = A_2 V_2 \qquad (D.3)$$

Differentiation of the continuity expression results in

$$\frac{dV_1}{dt} = \frac{A_2}{A_1} \frac{d^2x}{dt^2} \qquad (D.4)$$

$$\frac{dV_2}{dt} = \frac{d^2x}{dt^2} \qquad (D.5)$$

Substitution of Equations D.3, D.4, and D.5 into Equation D.2 results in the expression

$$P_1 - P_2 + \frac{\rho}{2}\left[\left(\frac{A_2}{A_1}\right)^2 - 1\right]\left(\frac{dx}{dt}\right)^2 = \rho\left[\frac{A_2}{A_1} L_1 + L_2\right] \frac{d^2x}{dt^2} \qquad (D.6)$$

The membrane deflection, x, is related to the pressure difference, $P_1 - P_2$, by

$$P_1 - P_2 = -\frac{K_d x}{A_2} \qquad (D.7)$$

If Equation D.7 is substituted into Equation D.6 and the following approximations are made:

$$L_2 \ll \frac{A_2}{A_1} L_1$$

$$\left(\frac{dx}{dt}\right)^2 \approx 0$$

the equation of motion simplifies to

$$\frac{d^2x}{dt^2} + \frac{K_d}{\rho A_1 L_1}\left(\frac{A_1}{A_2}\right)^2 x = 0 \qquad \text{(D.8)}$$

The natural frequency of the system is obtained from the solution of Equation (D.8):

$$f_o = \frac{1}{2\pi}\sqrt{\frac{K_d}{\rho A_1 L_1}\left(\frac{A_1}{A_2}\right)^2} \qquad \text{(D.9)}$$

where f_o is in cycles per second.

When commercial transducers are used, Equation (D.9) is not in its most useful form since the only characteristic usually quoted by the manufacturer is the natural frequency in air, f_d, of the transducer. This natural frequency may be assumed equivalent to that of a clamped circular diaphragm:

$$f_d = \frac{10.21}{\pi}\sqrt{\frac{E_y t^3}{12(1-\nu_p^2)}\,\frac{1}{\rho_d t\, r_d^4}} \qquad \text{(D.10)}$$

where ρ_d is the mass density of the membrane material. Combining Equations D.1, D.9 and D.10 results in

$$f_o = 1.11\, f_d^{3/2} \left[\frac{\rho_d}{\rho}\,\frac{A_1}{L_1}\right]^{1/2} \left[\frac{\rho_d\,(1-\nu_p^2)}{E_y}\right]^{1/4} \qquad (D.11)$$

or for $\nu_p = 0.3$:

$$f_o = 1.09\, f_d^{3/2} \left[\frac{\rho_d}{\rho}\,\frac{A_1}{L_1}\right]^{1/2} \left[\frac{\rho_d}{E_y}\right]^{1/4} \qquad (D.12)$$

Equation D.12 was used to evaluate various transducer-total head tube combinations. The final form of the instrument package had the following characteristics:

$$f_d = 10{,}000 \text{ cps}$$

$$\frac{\rho_d}{\rho} = 7.83$$

$$\frac{A_1}{L_1} = 1.155 \times 10^{-3} \text{ inches}$$

$$E_y = 30 \times 10^6 \text{ psi}$$

where the transducer and total head tube were made of stainless steel. Using Equation (D.12) the theoretical natural frequency was found to be 240 cps, which is lower than the observed value of 320 cps.

APPENDIX E

SUMMARY OF MEASURED BOUNDARY LAYER PARAMETERS

Sta.	Run	k	δ	Δ	δ^*	θ	H	U	R_θ
		inches	inches	inches	inches	inches		fps	$\times 10^{-5}$
2	5	Smooth	0.122	0.481	.0190	.0141	1.346	35.32	0.418
2	6	"	0.106	0.433	.0169	.0123	1.374	49.89	0.461
4	14	"	0.252	1.272	.0416	.0305	1.364	49.89	1.137
4	15	"	0.248	1.222	.0409	.0298	1.372	41.37	0.913
5	21	"	0.299	1.292	.0453	.0344	1.320	40.21	1.079
6	7	"	0.331	1.416	.0516	.0387	1.332	34.09	0.962
6	8	"	0.323	1.379	.0488	.0368	1.324	48.03	1.361
6	9	"	0.344	1.588	.0521	.0388	1.343	47.28	1.435
6	10	"	0.337	1.479	.0549	.0408	1.346	19.64	0.551
6	11	"	0.340	1.585	.0547	.0406	1.347	32.24	0.940
6	12	"	0.348	1.583	.0537	.0402	1.336	38.59	1.176
6	13	"	0.344	1.639	.0562	.0412	1.363	27.11	0.807
3	57	.0125	0.278	1.244	.0669	.0412	1.624	41.11	1.027
4	56	"	0.389	1.645	.0832	.0544	1.528	39.63	1.372
5	55	"	0.487	1.986	.1005	.0668	1.504	40.78	1.759
6	52	"	0.545	2.229	.1074	.0727	1.478	47.34	2.341
6	53	"	0.543	2.209	.1070	.0726	1.474	40.18	1.927
6	54	"	0.521	2.164	.1043	.0702	1.485	23.99	1.074
2	48	.025	0.127	0.318	.0307	.0178	1.721	39.28	0.467
3	45	"	0.294	1.088	.0746	.0441	1.691	40.94	1.081
4	46	"	0.407	1.574	.0932	.0586	1.591	41.30	1.508
5	47	"	0.498	2.110	0.113	.0724	1.557	41.62	1.843
6	43	"	0.552	2.122	0.121	.0780	1.545	27.10	1.303
6	44	"	0.567	2.237	0.120	.0785	1.527	41.43	2.115
3	61	.050	0.345	1.260	.0967	.0538	1.799	41.73	1.255
4	60	"	0.467	1.804	0.121	.0702	1.726	41.34	1.678
5	59	"	0.586	2.267	0.144	.0862	1.673	42.40	2.150
6	58	"	0.640	2.411	0.159	.0951	1.676	42.86	2.369
3	27	.100	0.480	1.373	0.133	.0728	1.830	46.11	2.137
3	28	"	0.478	1.402	0.136	.0726	1.872	29.86	1.316
3	34	"	0.433	1.315	0.131	.0679	1.928	41.36	1.621
4	29	"	0.630	2.003	0.182	.0956	1.907	46.70	2.846
4	30	"	0.612	1.985	0.181	.0944	1.913	30.03	1.705
5	31	"	0.732	2.388	0.203	0.112	1.811	47.13	3.310
5	32	"	0.728	2.354	0.201	0.111	1.812	31.12	2.105
6	25	"	0.783	2.706	0.219	0.121	1.806	47.03	3.562
6	26	"	0.768	2.644	0.214	0.119	1.805	30.78	2.191
6	33	"	0.778	2.483	0.221	0.119	1.851	42.60	2.994

APPENDIX F

SUMMARY OF SKIN FRICTION DATA

Sta.	Run	k	k_s	$\frac{x}{k_s}$ (average value for k_s)	$\sqrt{\frac{C_f}{2}}$ Vel Prof	$\sqrt{\frac{C_f}{2}}$ Karman	$\sqrt{\frac{2}{C_f}}$ Vel Prof	$\frac{Y_2}{Y_1}$ R_{δ^*}
4	14	Smooth	Smooth		.0327		30.58	4.106×10^4
4	15	"	"		.0334		29.94	3.288
5	21	"	"		.0351		28.49	1.775
6	9	"	"		.0328		30.49	3.711
6	10	"	"		.0371		26.95	.9727
6	11	"	"		.0346		28.90	2.274
6	12	"	"		.0339		29.50	2.739
6	13	"	"		.0343		29.15	2.550
3	57	.010	0.012	950	.0538	.0547	18.59	257
4	56	.010	"	1317	.0506	.0532	19.76	461
5	55	.010	"	1675	.0506	.0525	19.76	484
6	54	.010	"	1871	.0482	.0462	20.75	660
6	53	.010	"	1871	.0482	.0462	20.75	713
6	52	.010	"	1871	.0482	.0462	20.75	669
2	48	.025	0.0275	182	.0968		10.33	
3	45	.022	"	415	.0686	.0606	14.58	648.8
4	46	.024	"	574	.0592	.0602	16.89	177.4
5	47	.023	"	731	.0534	.0554	18.73	316.4
5	43	.023	"	876	.0536	.0487	18.65	203.8
6	44	.023	"	916	.0568	.0487	17.61	332.1
3	61	.051	0.098	116	.0768	.0671	13.02	31.3
4	60	.055	"	161	.0672	.0672	14.88	69.1
5	59	.052	"	205	.0636	.0655	15.72	95.8
6	58	.052	"	279	.0661	.0627	15.13	84.0
3*	27	.102	0.359	31.8	.0970	.0908	10.31	11.35
3*	28	.102	"	31.8	.0970	.0908	10.31	11.05
4*	29	.110	"	44	.0910		10.99	
4*	30	.110	"	44	.0910		10.99	
5*	31	.107	"	56	.0852		11.74	19.82
5*	32	.107	"	56	.0852		11.74	19.38
6*	25	.111	"	62.5	.0809		12.36	25.7
6*	26	.111	"	62.5	.0809		12.36	25.5
3	34	.104	"	31.8	.0995		10.05	10.0
6	33	.101	"	62.5	.0889		10.05	16.35

* Protrusions

APPENDIX G

SUMMARY OF CAVITATION INCEPTION DATA

k	Velocity fps	σ_i	Gas Content %
0.0125	48.37	.0894	.193
"	47.04	.0875	"
"	46.27	.0818	"
"	44.87	.0845	"
"	43.53	.0826	"
"	42.43	.0821	"
"	41.05	.0796	"
"	39.76	.0796	"
"	38.06	.0750	.173
"	36.65	.0712	"
"	34.91	.0753	"
"	33.22	.0743	"
"	31.41	.0787	"
"	29.68	.0761	"
"	28.00	.0753	"
"	25.60	.0954	"
0.025	49.15	.095	.253
"	46.55	.102	"
"	44.81	.104	"
"	41.63	.107	"
"	40.44	.100	"
"	33.36	.100	"
"	28.76	.079	"
"	23.82	.118	"

APPENDIX G (Cont.)

k	Velocity	σ_1	Gas Content
	fps		%
0.050	29.79	.1233	.266
"	27.90	.1124	"
"	24.43	.1403	"
"	47.43	.1220	.183
"	46.27	.1203	"
"	45.15	.1206	"
"	43.69	.1216	"
"	42.46	.1238	"
"	41.24	.1233	"
"	39.91	.1241	"
"	37.76	.1320	"
"	36.43	.1281	"
"	34.30	.1281	"
"	32.45	.1371	"
.100	50.81	.243	.334
"	47.54	.204	"
"	44.49	.204	"
"	41.55	.227	"
"	39.97	.204	"
"	34.33	.235	"
"	32.75	.243	"
"	24.50	.255	"
"	50.63	.2248	.471
"	48.74	.2270	"
"	47.47	.2347	"
"	45.65	.2287	"
"	43.73	.2374	"
"	41.90	.2498	"
"	40.34	.2549	"
"	37.74	.2615	"
"	35.30	.2612	"
"	32.53	.2719	"
"	30.32	.2681	"

Unclassified
Security Classification

DOCUMENT CONTROL DATA - R&D

(Security classification of title, body of abstract and indexing annotation must be entered when the overall report is classified)

1. ORIGINATING ACTIVITY (Corporate author)

Massachusetts Institute of Technology

2a. REPORT SECURITY CLASSIFICATION

Unclassified

2b. GROUP

EA

3. REPORT TITLE

CAVITATION NEAR SURFACES OF DISTRIBUTED ROUGHNESS

4. DESCRIPTIVE NOTES (Type of report and inclusive dates)

Technical Report

5. AUTHOR(S) (Last name, first name, initial)

Arndt, Roger E. A.
Ippen, Arthur T.

6. REPORT DATE	7a. TOTAL NO. OF PAGES	7b. NO. OF REFS
June 1967	149	90

8a. CONTRACT OR GRANT NO.

DA-31-124-ARO-D-410

b. PROJECT NO.

20014501B33G

c.

d.

9a. ORIGINATOR'S REPORT NUMBER(S)

6024.1-E

9b. OTHER REPORT NO(S) (Any other numbers that may be assigned this report)

Report No. 104 - R67-17

10. AVAILABILITY/LIMITATION NOTICES

This document is subject to special export controls and each transmittal to foreign governments or foreign nationals may be made only with prior approval of the U. S. Army Research Office—Durham, Durham, North Carolina.

The findings in this report are not to be construed as an official Department of the Army position, unless so designated by other authorized documents.

11. SUPPLEMENTARY NOTES

None

12. SPONSORING MILITARY ACTIVITY

U.S. Army Research Office-Durham
Box CM, Duke Station
Durham, North Carolina 27706

13. ABSTRACT

This investigation consists of an experimental study of cavitation inception and the associated bubble dynamics in turbulent boundary layers adjacent to surfaces roughened with two-dimensional triangular grooves. The project was initiated due to the apparent lack of published information on the effects of distributed roughness on cavitation inception as opposed to the effects of isolated irregularities. The experimental program covers the measurement of mean velocity profiles, turbulence intensity and the determination of the cavitation inception index for turbulent flow adjacent to both smooth and rough boundaries. In all cases the test liquid was water at room temperature. Four triangular roughness patterns were tested, consisting of roughness heights of 0.100", 0.050", 0.025", and 0.0125", respectively. The maximum velocity was varied between the limits 16 to 51 feet per second. For the same conditions, cavitating flow was observed by high speed motion pictures. Data concerning bubble distribution, stability, and growth rate were obtained from the photographs and correlated with existing theory.

14. KEY WORDS

cavitation inception
bubble dynamics
turbulent boundary layers
two-dimensional triangular grooves
roughness pressure gradient
equilibrium boundary layers

DD FORM 1 JAN 64 1473

Unclassified
Security Classification